

DISSERTATION
SUBMITTED TO THE
COMBINED FACULTIES OF THE NATURAL SCIENCES AND MATHEMATICS
OF THE RUPERTO-CAROLA-UNIVERSITY OF HEIDELBERG, GERMANY
FOR THE DEGREE OF
DOCTOR OF NATURAL SCIENCES

PUT FORWARD BY

CASSANDRA LORLENE FALLSCHEER

BORN IN: CHICO, CALIFORNIA, USA

ORAL EXAMINATION: FEBRUARY 9th, 2010

*Dedicated to the people of the Kiwanis Chico Community Observatory who taught me to
“keep lookin’ up”.*

Abstract

In this thesis, I study three different evolutionary stages of the massive star formation process looking for supporting evidence for an accretion-based formation scenario of massive stars. The first source studied, the Infrared Dark Cloud IRDC 18223-3, is at one of the earliest observable phases of massive star formation. This source is characterized by a cone-shaped molecular outflow component which is used to establish the outflow orientation. A velocity gradient traced by the molecule N_2H^+ but more convincingly by CH_3OH is indicative of a rotating object oriented orthogonally to the outflow direction. This object is on the order of 28,000 AU in size and does not exhibit Keplerian rotation, but may host a disk within. Modeling this velocity gradient shows that a single rotating and infalling entity is capable of reproducing the observations.

Moving to a High Mass Protostellar Object, IRAS 18151-1208, a well-defined outflow orientation is observed as well as an elongation in the 1.3 millimeter dust continuum that is perpendicular to the outflow. This elongation is modeled using a Monte Carlo 3D radiative transfer code. Comparing the modeling results to those of low mass protostars it is deduced that a scaled up version of low-mass star formation provides a plausible description of the observations in this high mass case. In the scaled up version, the density and flaring exponents as well as the relative scale height at one third of the outer radius remain the same as in the low-mass model. The disk mass, outer radius, and central star's mass and luminosity all increase.

The third source studied in this thesis, the hot molecular core IRAS 18507+0121, exhibits the rich chemistry characterizing the hot core phase of massive star formation. The outflow orientation is confirmed and each chemical species is looked at for indication of rotation. Somewhat surprisingly, clear signatures of rotation are not detected and several possible explanations for this are discussed such as insufficient spatial resolution. However, along the lines of what has been observed in IRAS 18151-1208, a slight elongation in the dust continuum perpendicular to the outflow orientation is detected.

Several approaches are explored as a means of studying whether the observable differences in the massive star formation regions are a result of evolution. Taken individually, no indicator is sufficient to definitively determine an age sequence for the three sources. However, taken collectively, the trends seen in these case studies can be attributed to an evolutionary sequence. The results of this thesis are consistent with an accretion based formation mechanism of massive stars and I conclude that the structural changes of the observed disk-like structures from large-scale to more compact may be the result of evolution.

Zusammenfassung

In dieser Arbeit untersuche ich anhand dreier Beispiele unterschiedliche Stadien massereicher Sternentstehung, um Hinweise zu finden, die eine Beschreibung des Entstehungsprozesses massereicher Sterne mit Hilfe von Akkretion stützen. Die erste untersuchte Quelle, die Dunkelwolke IRDC 18223-3, befindet sich in einer der frühesten beobachtbaren Entwicklungsphasen massereicher Sterne. Charakteristisch für diese Quelle ist ihr kegelförmiger molekularer Ausfluss, mit dessen Hilfe die Ausflussausrichtung bestimmt wird. Der Geschwindigkeitsgradient, der mit Hilfe von N_2H^+ , verlässlicher noch mit Hilfe von CH_3OH , detektiert wird, weist auf ein rotierendes Objekt hin, dessen Drehachse parallel zur Ausflussrichtung steht. Die Größe dieses Objekts liegt in der Größenordnung von 28.000 AE und weist keine Kepler-Rotation auf, könnte im Inneren aber eine Scheibe beherbergen. Die Modellierung dieses Geschwindigkeitsgradienten zeigt, dass ein einzelnes, rotierendes und in sich zusammenstürzendes Objekt in der Lage ist, die Beobachtungen wiederzugeben.

Beim massereichen protostellaren Objekt IRAS 18151-1208 wird neben einer wohldefinierten Ausflussrichtung eine dazu senkrechte, längliche Struktur in der Staubkontinuumsstrahlung bei 1.3 Millimetern beobachtet. Diese Elongation wird mit Hilfe eines 3D Monte-Carlo Strahlungstransportprogrammes modelliert. Der Vergleich dieses Modells mit Modellen von Protosternen geringer Masse lässt darauf schließen, dass eine hochskalierte Variante der Entstehung leichter Sterne eine plausible Beschreibung der Beobachtungen im vorliegenden Fall großer Masse bietet. Bei dieser hochskalierten Variante bleiben sowohl die Dichte- und der Aufweitungsexponent wie auch die Skalenhöhe gemessen bei circa einem Drittel des äußeren Radius, unverändert im Vergleich zum Modell für massearme Sterne. Die Masse der Scheibe und deren äußerer Radius sowie die Masse des Zentralobjekts und dessen Leuchtkraft erhöhen sich.

Die dritte Quelle die in dieser Arbeit untersucht wird, der heiße molekulare Kern IRAS 18507+0121, weist die vielfältige chemische Zusammensetzung, die für die heiße-Kern-Phase der Entstehung massereicher Sterne typisch ist, auf. Die Ausflussausrichtung wird bestätigt und jede chemische Spezies wird auf Anzeichen von Rotation hin untersucht. Überraschenderweise werden keine klaren Rotationsanzeichen detektiert und einige mögliche Erklärungen hierfür werden diskutiert, wie zum Beispiel eine möglicherweise unzureichende räumliche Auflösung. Jedoch findet sich, ähnlich den Beobachtungen von IRAS 18151-1208, eine leichte Elongation senkrecht zum Ausfluss in der Staubkontinuumsstrahlung.

Die beschriebenen Unterschiede in Regionen massereicher Sternentstehung werden daraufhin untersucht, ob sie auf die unterschiedliche Entwicklung zurückzuführen sind. Für sich betrachtet reicht kein Indikator aus, um eine definitive Altersreihenfolge der drei Quellen festzulegen. Zusammengenommen können aber die Tendenzen, die in diesen drei Fallstudien gesehen werden, einer Entwicklungsgeschichte zugeordnet werden. Die Ergebnisse dieser Dissertation stehen im Einklang mit einem akkretionsbasierten Entstehungsmechanismus massereicher Sterne, und ich folgere, dass die beobachteten strukturellen Veränderungen der scheibenähnlichen Systeme von großräumig zu kompakt Folge des Evolutionsprozesses massereicher Sternentstehungsgebiete sind.

Contents

Table of Contents	i
List of Figures	v
List of Tables	vii
1 Introduction	1
1.1 Massive Star Formation	1
1.2 Rotation and Disks	3
1.2.1 Theory	3
1.2.2 Observations	5
1.3 The Tools of the Trade	7
1.4 A Sample of Massive Star Formation Regions	8
2 Rotational Structure and Outflow in the Infrared Dark Cloud 18223-3	11
2.1 Introduction	12
2.2 Observations	13
2.2.1 Submillimeter Array	13
2.2.2 Plateau de Bure Interferometer	16
2.2.3 Pico Veleta 30 m Telescope	16
2.3 Results and Discussion	18
2.3.1 Large Scale Emission	18
2.3.2 Millimeter Continuum Emission	19
2.3.3 Outflow Properties	20
2.3.4 Age of the System	23
2.3.5 Rotational Structure	24
2.3.6 Theoretical Modeling	26
2.4 Conclusions	28
3 A high mass dusty disk candidate: the case of IRAS 18151-1208	33
3.1 Introduction	34
3.2 Observations	35

3.2.1	Submillimeter Array	35
3.2.2	Pico Veleta 30 m Telescope	36
3.3	Observational Results	38
3.3.1	Millimeter Continuum Emission	38
3.3.2	Line Data	38
3.3.3	Spectral Energy Distribution	40
3.4	Modeling	41
3.4.1	The Monte Carlo 3D Radiative Transfer Code	41
3.4.2	The Disk	41
3.4.3	The Dust Model	42
3.4.4	Observational Constraints	42
3.4.5	The Parameter Space	43
3.5	Comparing the Model with Observations	44
3.6	Discussion	47
3.6.1	Testing the Parameter Space	47
3.6.2	Comparison with T Tauri Stars	50
3.6.3	Rotation and Infall	52
3.6.4	Predictions for Future Observatories	52
3.7	Conclusions	53
4	The Hot Core Source: IRAS 18507+0121	55
4.1	Introduction	55
4.2	Observations	56
4.2.1	Submillimeter Array	57
4.2.2	Pico Veleta 30 m Telescope	59
4.3	Results and Discussion	59
4.3.1	Millimeter Continuum Emission	59
4.3.2	Line Data and Outflow Properties	60
4.3.3	Velocity Structure	64
4.4	Conclusions	65
5	Comparison of the Case Studies	67
5.1	The Spectral Approach	68
5.1.1	Infrared Observations	68
5.1.2	SMA Spectra	68
5.1.3	CH ₃ OH	70
5.1.4	C ¹⁸ O Line Width	70
5.2	The Physical Approach	70
5.2.1	Outflow Extent and Outflow Dynamical Age	71
5.2.2	Spatial Extent of the Disk-like Object	71

6	Conclusions	73
6.1	Summary	73
6.1.1	Outflow	73
6.1.2	Disk Indications	74
6.1.3	Theoretical Modeling	75
6.2	Direction for the Future	76
	Acknowledgments	79
	Bibliography	81

List of Figures

1.1	Simulation of massive accretion disk	3
1.2	Observations of a disk component around IRS 15	6
1.3	Observations of a disk component in IRAS 20126+4104	6
2.1	Velocity integrated $^{12}\text{CO}(2-1)$ single dish image of IRDC 18223-3.	17
2.2	PdBI 3mm 0th, 1st, and 2nd moment maps	18
2.3	The 1.1 mm (SMA), 1.3 mm (SMA), and 3.4 mm (PdBI) dust continuum	20
2.4	$^{12}\text{CO}(2-1)$ integrated maps from SMA, IRAM 30 m, and SMA + IRAM 30 m combined showing the outflow orientation	22
2.5	The SiO(2-1) integrated map	23
2.6	$\text{C}^{18}\text{O}(2-1)$, $\text{CH}_3\text{OH}(6_0-5_0)$ A, and $\text{N}_2\text{H}^+(3-2)$ total intensity (0th) and velocity (1st) moment maps	25
2.7	Position-velocity diagrams of CH_3OH and N_2H^+ derived for cuts along the ob- served velocity gradient	26
2.8	Ulrich infall model of the velocity gradient seen in CH_3OH	29
2.9	The model after convolving and rotating	30
3.1	Spectra of IRAS 18151-1208 from the SMA	36
3.2	1.3 mm dust continuum	37
3.3	Zoomed in view of the primary peak of the 1.3 mm dust continuum	37
3.4	The outflow in $^{12}\text{CO}(2-1)$	39
3.5	SED of the best fit model	45
3.6	Radial density profile of the best fit model	45
3.7	Effect on the SED of varying individual parameters	46
3.8	Effect on the radial brightness profiles of varying individual parameters	48
3.9	Contour plot of the Toomre Q stability parameter	49
3.10	C^{18}O , CH_3OH , and SO velocity moment maps	51
3.11	Predictions at mid-infrared and millimeter wavelengths of what may be observ- able with future observatories	52
4.1	Spitzer 24 μm image with IRAM 30m 1.2 mm continuum contours	56

4.2	Spectra of IRAS 18507+0121 from the SMA	57
4.3	SMA 1.3 mm dust continuum	59
4.4	Blue- and redshifted ^{12}CO emission	61
4.5	IRAS 18507+0121 velocity moment maps	62
4.5	continued	63
4.6	Position-velocity diagram of C^{18}O	64
4.7	Velocity moment map of ^{13}CO	65
5.1	SMA spectra of IRDC 18223-3, IRAS 18151-1208, IRAS 18507+0121	69
6.1	ALMA	77

List of Tables

2.1	Observed lines in IRDC 18223-3	14
2.2	Plateau de Bure Interferometer (PdBI), Submillimeter Array (SMA), and IRAM 30 m observation parameters.	15
2.3	Outflow parameters for IRDC 18223-3	21
3.1	SMA observation parameters	35
3.2	Observed lines in IRAS 18151-1208	35
3.3	Outflow properties derived from CO observations	38
3.4	Sources of SED data points	40
3.5	The parameters used in the best fit model	47
4.1	Observed lines in IRAS 18507+0121	58
4.2	Outflow parameters for IRAS 18507+0121	61
5.1	Comparison of observed/derived quantities of the three sources	67

Chapter 1

Introduction

Throughout their existence, massive stars have a high impact on their surroundings. Massive molecular outflows induce further star formation at the infant stages of evolution. Then, during their main sequence lifetime, stellar winds heat and ionize the interstellar medium. Finally, when they end their lives as supernovae, massive stars enrich the interstellar medium with heavy elements. Massive stars are thus important entities in the cosmic scheme of things.

1.1 Massive Star Formation

The seeds of star formation, namely regions of slight overdensity, begin to collapse gravitationally within cold, dark, giant molecular clouds marking the beginning of the star formation process. Many of these overdense regions exist within any one molecular cloud, leading eventually to a cluster of stars varying widely in mass from the sub-stellar mass limit all the way up to several dozen solar masses and even up to around 150 solar masses in some extreme cases (Massey & Hunter 1998).

The formation process is relatively well described for a low mass star like our Sun. In the case of low mass stars, a protostar forms during the gravitational collapse stage, characterized by bipolar molecular outflows fed by a circumstellar disk which simultaneously provides the material which accretes onto the central protostar. The evolution then proceeds through the T Tauri star phase with the central object surrounded by a protoplanetary disk out of which planetesimals will eventually form into a planetary system. After the accretion phase, these T Tauri stars slowly contract until hydrogen burning begins in the star's nucleus marking its entry onto the main sequence.

The picture is far less clear for massive stars. The theory of massive star formation is not well understood, in part because the current state of observational constraints is limited. In order to guide theoretical modeling efforts, it is necessary to have a clear observational picture of the process of massive star formation. However, this is an observationally difficult task.

Massive stars ($M > 8M_{\odot}$) tend to form toward the centers of clusters in regions with many neighboring stars and where the optical depth of the cloud is high. These create observational

difficulties in the form of source confusion and observable wavelength regime restrictions. Exacerbating the difficulty is that massive stars are rare as described by the initial mass function (IMF). The IMF is the distribution of the number of stars of a given mass that will be formed within a star cluster. Early work indicated that the IMF is a power law function of mass with an exponent of -2.35 (Salpeter 1955), while later work indicates that there may be different power law exponents at different mass regimes (Scalo 1986; Kroupa et al. 1993). Both theoretical and observational work is still being conducted to determine the origin of the slope of the IMF in the high mass regime (Clark et al. 2009; Rodón et al. 2009, *submitted*).

Additionally, massive stars form and evolve on much shorter evolutionary timescales than low mass stars. Accretion timescales for low mass stars are fairly well established (Iben 1965; Wuchterl & Klessen 2001), but for the high mass regime, formation time estimates are based on the range of accretion rates from 10^{-4} - 10^{-3} solar masses per year expected in massive star formation (McKee & Tan 2003). A $10 M_{\odot}$ star probably accretes at a rate on the lower side of this range while a more massive star will have a larger accretion rate and correspondingly a shorter time in the main accretion phase. So while a $1 M_{\odot}$ star takes 50 million years before it reaches the main sequence, a $10 M_{\odot}$ star may take around 100,000 years and a $30 M_{\odot}$ on the order of 10,000 years, although massive stars do continue to accrete material after they have reached the main sequence. This leads to the creation of an observational challenge to learn about massive star formation since their short evolutionary timescales coupled with their sparsity determined by the IMF have the overall effect that the distances to massive star formation regions are on average larger than to low mass star formation regions.

Despite these observational difficulties, the broad sequence of events through which a massive star evolves has been identified (see reviews by Churchwell 2002; Beuther et al. 2007; Zinnecker & Yorke 2007). The process begins in high-mass starless cores, then transitions to a high-mass core containing protostars of low- to intermediate-mass that will become high-mass objects with time. These initial stages are deeply embedded within Infrared Dark Clouds. The process then progresses through a high mass protostellar object phase and continues on to the later stages of massive star formation as a hot core. During the massive protostellar object phase, the source produces ionizing radiation which forms Hypercompact HII (HCHII) regions. These regions are associated with water masers which are often taken as indicators of massive star formation (Churchwell et al. 1990). After undergoing expansion, HCHII regions become Ultracompact HII (UCHII) regions with sizes less than 0.1 pc (Kurtz 2002). Compared to UCHII regions, the diameters of HCHII regions are typically an order of magnitude smaller (<0.01 pc), and densities in HCHII regions are on the order of 100 times higher. While most massive protostars hosted by HCHII regions are still undergoing accretion, some within UCHII regions may still be accreting as well. After the star has reached its final mass, the UCHII regions transition into Compact HII regions, then finally HII regions.

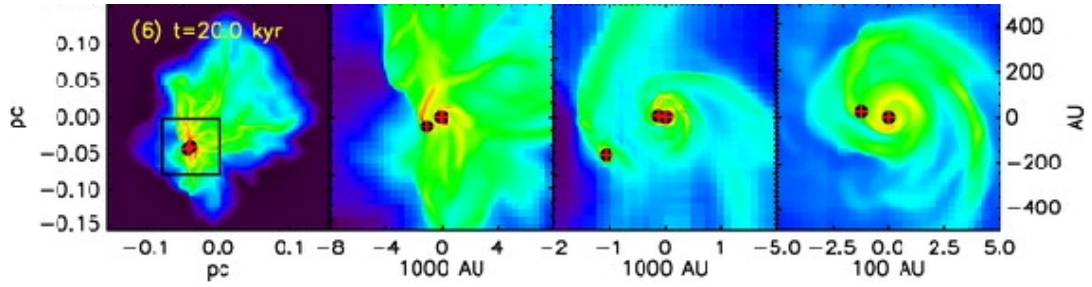


Figure 1.1: Simulated column density in a massive star formation region after evolving for 20,000 years. The panels become progressively zoomed in from left to right. Several protostars have formed within the disk and are indicated by plus signs. The panels (except the first panel) are centered on the primary star. Figure credit: Fig. 3 in Krumholz et al. (2007).

1.2 Rotation and Disks

This thesis focuses on the existence, observable properties, evolution and characterization of circumstellar accretion disks in massive star formation. The past decade has seen a drastic increase in disk studies of massive star formation regions corresponding roughly to the advent of millimeter interferometer facilities (e.g. Submillimeter Array on Mauna Kea in Hawaii, Plateau de Bure in the French Alps, Owens Valley Radio Observatory in eastern California). Concurrently, work on theoretical descriptions of how disks may evolve has received increased attention.

1.2.1 Theory

It was once thought that radiation pressure from a forming massive star would become too strong and interfere with further accretion, creating a road block for the idea that massive star formation may proceed in a similar fashion to low mass star formation (Larson & Starrfield 1971; Kahn 1974; Wolfire & Cassinelli 1987; Jijina & Adams 1996). Various methods were proposed for how to overcome this radiation pressure, including circumstellar accretion disks (Jijina & Adams 1996; Yorke & Sonnhalter 2002; Vaidya et al. 2009), modified dust properties (Wolfire & Cassinelli 1987), high accretion rates (Wolfire & Cassinelli 1987; McKee & Tan 2003), or accretion at later stages in the formation process through the HCHII region (Keto 2003). More recently, simulations by Krumholz et al. (2007, 2009) indicate that massive stars at least up to $40 M_{\odot}$ can in fact form via accretion from circumstellar disks. These simulations show that it is possible that companions to the massive star may also form within the disk. A demonstration of this as well as the structure of the modeled disk is shown in Fig. 1.1. The geometry of such a structure is likely a non-axisymmetric thin disk which is very hot in the inner regions (Kratter & Matzner 2006; Krumholz et al. 2009; Vaidya et al. 2009).

An accretion based theory proposed by Keto (2003); Keto & Wood (2006) is that even once the massive protostar has created a HCHII region, this region does not inhibit the flow of material onto the protostar. In this description, molecular gas becomes ionized in the HCHII region and

continues onto a group of stars in the center via an ionized accretion disk.

Accretion based theories suggest that the accretion rate onto massive protostars is on the order of 10^{-4} - 10^{-3} solar masses per year (McKee & Tan 2003; Banerjee & Pudritz 2007). This are several orders of magnitude higher than the accretion rate onto low mass protostars and allows the formation of a massive star before the radiation pressure becomes dominant. These theories are consistent with the abundant observations of collimated molecular outflows in massive star formation regions (Shepherd & Churchwell 1996; Beuther et al. 2002b; López-Sepulcre et al. 2009). Arce et al. (2007) review the properties of such massive outflows and summarize scenarios for explaining these properties. Molecular outflows are entrained by jets which are driven by magnetohydrodynamic acceleration from an accretion disk. In accretion based theoretical descriptions of massive star formation, these disks also provide the material which accretes onto the central star (or stars).

A second scenario describing massive star formation is that of competitive accretion (Bonnell et al. 1997, 2001, 2004; Bonnell & Bate 2006). In this theoretical framework, the most massive protostars competitively accrete material from their surroundings. In this description, environmental factors heavily influence the final mass of the massive star. Thinking of a cluster forming region as a potential well, protostars closer to the center of the cluster will be affected more by the gravitational potential than protostars further toward the edge of the cluster. Hence, the infalling gas within the cluster will be funneled preferentially onto those protostars closer to the cluster center opposed to protostars further out. With accretion rates of the protostars at the center much higher than of those further out, massive stars will tend to form in the cluster center leaving low mass stars to form in the outskirts.

A subsidiary method proposed by Bonnell et al. (1998) and Bally & Zinnecker (2005) which may play a role in some extreme instances is that massive stars could form through the merging and coalescence of lower mass objects. While this mechanism for massive star formation is supported by the observation that massive stars tend to form in the busiest regions of star formation, namely, dense cluster centers, it does not provide a direct explanation for the molecular outflows that are observed in massive star formation regions. Disks are not an integral part of this explanation for massive star formation, as the process of merging would be quite violent and chaotic.

One strength of the competitive accretion model is that it sufficiently describes the origin of the IMF. Keplerian disks around massive protostars are not ruled out explicitly in this theory, but within the highly turbulent cluster forming regions, large disks would be unlikely to survive. However, this theory may be adequate to describe some instances of massive star formation, so the best description of massive star formation may be a combination of the methods described here. For the sake of this thesis, we hypothesize that, as in low mass star formation, the existence of molecular outflows is a direct indication that an accretion disk is providing the reservoir from which the material comes.

1.2.2 Observations

In the case of low mass star formation, disks around protostars can be studied in a straightforward fashion. Examples of disks around low mass T Tauri and even intermediate mass Herbig Ae/Be stars exist that are close enough such that the disk component can be observed both spatially and kinematically in intricate detail [e.g. the T Tauri star TW Hya (Kastner et al. 1997; Qi et al. 2004), the Herbig Ae star HD 141569A (Goto et al. 2006); see review by Dutrey et al. 2007]. The proximity of several of these systems, coupled with their visibility at wavelengths that both interferometers and current space telescopes are sensitive to, allows resolution down to the order of several tens of astronomical units (AU). For example, the T Tauri star BP Tau at a distance of 56 pc observed with the Plateau de Bure Interferometer at a resolution of less than 1'' corresponds to a spatial resolution of ~ 40 AU (Simon et al. 2000). This is not possible in the massive regime due to the combination of larger distances to the closest massive star formation regions, the clustered mode of massive star formation, and current technology limitations. However, certain aspects of the massive star formation process are observable, and from these, we can deduce a reasonable picture with which to guide theoretical modeling.

In the intermediate mass regime (~ 5 - $10 M_{\odot}$) there are several examples of rotating disk structures surrounding a central object [e.g. AFGL 490 (Schreyer et al. 2002, 2006), G192.16-3.82 (Shepherd & Kurtz 1999; Shepherd et al. 2001), G92.67+3.07 (Bernard et al. 1999), M17 (Chini et al. 2004)]. An example of such a structure can be seen in Fig. 1.2. Another good example of this is IRAS 20126+4104 (Cesaroni et al. 1997, 2005). This $\sim 10^4 L_{\odot}$ source has a bipolar molecular outflow and is associated with water maser activity (Moscadelli et al. 2005). Infrared observations resolve two components, indicating a multiple system within the disk (Sridharan et al. 2005b) while centimeter observations resolve the core into three components (Hofner et al. 2007). Observations of a velocity gradient perpendicular to the outflow orientation provide a strong case for an accretion disk scenario around this well-studied $7 M_{\odot}$ central source. The outflow orientation, position of the masers, as well as the velocity gradient observed in IRAS 20126+4104 can be seen in Fig. 1.3.

Rotating objects around higher mass objects have been detected, but the terminology reserved for these structures by Cesaroni (2005) is usually circumstellar ‘toroids’. Several examples of these objects include G24.78+0.08 (Beltrán et al. 2004, 2005), G28.20-0.05 (Sollins et al. 2005), IRAS 18089-1732 (Beuther & Walsh 2008) and NGC 7538 S (Sandell et al. 2003). They are not classified as disks because they do not fit into the classical picture of low-mass disks. These rotating toroids have typical radii of thousands of AU and masses comparable to or slightly larger than the mass of the central source. They are not in Keplerian rotation although they may be feeding inner accretion disks, and likely surround multiple sources.

The observation of a true accretion disk around an O-type star remains elusive, although they are theoretically predicted (Krumholz et al. 2007, 2009; Keto 2003). One of the more common techniques currently used in the attempt to detect observational signatures of disks is to determine the outflow orientation and then look at maps of high density tracing molecules to

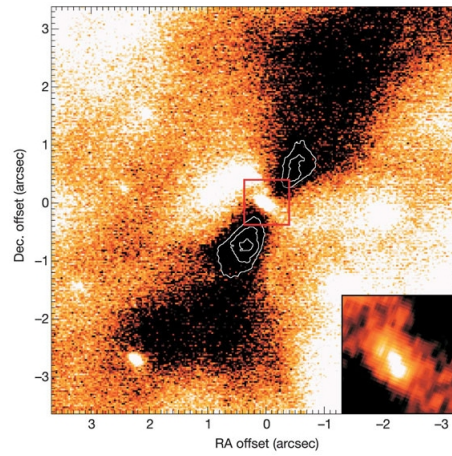


Figure 1.2: The silhouette of a disk structure around one of the stars in M 17, IRS 15, can be seen in this $2.2 \mu\text{m}$ image. The contours outline the densest region of the inner torus. The diameter of the structure is approximately 20,000 AU. A zoomed-in version of the central star is displayed in the lower right corner. It's elongation is due to the observing technique. Figure credit: Fig. 1 in Chini et al. (2004).

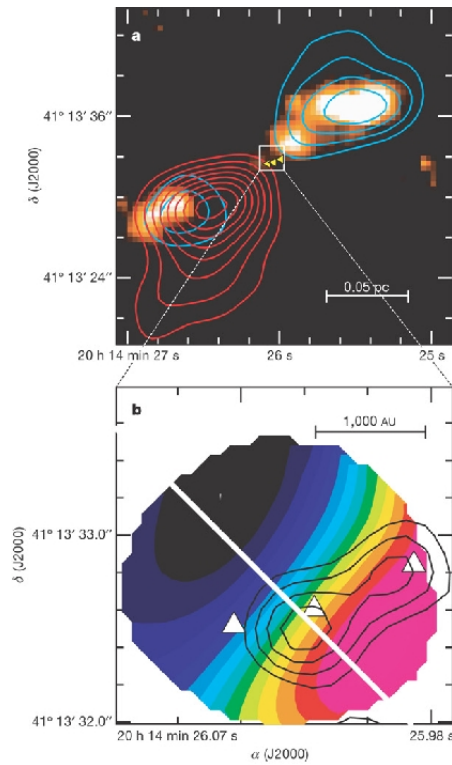


Figure 1.3: In the upper panel, the red- and blueshifted $\text{HCO}^+(1-0)$ tracing the outflow is shown in color-coded contours overlaid on the $2.2 \mu\text{m}$ H_2 emission. In the lower panel, contours of the 3.6 cm continuum are overlaid on a velocity map of $\text{C}^{34}\text{S}(5-4)$. A velocity gradient perpendicular to the outflow is apparent by the color scale with red corresponding to redshifted emission and blue to blueshifted emission. In both panels, the H_2O masers are marked by triangles. Figure credit: Fig. 1 in Cesaroni et al. (2006).

see whether a velocity gradient perpendicular to the outflow exists. Molecules that have been used in the past include $C^{17}O$ (Schreyer et al. 2006), NH_3 (Keto et al. 1988), $C^{34}S$ (Cesaroni et al. 2005), CH_3CN (Zhang et al. 1998), and $HCOOCH_3$ (Beuther et al. 2005d). However, one of the things we show in this thesis is that a molecule which traces rotation in one source may not do so in another source. It is still open to debate whether the molecular tracers change with time or environment, and even whether there are other molecules that have yet to be identified as disk tracers.

It is highly likely that massive disks are significantly larger than their low-mass counterparts, but a quantitative estimate for how much larger is not known. The dynamics of low mass disk systems dictate that the disks exhibit Keplerian rotation. The massive disks, on the other hand, probably have a non-negligible amount of mass compared to the central object and would not be Keplerian. In contrast to low mass disks, massive accretion disks are likely self-gravitating and may form multiple sources within the disk (Krumholz et al. 2009).

1.3 The Tools of the Trade

Observational studies of massive star formation are hindered by the inherent properties of massive star formation regions as described above. Observations at optical and even infrared wavelengths are not possible at the early stages of massive star formation due to obscuration from high optical depth of the envelope at these wavelengths. It is thus necessary to observe these regions at millimeter and submillimeter wavelengths. At these wavelengths, the cold dust can be detected by its continuum emission, and the presence of molecular lines provide further information about the structure and kinematics of the gas in these regions. However, due to the large average distances to massive star formation regions, high angular resolution is necessary to resolve the expected size scales of massive disks. This is made possible through the use of interferometry. An overview of the theory and methods behind this technique are described in Jackson (2008) and a much more in depth analysis is given by Thompson et al. (2001).

The basic principle of radio interferometry is that an array of antennas which are spatially separated observe a source simultaneously and the radio waves collected by each antenna can be combined to form an image. The resulting image has an angular resolution defined by the longest baseline (the distance between the two antennas spaced furthest apart) in the array. The larger the longest baseline is, the higher the angular resolution. In interferometry, angular resolution is not the only important element. Sensitivity is another important factor. The higher the percentage of collecting area within the array, the fainter the detection limit.

The result of not having collecting area within the shortest baseline is that the emission from the largest structures in the target region is filtered out. It is therefore helpful to have observations from single dish telescopes. These single dish observations on their own do not have very high angular resolution, but have the advantage that they do not filter out flux from large scale structures such as the massive extended outflows. For spectral lines, it is usually

possible to combine the single dish observations with the interferometric data to benefit from the strengths of both types of observations. This approach affords high angular resolution but minimizes the effects of missing short spacing information.

An additional consideration for the instrumentation is that the spectral resolution must be sufficient to resolve the kinematic signatures of disks. Spectral resolution of less than a km s^{-1} is attainable, and as the rotational velocities are expected to be on the order of a few km s^{-1} , this is not the limiting factor in massive disk studies.

1.4 A Sample of Massive Star Formation Regions

Here we present three case studies of massive star formation regions. These three sources are at different stages in the evolutionary process, and in this thesis we will explore different lines of reasoning supporting this.

The Infrared Dark Cloud 18223-3: The youngest source in our study is at one of the earliest stages of massive star formation. The Infrared Dark Cloud 18223-3 was originally detected due to its proximity to the Infrared Astronomical Satellite source IRAS 18223-1243. Using the IRAM 30 m telescope, a 1.2 mm continuum survey of 69 high-mass protostellar objects was conducted (Beuther et al. 2002a). One of the sources in this study was IRAS 18223-1243. Within a filament extending from IRAS 18223-1243, IRDC 18223-3 was identified approximately $3.5'$ south of the IRAS source. Observations of CS and CO with the IRAM 30 m telescope exhibit features in the wings of these spectral lines indicative of early star formation and outflow activity (Beuther et al. 2005b). Although Spitzer observations from the GLIMPSE survey of the Galactic plane at 3.6, 4.5, 5.8, and $8.0 \mu\text{m}$ (Benjamin et al. 2003) do not detect IRDC 18223-3, the lack of a midinfrared counterpart may be due to the source's extreme youth.

Multiple sets of observations support the idea that this source is very young. For example, while H_2 emission in the $4.5 \mu\text{m}$ band is not seen at the peak position of the millimeter dust continuum, it is detected on either side of the continuum peak and likely is the result of an outflow producing shocked emission when it collides with the molecular gas in the vicinity. These phenomena are commonly known as green fuzzies or extended green objects (EGOs) because of the green color coding commonly assigned to the $4.5 \mu\text{m}$ band in three-color images (e.g. Cyganowski et al. 2008). $\text{N}_2\text{H}^+(1-0)$ observations with the Plateau de Bure Interferometer (Beuther et al. 2005b) reveal a secondary peak approximately $6''$ east of the main peak which is not detected in the dust continuum. Analysis of the N_2H^+ line widths in the region also point to early stages of star formation.

Observations from the Spitzer MIPS GAL survey (Carey et al. 2005) detect $24 \mu\text{m}$ emission from IRDC 18223-3. Using 24 and $70 \mu\text{m}$ fluxes from this survey in addition to fluxes obtained from earlier data sets, Beuther & Steinacker (2007) determine via spectral energy distribution (SED) fitting that a single-component blackbody is insufficient to reproduce the observed SED. These authors found that a warm component with $\sim 0.01 M_\odot$ at $\sim 50 \text{K}$ and a more massive (~ 600

M_{\odot}) cold component (15 K) are necessary to fit the observed SED. In this thesis (Chapter 2), we present line and continuum observations of IRDC 18223-3 from the Submillimeter Array and IRAM 30 m telescope identifying the outflow orientation and a large rotational structure perpendicular to the outflow.

The other two case studies presented here (IRAS 18151-1208 and IRAS 18507+0121) are members of a sample of nine massive disk candidates (PI Q. Zhang). The purpose of this effort is to study the outflow, accretion, and infall properties of massive star formation regions. Observations for this project were carried out at the SMA and IRAM 30 m telescope. Observation of all sources in both the compact and extended SMA configurations at 230 GHz offer high angular resolution corresponding to a few thousand AU at the typical distances of the sources in the survey. Included in the spectral setup is the primary outflow tracer $^{12}\text{CO}(2-1)$ as well other molecules helpful in star formation studies such as ^{13}CO , C^{18}O , SO , CH_3OH and CH_3CN . Complementary single dish measurements of ^{12}CO and ^{13}CO recover the flux lost due to missing short spacings in the interferometer data and are critical for the correct interpretation of large scale emission such as the outflow component. Other collaborators in this effort include H. Beuther (IRAS 18182-1432), Q. Zhang (IRAS 18566+0408), K. Qiu (IRAS 18360-0537), R. Cesaroni & M. Beltrán (G31.41+0.31 & G24.78+0.08), R. Galván-Madrid & L. Zapata (W33A).

The High Mass Protostellar Object IRAS 18151-1208: IRAS 18151-1208 was previously observed at multiple frequencies and in several molecular line tracers in the survey of Sridharan et al. (2002); Beuther et al. (2002b). Although these data have relatively low spatial resolution, they give preliminary indication for the existence of an outflow in the region. Later, a survey at 450 and 850 μm with the James Clerk Maxwell Telescope (JCMT) also included IRAS 18151-1208 and found similar morphology as in the 1.2 mm continuum observations of Beuther et al. (2002a) (Williams et al. 2004). Observations with a narrow band H_2 filter at 2.122 μm on the U.K. Infrared Telescope (UKIRT) show clear indication of two collimated bipolar jets of molecular H_2 emission. One of these jets emanates from the IRAS 18151-1208 source, while the other is likely produced by a younger, more embedded secondary source a few arcseconds to the southwest (Davis et al. 2004).

Campbell et al. (2008) measure the 10 μm silicate absorption feature in the spectrum of IRAS 18151-1208 at high spectral resolution. They also observe IRAS 18151-1208 with a narrow band filter at 24.8 μm using the Infrared Telescope Facility (IRTF). They then reproduce these measurements with a simple dust model and conclude that IRAS 18151-1208 is an early stage high mass protostellar object with a luminosity suggesting an early B spectral type. Further SED analysis was done by Marseille et al. (2008) over a broader range of wavelengths. These authors also present single dish maps of molecular emission and models of the dust continuum emission.

In Chapter 3, we present and analyze the high resolution SMA and IRAM 30 m data of the high mass protostellar object IRAS 18151-1208. The CO measurements trace the molecular

outflow and an elongation in the dust continuum perpendicular to this orientation suggests the possibility of a disk surrounding IRAS 18151-1208. We then model the SED and produce modeled images at 1.3 mm using a Monte Carlo 3D Radiative Transfer previously used for disks around protostars in the low mass regime.

The Hot Molecular Core IRAS 18507+0121: IRAS 18507+0121 is a typical hot molecular core (HMC) source exhibiting a rich chemical diversity. The general region surrounding IRAS 18507+0121 includes four cores within an infrared dark cloud extending in the north-south direction (Rathborne et al. 2005). Three of these four cores are actively undergoing massive star formation. The core in the multiwavelength study by Rathborne et al. (2005) termed MM1 refers to the source of our current studies.

The outflow component of IRAS 18507+0121 is well-defined and studied in detail with CO(1–0) by Shepherd et al. (2007). These authors find two outflows emanating from this source (which they refer to as G34.4+0.23 MM) and three more outflows coming from a nearby UCH_{II} region. For the outflows associated with G34.4+0.23 MM, the redshifted lobe of the main outflow which extends southwest from the source is the dominant component. The blueshifted counterpart and the other outflow are significantly weaker. Earlier 1.2 mm continuum maps including G34.4+0.23 MM and the UCH_{II} region which is $\sim 40''$ to the south are consistent with G23.4+0.23 MM having a B2 protostar at its center (Shepherd et al. 2004), although later fitting of the SED from infrared through millimeter wavelengths is more consistent with a B0 protostar (Rathborne et al. 2008).

In earlier work by Ramesh et al. (1997), infall is detected by modeling the single dish spectra of the high density tracers HCO⁺, H¹³CO⁺, CS, and C³⁴S. More recently, Rathborne et al. (2008) compare this region to another star forming core. The 345 GHz SMA and single dish data presented in that comparison study support the interpretation that MM1 is a hot, compact, and dense HMC undergoing massive star formation. The authors detect rotation in ¹³CO and suggest that this may be due to either an outflow or a rotating envelope. Additionally, interferometric polarimetry of this source indicate the presence of a magnetic field oriented in the east-west direction (Cortes et al. 2008).

In Chapter 4, we confirm the outflow orientation observed by Shepherd et al. (2007) and take advantage of the high angular resolution SMA data to go on a quest for signatures of rotation perpendicular to the outflow, although this proves difficult.

Through the study of these three sources undergoing massive star formation, we highlight the set of differences and similarities between the sources and propose that these differences are a result of an evolutionary sequence. In the following three chapters, the case studies of each of the three sources will be described. In Chapter 5, we take a critical look at some of the properties which make each source unique, and other properties that link the sources together into the overall picture of massive star formation. While each of these sources exhibits behavior worthy of individual study, the set of these case studies is particularly valuable as a means of discussing possible evolutionary scenarios of disks in massive star formation.

Chapter 2

Rotational Structure and Outflow in the Infrared Dark Cloud 18223-3

This chapter is based on a paper published in Astronomy & Astrophysics:

Fallscheer, C., Beuther, H., Zhang, Q., Keto, E., & Sridharan, T. K. 2009, A&A, 504,127

Abstract

Aims. We examine an Infrared Dark Cloud at high spatial resolution as a means to study rotation, outflow, and infall at the onset of massive star formation.

Methods. The Infrared Dark Cloud (IRDC) 18223-3 was observed at 1.1 mm and 1.3 mm with the Submillimeter Array (SMA) and follow-up short spacing information was obtained with the IRAM 30 m telescope. Additional data were taken at 3 mm with the IRAM Plateau de Bure Interferometer (PdBI).

Results. Submillimeter Array observations combined with IRAM 30 meter data in $^{12}\text{CO}(2-1)$ reveal the outflow orientation in the IRDC 18223-3 region, and PdBI 3 mm observations confirm this orientation in other molecular species. The implication of the outflow's presence is that an accretion disk is feeding it, so using line data for high density tracers such as C^{18}O , N_2H^+ , and CH_3OH , we looked for indications of a velocity gradient perpendicular to the outflow direction. Surprisingly, this gradient turns out to be most apparent in CH_3OH . The large size (28,000 AU) of the flattened rotating object detected indicates that this velocity gradient cannot be due solely to a disk, but rather from inward spiraling gas within which a Keplerian disk likely exists. The rotational signatures can be modeled via rotationally infalling gas. From the outflow parameters, we derive properties of the source such as an outflow dynamical age of $\sim 37,000$ years, outflow mass of $\sim 13 M_{\odot}$, and outflow energy of $\sim 1.7 \times 10^{46}$ erg. While the outflow mass and energy are clearly consistent with a high-mass star forming region, the outflow dynamical age indicates a slightly more evolved evolutionary stage than previous spectral energy distribution (SED) modeling indicates.

Conclusions. The orientation of the molecular outflow associated with IRDC 18223-3 is in the northwest-southeast direction and velocity gradients orthogonal to the outflow reveal a large rotating structure likely harboring an accretion disk within. We also present a model of the observed methanol velocity gradient. The calculated outflow properties reveal that this is truly a massive star in the making. These data present evidence for one of the youngest known outflow/infall/disk systems in massive star formation. A tentative evolutionary picture for massive disks is discussed.

2.1 Introduction

Massive stars ($M > 8M_{\odot}$) are paramount constituents of galaxies, yet their formation is significantly less well understood than low-mass star formation. Theories of massive star formation predict massive accretion disks and indirect evidence for disks is prevalent, but observational evidence for such structures is rare. Outflows appear to be widespread in massive star formation regions (Shepherd & Churchwell 1996; Zhang et al. 2001, 2005; ?), and must be powered and fed by a (massive) accretion disk. Evidence of rotation and infall that hint at the presence of disks has been detected in several systems, although further study is required (see reviews by Beuther et al. (2007); Cesaroni et al. (2007); Zinnecker & Yorke (2007)).

Several factors complicate observational disk studies of massive star formation regions. Compared to low mass star formation regions, they are much rarer and further away on average. Additionally, massive stars evolve quickly and typically form deeply embedded within a core at the center of a cluster, thus obscuring the process from optical wavelengths and making it difficult to distinguish one protostar from another in such a busy region of star formation typically at kpc distances. Due to these complications, it is extremely difficult to directly observe massive accretion disks at sufficiently high spatial resolution to definitively identify the disk component.

Nevertheless, today's interferometers are conducive to studies that probe size-scales comparable to the sizes we might expect for accretion disks around massive stars, and studies of disks in massive star formation regions have recently increased significantly in number (Cesaroni et al. 2007).

The detection of circumstellar disks would provide strong support for the theory that massive star formation is similar to a scaled-up version of low-mass star formation (e.g. Yorke & Sonnhalter 2002; Krumholz et al. 2007, 2009). These rotating disks, if present, would exhibit a velocity gradient perpendicular to the established outflow direction.

While previous disk studies in high-mass star formation mainly concentrated on relatively evolved regions such as high-mass protostellar objects (e.g. IRAS 20126+4104, Cesaroni et al. 1997, 2005; G192.16-3.82, Shepherd et al. 2001; IRAS 18089-1732, Beuther & Walsh 2008), here we focus on one of the earliest evolutionary stages, namely an Infrared Dark Cloud.

A survey of high-mass protostellar objects (HMPOs) associated with Infrared Astronomical Satellite (IRAS) sources was conducted (Beuther et al. 2002a), and IRDC 18223-3 happened to

be in the field of view of one of the target sources, IRAS 18223-1243. IRDC 18223-3 lies at a distance of 3.7 kpc (Sridharan et al. 2005a) in a filamentary structure extending south from IRAS 18223-1243 (Beuther et al. 2005b). IRDC 18223-3 is likely a high-mass core containing a young stellar object that is currently accreting at a high enough rate that it will eventually join the high-mass regime (Beuther & Steinacker 2007). Our current studies present the outflow properties of this source and reveal velocity gradients in several molecular species that are not aligned with the outflow orientation.

Based on the analysis of Spitzer observations combined with SMA observations, IRDC 18223-3 is comprised of at least two separate components (Beuther & Steinacker 2007). A cooler component at ~ 15 K contains most of the mass ($580 M_{\odot}$) while a warmer component at ~ 50 K with approximately $0.01 M_{\odot}$ is necessary to explain the excess flux in the SED at $24 \mu\text{m}$. The young source has an accretion-dominated luminosity of $180 L_{\odot}$ that is expected to increase over time. While the young stellar object has not yet accumulated a significant amount of mass, in the framework of the simulations by Krumholz et al. (2007), the source's mass and luminosity are consistent with a large accretion rate of $\sim 10^{-4} M_{\odot} \text{ yr}^{-1}$. This high accretion rate, as well as the outflow parameters we derive, both point to a scenario that this source will eventually become a massive star and that we are looking at one of the earliest stages of massive star formation. Therefore, this source is an excellent case study for looking at the properties of massive stars at the beginning stages of their lifetimes. This source also provides an ideal specimen to study the role of disks in early evolutionary phases of massive star formation.

In this paper we report a cone-shaped structure detected in $^{12}\text{CO}(2-1)$ outlining the molecular outflow as well as a velocity gradient of 3 km s^{-1} in $\text{CH}_3\text{OH}(6_K-5_K)$ and $\text{N}_2\text{H}^+(3-2)$ perpendicular to the outflow. We also see velocity gradients on the order of a few km s^{-1} not aligned with the outflow axis in $\text{C}^{18}\text{O}(2-1)$. Additionally, we present the results of modeling the observed CH_3OH parameters to obtain the velocity and density structure of the region.

2.2 Observations

Observations with the Submillimeter Array, Plateau de Bure Interferometer and IRAM 30 m observatories include the 1.3 mm dust continuum and several spectral lines (see Table 2.1). The details of the observations are discussed below.

2.2.1 Submillimeter Array

Observations of IRDC 18223-3 with the Submillimeter Array¹ were carried out the nights of 30 May 2006, 8 August 2006, 24 July 2007, and 27 August 2007. The phase reference center of this source is R.A. $18^{\text{h}}25^{\text{m}}08.55^{\text{s}}$ Decl. $= -12^{\circ}45'23.3''$ (J2000.0) and the velocity of rest v_{LSR} is

¹The Submillimeter Array is a joint project between the Smithsonian Astrophysical Observatory and the Academia Sinica Institute of Astronomy and Astrophysics, and is funded by the Smithsonian Institution and the Academia Sinica.

Table 2.1: Observed lines

Telescope	Transition	Rest Freq. [GHz]	E_{upper} [K]
PdBI	H ¹³ CO ⁺ 1 → 0	86.754	4
PdBI	SiO 2 → 1	86.847	6
PdBI	HN ¹³ C 1 → 0	87.091	4
SMA	C ¹⁸ O 2 → 1	219.560	16
SMA	SO 6 ₅ → 5 ₄	219.949	35
SMA	¹³ CO 2 → 1	220.399	16
SMA	CH ₃ OH 8 ₋₁ → 7 ₀ E	229.759	89
SMA, 30m	CO 2 → 1	230.538	17
SMA	N ₂ H ⁺ 3 → 2	279.512	27
SMA	CH ₃ OH 6 ₀ → 5 ₀ E	289.939	62
SMA	CH ₃ OH 6 ₋₁ → 5 ₋₁ E	290.070	54
SMA	CH ₃ OH 6 ₀ → 5 ₀ A	290.111	48
SMA	CH ₃ OH 6 ₁ → 5 ₁ E	290.249	70
SMA	CH ₃ OH 6 ₋₂ → 5 ₋₂ E	290.307	75

45.3 km s⁻¹ (Sridharan et al. 2005a). The SMA has two spectral sidebands—both 2 GHz wide separated by 10 GHz. All SMA data sets were calibrated with the IDL superset MIR², then imaged and analyzed with MIRIAD. These submillimeter interferometric observations allow us to probe through the optically opaque molecular cloud which IRDC 18223-3 is deeply embedded within. Specific details of the observations are listed in Table 2.2.

The observations on 30 May 2006 are with all 8 antennas at 1.3 mm in the extended configuration. Zenith opacity measured by the Caltech Submillimeter Observatory was approximately $\tau(230)$ 0.15. Observing with 8 antennas coupled with the fact that the track was 8.5 hours long (5 hours on-source integration) provided optimal coverage in the uv plane. Passband and flux calibrations were derived from observations of Uranus. For the flux, solutions could not be found on all baselines so it was necessary to perform an initial flux calibration on 3C279 to set the relative flux levels. Phase and amplitude calibrations were made from regular observations (5 minutes every half hour) of quasars 1911-201 and 1733-130. The same spectral setup was observed on 8 August 2006 in the compact configuration. Only 7 antennas were used in this data set. Despite τ varying between 0.2 and 0.25, the data are good quality. The same calibration objects were used as in the 30 May data set, however, it was not necessary to set the relative flux levels before using Uranus for the flux calibration. The track was 7 hours long, 4 hours of which were spent on-source. After combination of the data from both configurations, projected baselines range from 9 to 163 k λ .

²The MIR cookbook by Charlie Qi can be found at <http://cfa-www.harvard.edu/cqi/mircook.html>

Table 2.2: Plateau de Bure Interferometer (PdBI), Submillimeter Array (SMA), and IRAM 30 m observation parameters.

Obs	Date	Freq [GHz]	Configuration	Bandpass	Calibrators		Beam [$''$]	rms _{cont} [mJy/bm]	rms _{line} [mJy/bm]
					Phase & Amplitude	Flux			
PdBI	23 May 2006	89	D	3C273	NRAO 530 & 1741-038	MWC 349			
	03 Apr 2007	89	C	3C84	NRAO 530 & 1741-038	MWC 349			
	05 Apr 2007	89	C	3C273	NRAO 530 & 1741-038	MWC 349			
SMA		89	combined				6.7×3.1	0.15	11
	30 May 2006	230	extended	Uranus	1911-201 & 1733-130	Uranus			
	08 Aug 2006	230	compact	Uranus	1911-201 & 1733-130	Uranus			
		230	combined				1.4×1.3	1.6	65
	24 Jul 2007	279	compact	Uranus	1911-201	Uranus			
	27 Aug 2007	279	extended	3C454.3	1733-130	Uranus			
		279	combined				1.3×1.3	2.2	85
30 m	24 Feb 2007	230		on-the-fly mapping			11		0.17 ^a

Entries include the observatory at which the data were taken, the date of observation, the frequency observed, the array configuration, the calibrators, the synthesized beam obtained after inverting and cleaning the data, the 1σ continuum noise level, and the 1 km s^{-1} rms.

^aUnits: K at 0.4 km s^{-1} resolution averaged over the spectra in the central $4''\times 4''$ of the map.

Observations at 1.1 mm were obtained on 24 July 2007 in the compact configuration with all 8 antennas and in the extended configuration with only 6 fully-functioning antennas on 27 August 2007. Zenith opacity, $\tau(230 \text{ GHz})$, was ~ 0.15 for the compact configuration observations, and ~ 0.17 for the extended configuration observations. The quasar 1911-201 was used for phase and amplitude calibrations for the compact configuration data, and quasar 1733-130 was used for the extended configuration data. Uranus was used for flux calibration in both 1.1 mm data sets and for phase and amplitude calibration of the compact configuration. Quasar 3C454.3 was used for bandpass calibration of the extended configuration data as well as to set relative flux levels prior to using Uranus for the absolute flux calibration. Projected baselines ranged from 11 to 189 $k\lambda$ in the combined 1.1 mm data set.

2.2.2 Plateau de Bure Interferometer

Additional observations of IRDC 18223-3 were obtained at 3mm with the IRAM Plateau de Bure Interferometer (PdBI)³ located near Grenoble, France. Observations were carried out on 23 May 2006, then 3 and 5 April 2007. These observations include detections of SiO(2-1), SO₂, HN¹³C, and H¹³CO⁺(1-0) as well as the 3 mm continuum. Quasars NRAO 530 and 1741-038 were used as phase and amplitude calibrators and MWC 349 for flux calibration. Further details are listed in Table 2.2.

2.2.3 Pico Veleta 30 m Telescope

To complement our interferometric data, we obtained short spacing observations of IRDC 18223-3 on 24 February 2007 with the HERA receiver at the IRAM 30 m telescope near Granada, Spain. The ¹²CO(2-1) line at 230.5 GHz and ¹³CO(2-1) at 220.4 GHz were observed in on-the-fly mode, resulting in maps approximately 140'' \times 140'' in extent. The sampling interval was 2'' and the region was scanned four times in the north-south direction and four times in the east-west direction in order to reduce effects caused by the scanning process. The spectra were reduced using CLASS which is part of the GILDAS software package and then right ascension and declination scans were combined with the plait algorithm in GREG, another component of the GILDAS collection. The ¹²CO data have a beam size of 11'' and a T_{mb} corrected rms noise level of 0.17 K at 0.4 km s⁻¹ resolution (averaged over the spectra in the central 4'' \times 4'' region of the map).

After reducing the 30 m data set separately, single dish ¹²CO data were converted to visibilities and then combined with the SMA data sets using the MIRIAD package task UVMODEL. The synthesized beam of the combined data is 1.9'' \times 1.7'' (PA 70°).

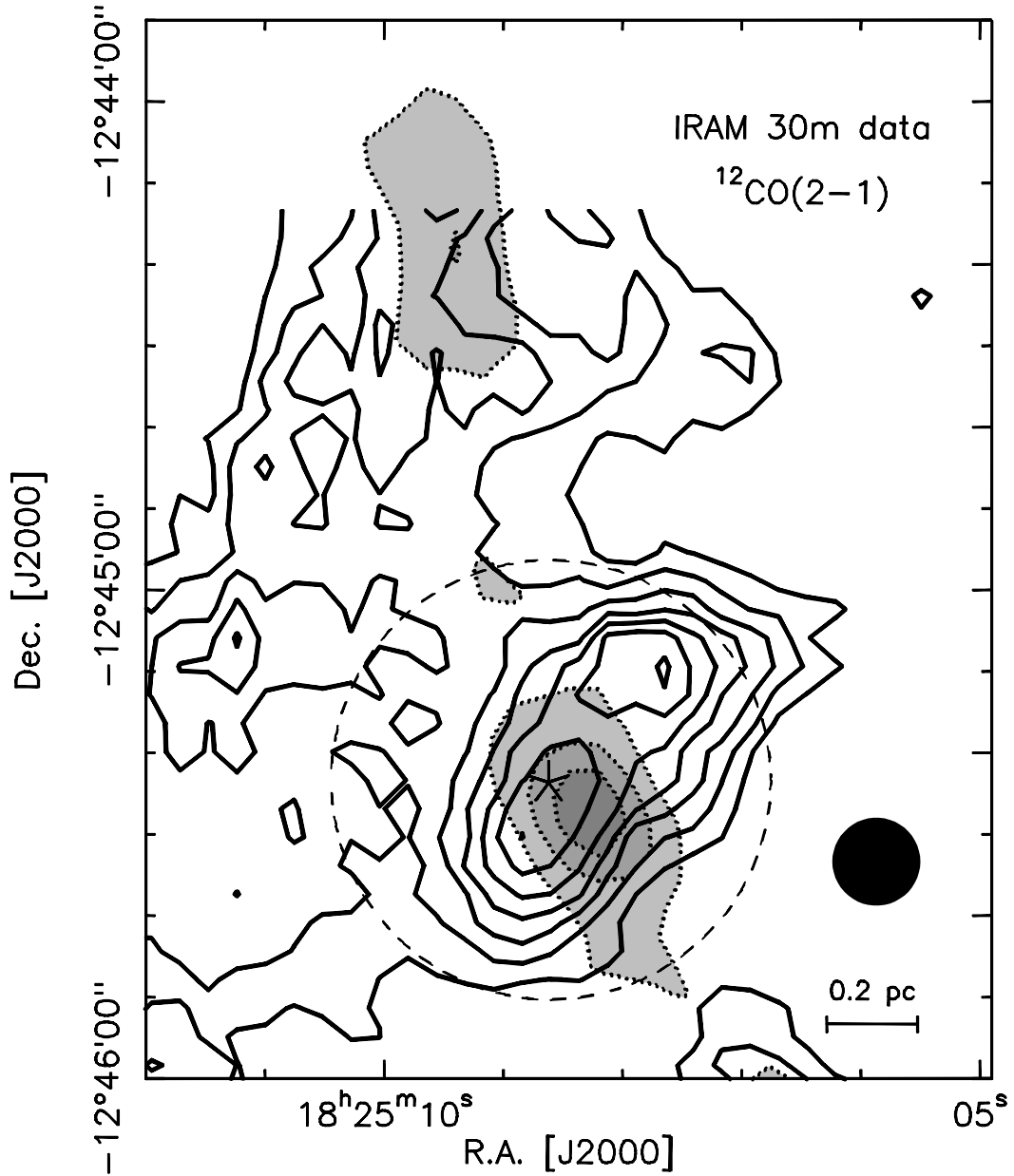


Figure 2.1: Image of the velocity integrated $^{12}\text{CO}(2-1)$ flux from the IRAM 30m single dish telescope of IRDC 18223-3. The integration is from $30-60 \text{ km s}^{-1}$ which includes the entire velocity range of the line. Dotted contours of the 1.2 mm single dish continuum map (Beuther et al. 2002a) are overlaid and shaded in grayscale. The star marks the position of the 1.3 millimeter continuum peak which is approximately $3.5'$ south of IRAS 18223-1243. We attribute the difference in peak position between the 1.2 mm single dish and 1.3 mm interferometer data to pointing error in the single dish data. The size of the SMA primary beam ($54''$) is marked by the dashed circle. The beam size is shown in the bottom right corner.

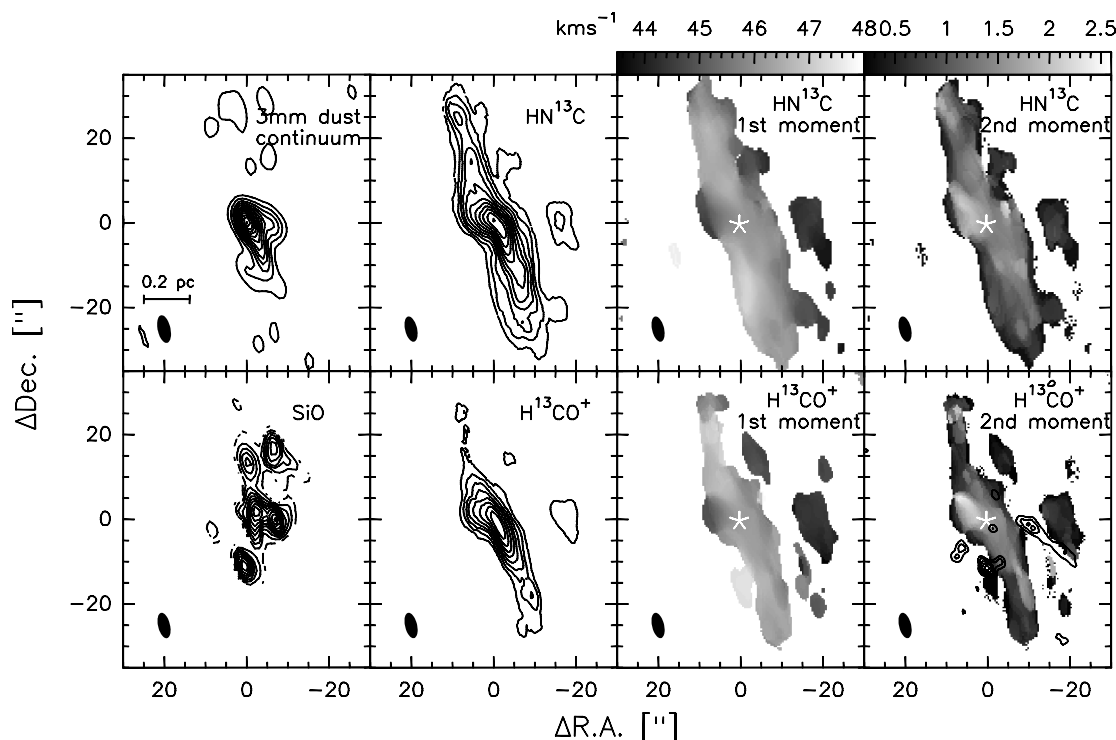


Figure 2.2: Integrated flux of IRDC 18223-3 observed with PdBI of the 3mm dust continuum, SiO, HN^{13}C , and H^{13}CO^+ . The integrations include the entire velocity range of the lines, namely $35\text{--}54\text{ km s}^{-1}$ for SiO, and $43\text{--}48\text{ km s}^{-1}$ for both HN^{13}C and H^{13}CO^+ . Contours always start at the 3σ level. For the continuum, SiO, HN^{13}C , and H^{13}CO^+ respectively, contours increase in steps of 3, 5, 3, and 8σ where σ is 0.15, 11, 16, and 11 mJy bm^{-1} . The velocity (1st) and line width (2nd) moment maps of HN^{13}C and H^{13}CO^+ are presented in the panels on the right. The redshifted CO emission contours are overlaid on the H^{13}CO^+ 2nd moment map. The star indicates the position of the dust continuum peak. The size of the synthesized beam is shown by the ellipse at the bottom left corner of each panel.

2.3 Results and Discussion

2.3.1 Large Scale Emission

IRDC 18223-3 is about $3.5'$ south of IRAS 18223-1243 in a filamentary structure extending more than $5'$ ($>5\text{ pc}$) roughly in the north-south direction across the sky. In the large scale map presented in Fig. 2.1, the 1.2 mm continuum from previous observations (Beuther et al. 2002a) highlights the filamentary structure, and the $^{12}\text{CO}(2\text{--}1)$ mostly traces emission associated with the outflow. We also detect a weaker peak approximately $40''$ east and slightly north of the primary peak. However, as it is outside the primary beam of the interferometer observations, we do not detect this peak in subsequent observations discussed here. It is interesting to note that this $\text{CO}(2\text{--}1)$ peak is not associated with any emission in the 1.2 mm dust continuum.

Figure 2.2 presents the PdBI observations of several molecular species along with the dust continuum. We defer discussion of SiO, a shock tracer, to Section 2.3.3, Outflow Properties, because separate blueshifted and redshifted integrated maps (Fig. 2.5) indicate that it is associated with outflow activity. HN^{13}C and H^{13}CO^+ both trace the large filamentary structure associated

³IRAM is supported by INSU/CNRS (France), MPG (Germany) and IGN (Spain)

with IRAS 18223-1243 seen previously by Beuther et al. (2005b). Even the 3 mm dust continuum exhibits elongation along the filamentary structure. The slight protrusion westward of the central 3 mm continuum peak may come about as a contribution from the outflow as there is also a peak in SiO at approximately the same spatial position. As we do not see any indication of large scale velocity gradients in the first (velocity) moment maps of HN^{13}C and H^{13}CO^+ , there likely is no significant movement happening along the filament although we cannot exclude the expansion of gas in the plane of the sky. In contrast to previous $\text{N}_2\text{H}^+(1-0)$ data (Beuther et al. 2005b), we do not see an increase in line width directly centered on IRDC 18223-3 in the second (line width) moment maps. Rather, we see increased line width to the northeast of the central peak. The position of this peak in the second moment maps does not appear to be related to the outflow.

2.3.2 Millimeter Continuum Emission

The interferometer continuum data (Fig. 2.3) resolve the central structure into several peaks at a spatial resolution of ~ 4000 AU. The 1.1 mm dust continuum traces one main peak with 65 mJy bm^{-1} and three secondary peaks. A secondary peak of 17 mJy bm^{-1} occurs $4.0''$ to the northeast (P.A.= 26°) and another peak of 22 mJy bm^{-1} is situated $3.2''$ to the southwest (P.A.= 261°) These secondary peaks as well as a 27 mJy bm^{-1} peak that is more removed from the main peak ($7.9''$ with P.A.= 209°) are also detected at 1.3 mm, but an extension to the northwest in the 1.1 mm continuum is not seen at 1.3 mm. While the secondary peaks may be separate sub-sources, the line data presented below indicate that the two near-by peaks to the northeast and southwest are likely part of a larger scale infalling and rotating structure. The spatial resolution of the 3 mm data is worse, but even in the zoomed in continuum image of Fig. 2.3, the extension tracing the filament toward the south is already evident.

With the flux measured within the outer contour of the 1.3 mm dust continuum, we estimate the gas mass M and beam averaged column density N_{H_2} of the region following the methods of Hildebrand (1983) and Beuther et al. (2002a, 2005a). These estimates are under the assumptions that the dust continuum is optically thin at this wavelength, and that the gas to dust mass ratio is 100. For these calculations we assume a temperature of 20 K and a dust opacity index β of 2 which corresponds to an opacity of $0.35 \text{ cm}^2\text{g}^{-1}$ at 1.3 mm. Although Beuther & Steinacker (2007) determine components at two different temperatures, the 20 K we assume here is closer to the temperature of the component with the majority of the mass in IRDC 18223-3. We measure a total integrated flux of 130 mJy and a peak flux of 41 mJy bm^{-1} . From these values we derive a total mass of $120 M_\odot$ and a beam averaged column density of $3.8 \times 10^{24} \text{ cm}^{-2}$ corresponding to a peak visual extinction, $A_v(\text{mag})$, of ~ 4000 , where $A_v = N_{\text{H}_2}/0.94 \times 10^{21} \text{ cm}^{-2} \text{ mag}^{-1}$ (Frerking et al. 1982). Taking the uncertainties of the temperature and dust opacity into account, we estimate that the calculated mass and beam averaged column density for the compact structures detected here are accurate to within a factor of approximately 5.

It must also be noted that the mass estimate is heavily affected by missing flux in the in-

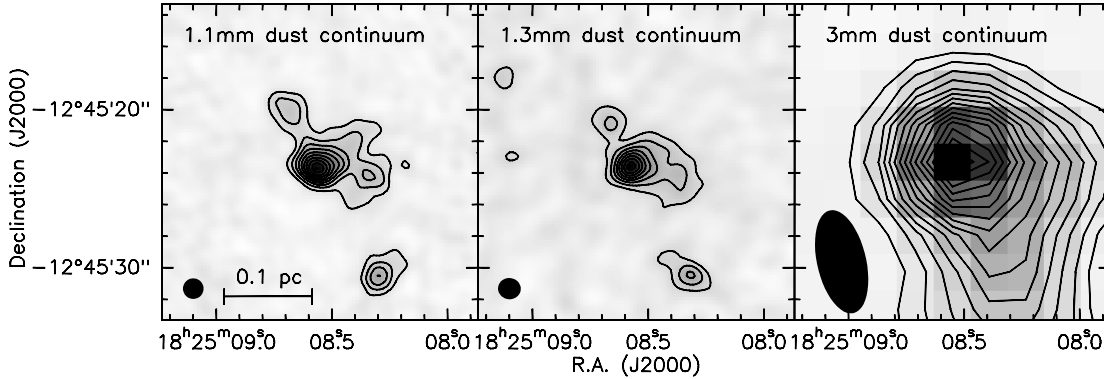


Figure 2.3: The 1.1 mm (SMA), 1.3 mm (SMA), and 3.4 mm (PdBI) dust continuum. The area displayed for all three panels is identical. Contours start at 3σ and increase in steps of 3σ where σ is 2.2, 1.6, and 0.15 mJy bm^{-1} for the 1.1, 1.3, and 3.4 mm continuum images respectively.

terferometer data. Comparing the flux from the 250 GHz single dish bolometer map (dotted contours in Fig. 2.1) with the 230 GHz SMA continuum flux, we estimate that without short spacing information, the interferometer filters out about 80% of the flux. Hence we recover only about 20% of the mass in our estimate. As a detection limit, we calculate a mass of $5.2 M_{\odot}$ and a column density of $5.3 \times 10^{23} \text{ cm}^{-2}$ at the 3σ ($5.7 \text{ mJy } \text{bm}^{-1}$) flux level. The interferometer data are not sensitive to structures less massive than this.

2.3.3 Outflow Properties

Figure 2.4 demonstrates that there is a large scale outflow in the northwest-southeast orientation. The morphology of the blueshifted CO component to the southeast is cone-shaped and likely is tracing the outer walls of the outflow cavity. There is also large, not very collimated blueshifted emission to the northwest of the source seen predominantly in the 30 m data. Although much less prevalent, we detect some redshifted emission on both sides of the primary 1.3 mm continuum peak. The fact that we detect red- and blueshifted emission on both sides of the driving source indicates that the outflow is roughly in the plane of the sky because as the outflow cavity widens, the near edge would appear blueshifted while the far edge would appear redshifted.

We detect SiO toward IRDC 18223-3 with the PdBI (See Figs. 2.2 and 2.5). This tracer of shocked material, especially in molecular outflows (Schilke et al. 1997), is consistent with the outflow orientation we determine from $^{12}\text{CO}(2-1)$ observations, and the southeastern SiO component coincides quite well with the southern edge of the blueshifted ^{12}CO cone-shaped emission. The slight difference in alignment between blue- and redshifted SiO emission shown in Fig. 2.5 and the CO outflow orientation indicated by the arrows overlaid in this figure could potentially arise from the presence of multiple outflows. Such a scenario would indicate the presence of an undetected secondary source. We discuss the possibility of multiplicity further in Section 3.4. Alternatively, the difference in morphology between SiO and CO may be explained

Table 2.3: Outflow parameters without inclination angle correction and corrected for an inclination of 20° with respect to the plane of the sky.

i	M_t	p	E	size	t	\dot{M}_{out}	F_m	L_m
[$^\circ$]	[M_\odot]	[M_\odot km/s]	[erg]	[pc]	[yr]	[M_\odot /yr]	[M_\odot km/s/yr]	[L_\odot]
13	150	1.7×10^{46}	0.45	37000	3.5×10^{-4}	4.0×10^{-3}	3.8	
20	440	1.5×10^{47}	0.48	14000	9.6×10^{-4}	3.2×10^{-2}	89	

Entries include inclination i , total outflow mass M_t , momentum p , energy E , size, outflow dynamical age t , outflow rate \dot{M}_{out} , mechanical force F_m and mechanical luminosity L_m . Inputs are discussed in the text.

by precession of the jet/outflow in which the SiO emission traces the current jet component's location. The fact that SiO tends to trace the more collimated jet component whereas CO traces the less collimated outflow cavity provides support that this explanation is plausible. The CO data indicate that the outflow is in the plane of the sky, but a slight inclination is necessary to explain the fact that we detect blueshifted SiO emission predominantly to the northwest and redshifted emission predominantly to the southeast indicating that the jet component is not exactly in the plane of the sky. In either case, the SiO data are consistent with the CO outflow to the extent that any disk component, if present, should have a position angle roughly 45° east of north.

Applying the methods of Cabrit & Bertout (1990) we derive properties of the system such as outflow mass, dynamical age, and outflow energy. These calculations assume that the line wing ratio of $^{13}\text{CO} (2-1)/^{12}\text{CO} (2-1)$ remains constant over the entire outflow. Based on our single dish data which is consistent with the data of Choi et al. (1993), we adopt a value for this ratio of 0.1. Based on measuring a CO emission spatial extent of $25''$ from the central peak and adopting maximum velocities of 10.5 km s^{-1} and 13 km s^{-1} for the red- and blueshifted lobes respectively, the derived characteristics of the outflow associated with IRDC 18223-3 are listed in Table 2.3.

The true velocity and spatial extent of an outflow must include a correction for the inclination of the system from the plane of the sky. Thus any outflow parameters derived from the measured velocity and outflow extent also depend on this correction. Based on the observation of blueshifted ^{12}CO emission on both sides of the central source, we interpret this to mean that the outflow is roughly in the plane of the sky. In this interpretation, our measurement of the CO spatial extent is a reasonable approximation of the true outflow extent and the effect of inclination on the calculated outflow properties should be small. The velocity correction, on the other hand, may be significant for inclinations close to 0° , leading to a much shorter timescale than that listed in Table 2.3. In turn, the outflow rate, mechanical force and mechanical luminosity may be significantly larger than the values given in Table 2.3 since these values depend on the outflow timescale.

We compare the quantities presented in Table 2.3 with the single dish study of massive outflows in Beuther et al. (2002b). Our calculated mechanical force (F_m), outflow mass (M_t), outflow rate (\dot{M}_{out}) and luminosity (L_m) place IRDC 18223-3 well within the massive regime

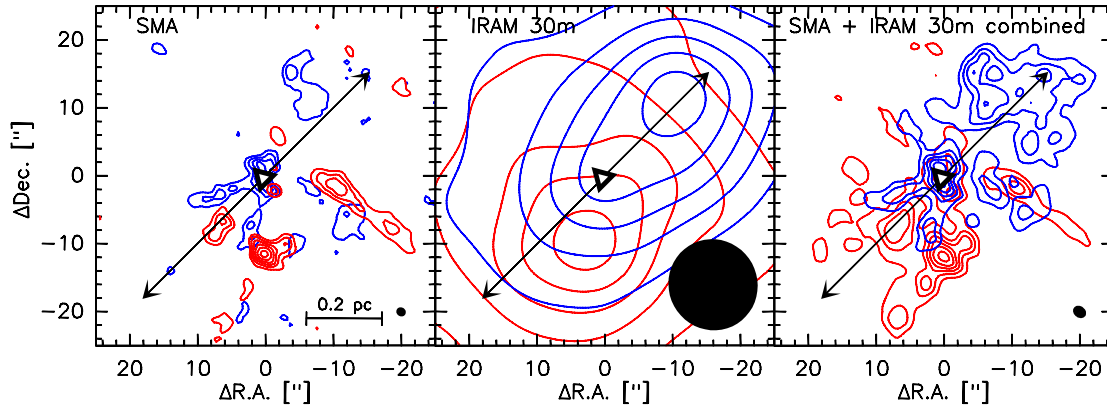


Figure 2.4: $^{12}\text{CO}(2-1)$ integrated maps of IRDC 18223-3 from SMA, IRAM 30 m, and SMA + IRAM 30 m combined in the *left*, *center*, and *right* panels respectively. Panels that include SMA data contain both extended and compact configuration observations. We define the outflow orientation (indicated by the arrows) by the blueshifted interferometer component. In each panel, the 1.3 mm continuum peak is indicated by the triangle, and the beam is included in the lower right corner. *Left*: blueshifted emission (blue contours) integrated over velocities of 38.5-43.5 km s^{-1} in steps of 3σ starting at 3σ where $\sigma=0.12 \text{ Jy bm}^{-1}\cdot\text{kms}^{-1}$. Redshifted emission (red contours) integrated over velocities of 50-54 km s^{-1} in steps of 2σ starting at 3σ where $\sigma=0.17 \text{ Jy bm}^{-1}\cdot\text{kms}^{-1}$. *Center*: blueshifted emission (blue contours) integrated over velocities of 36.5-43.5 km s^{-1} in steps of 1σ starting at 1σ where $\sigma=6.4 \text{ Jy bm}^{-1}\cdot\text{kms}^{-1}$. Redshifted emission (red contours) integrated over velocities of 46.5-53.5 km s^{-1} in steps of 1σ starting at 1σ where $\sigma=6.9 \text{ Jy bm}^{-1}\cdot\text{kms}^{-1}$. *Right*: blueshifted emission (blue contours) integrated over velocities of 36-44 km s^{-1} in steps of 6σ starting at 3σ where $\sigma=0.14 \text{ Jy bm}^{-1}\cdot\text{kms}^{-1}$. Redshifted emission (red contours) integrated over velocities of 50-56 km s^{-1} in steps of 6σ starting at 3σ where $\sigma=0.14 \text{ Jy bm}^{-1}\cdot\text{kms}^{-1}$.

of Figs. 4a (F_m vs. M_{core}) and 7 (M_t vs. M_{core}) and at the lower end of the high-mass regime in Figs. 4b (F_m vs. L_m) and 5 (\dot{M}_{out} vs. L_m) of Beuther et al. (2002b). In all of these figures, IRDC 18223-3 is well above the low mass sources from the studies by Cabrit & Bertout (1992) and Bontemps et al. (1996). Both of the figures in which IRDC 18223-3 is situated near the lower end of the high-mass regime are luminosity dependent. The position of IRDC 18223-3 in these plots is a reflection of the source's youth and we expect that the luminosity will increase with time eventually shifting the source well into the regions occupied by the high-mass outflows in Figs. 4b and 5. This general agreement with the properties of the high-mass sources further supports the interpretation that this outflow is associated with a source in the massive regime. The outflow parameters derived here confirm previous suggestions (Beuther & Steinacker 2007) that this truly is a massive star in the making.

It is also interesting to note that in the SiO integrated map in Fig. 2.2, there is an emission peak approximately $7''$ west of the main peak and Fig. 2.5 demonstrates that this includes both red- and blueshifted velocities. We also detect a collimated redshifted CO feature situated westward of the primary dust continuum peak. Puzzlingly, we do not detect a corresponding blueshifted counterpart, nor a millimeter source associated with this CO feature, but it may have a connection to the SiO detection as it appears to originate close to where SiO has a secondary peak. However, this is quite speculative, and we refrain from further comment and interpretation of this collimated redshifted CO emission.

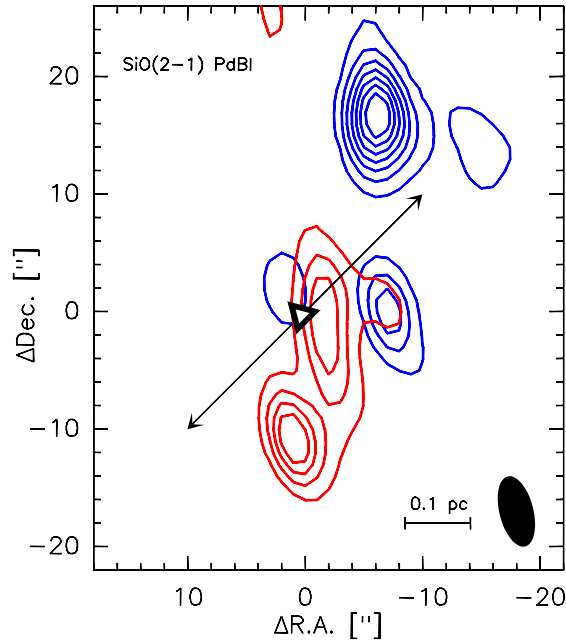


Figure 2.5: The SiO(2-1) integrated map. Again the triangle symbol marks the position of the dust continuum peak. The arrows indicate the orientation of the $^{12}\text{CO}(2-1)$ outflow as shown in Fig. 2.4. The PdBI beam is included in the lower right corner. Blueshifted emission (blue contours) integrated over velocities of 35-39 km s^{-1} in steps of 4σ starting at 3σ where $\sigma=0.011 \text{ Jy bm}^{-1}\cdot\text{kms}^{-1}$. Redshifted emission (red contours) integrated over velocities of 50-54 km s^{-1} in steps of 4σ starting at 3σ where $\sigma=0.011 \text{ Jy bm}^{-1}\cdot\text{kms}^{-1}$.

2.3.4 Age of the System

Compared to other massive star formation regions, IRDC 18223-3 is extremely young as evidenced by the molecular properties described in Beuther et al. (2005b). The C^{18}O line width measured at the main continuum peak of the SMA data is 1.7 km s^{-1} whereas it is typically a factor of two to five times larger for molecules that trace similar densities in more evolved massive star formation regions (see e.g. Bronfman et al. 1996; Hatchell et al. 1998; Hofner et al. 2000; Beuther et al. 2002a). In the two secondary continuum peaks, the C^{18}O line width is smaller still. The C^{18}O line width at the peak to the northeast is 0.94 km s^{-1} and in the southwest peak it is 0.60 km s^{-1} . While the line width at the center is less than 2 km s^{-1} , it is still larger than the line widths in the secondary peaks confirming that the outflow seen in $^{12}\text{CO}(2-1)$ originates from the primary peak. The quite narrow central line width that we measure, along with the paucity of chemical species present toward the center, support the interpretation that IRDC 18223-3 is at a very young evolutionary stage.

When the luminosity published by Beuther & Steinacker (2007) is considered in the framework of the models by Krumholz et al. (2007), estimates for the age of the system are less than $\sim 10,000$ years. Here we estimate the outflow dynamical age of IRDC 18223-3 to be approximately 37,000 years.

This timescale calculation depends on the tangent of the outflow's inclination angle (with

0° being in the plane of the sky). Applying a correction for inclination could potentially result in a much younger age than the 37,000 years which we calculate here. As seen in Table 2.3 for example, with an inclination angle of 20° with respect to the plane of the sky, the age estimate decreases by a factor of nearly 3.

Both the age estimate based on luminosity and the outflow dynamical age are subject to large uncertainties making it difficult to pinpoint the true age. We are rather in support of interpreting the source simply as very young based on the non-detection at infrared wavelengths as well as its not very evolved chemical state.

2.3.5 Rotational Structure

In this section we present maps of the velocity distribution weighted by intensity of the molecules in our SMA data set that are associated with tracing the physical conditions in dense gas.

The velocity moment map of C¹⁸O (Fig. 2.6) exhibits a velocity gradient of approximately 2 km s⁻¹ from south to north. The observed gradient is neither aligned with nor orthogonal to the outflow orientation, presumably because this tracer of denser regions is being strongly affected by infall and the outflow itself. The position angle of the observed gradient differs by about 30° with respect to the ¹²CO outflow orientation. As C¹⁸O is an isotopologue of ¹²CO, it may indeed be tracing a disk-like structure although the observed gradient may be influenced by infall and the outflow. This is not an entirely unexpected result despite the fact that C¹⁸O is optically thin and not a good outflow tracer.

Methanol is well documented as a molecule that traces cores, shocks, and masers in star formation regions (e.g., Jørgensen et al. 2004; Beuther et al. 2005c; Sobolev et al. 2007). It has also been reported as a lowmass disk tracer (e.g. Goldsmith et al. 1999), yet it has not previously been associated with tracing disks in massive star formation. In the velocity moment map of the CH₃OH(6₀-5₀) line at 290.110 GHz (middle panel of Fig. 2.6), we see a flattened, elongated rotating structure perpendicular to the outflow axis. The structure evident here is consistent with the velocity moment maps of the next two strongest methanol lines, 229.759 GHz and 290.070 GHz. The remaining methanol lines in our spectral setup (listed in Table 2.1) are too weak to be able to justify similar statements. The approximately 7.5'' extent corresponds to a major axis extent of 28,000 AU at the given distance of 3.7 kpc. Although this is rather large to be a disk, the narrow velocity range of 3 km s⁻¹ coupled with the large spatial extent perpendicular to the outflow support an interpretation that this is a large rotating and infalling core similar to the toroids described in the recent review by Cesaroni et al. (2007). There is also a high velocity component in the northwest corner of the CH₃OH velocity moment map which coincides with the outflow and is likely associated with the extension seen in the 1.1 mm dust continuum overlay of Fig. 2.6.

In Fig. 2.7, we present the position-velocity diagrams of the CH₃OH and N₂H⁺ emission. The cuts go through the peak of the dust continuum and have position angles along the velocity gradients seen in the moment maps. In the N₂H⁺ position-velocity diagram, it is apparent that

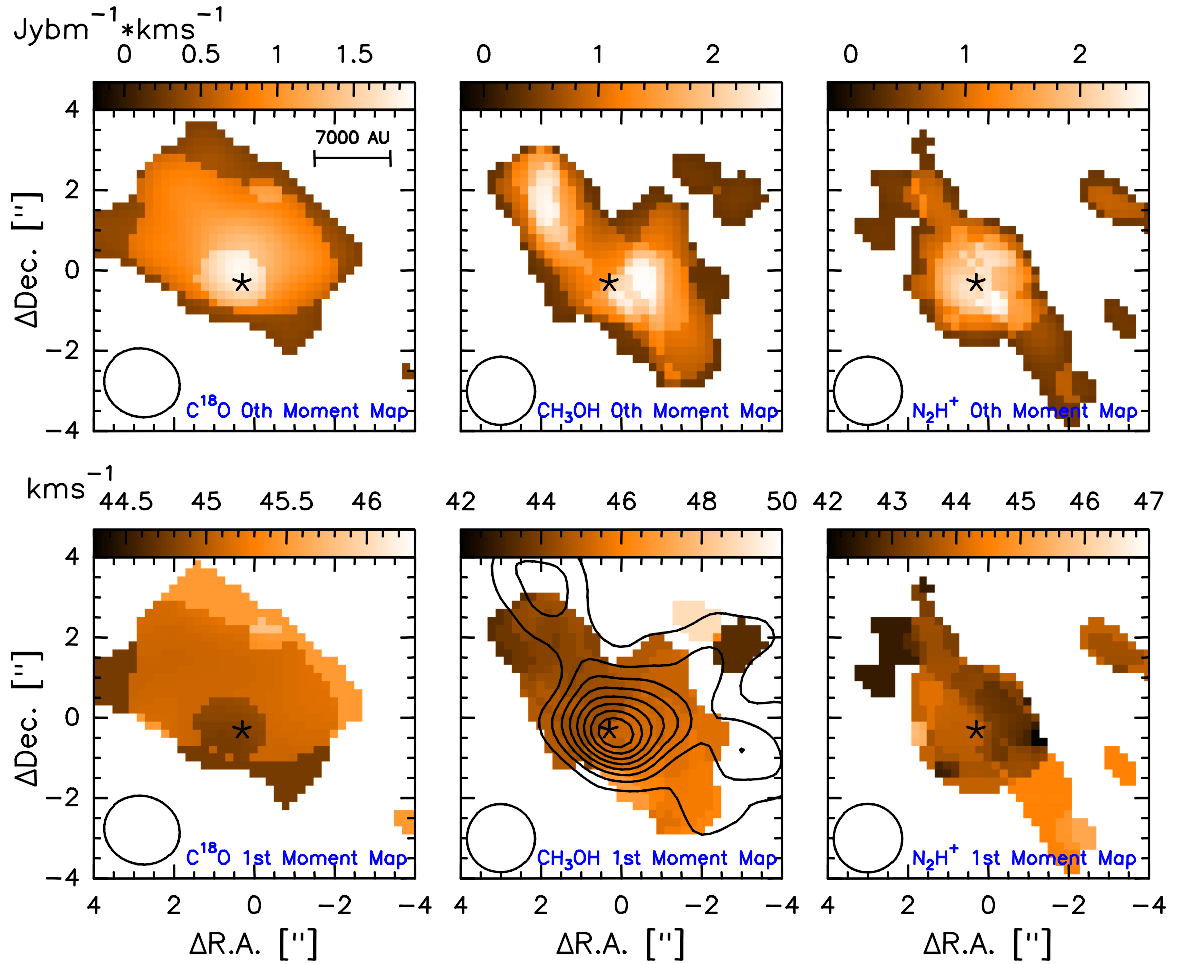


Figure 2.6: *Upper Row:* $\text{C}^{18}\text{O}(2-1)$, $\text{CH}_3\text{OH}(6_0-5_0)$ A, and $\text{N}_2\text{H}^+(3-2)$ total intensity (0th) moment maps. *Lower row:* $\text{C}^{18}\text{O}(2-1)$, $\text{CH}_3\text{OH}(6_0-5_0)$ A, and $\text{N}_2\text{H}^+(3-2)$ velocity (1st) moment maps. The high velocity component toward the northwest corner of the CH_3OH velocity moment map is also seen as an extension in the 1.1 mm dust continuum overlaid on the middle panel. The contours start at 5σ and increase in steps of 5σ where σ is 2.25 mJy bm^{-1} . All moment maps were clipped at the six sigma level of the respective line's intensity map. The star symbol indicates the position of the 1.3 mm dust continuum peak. The beam size is shown in the lower left corner of each plot.

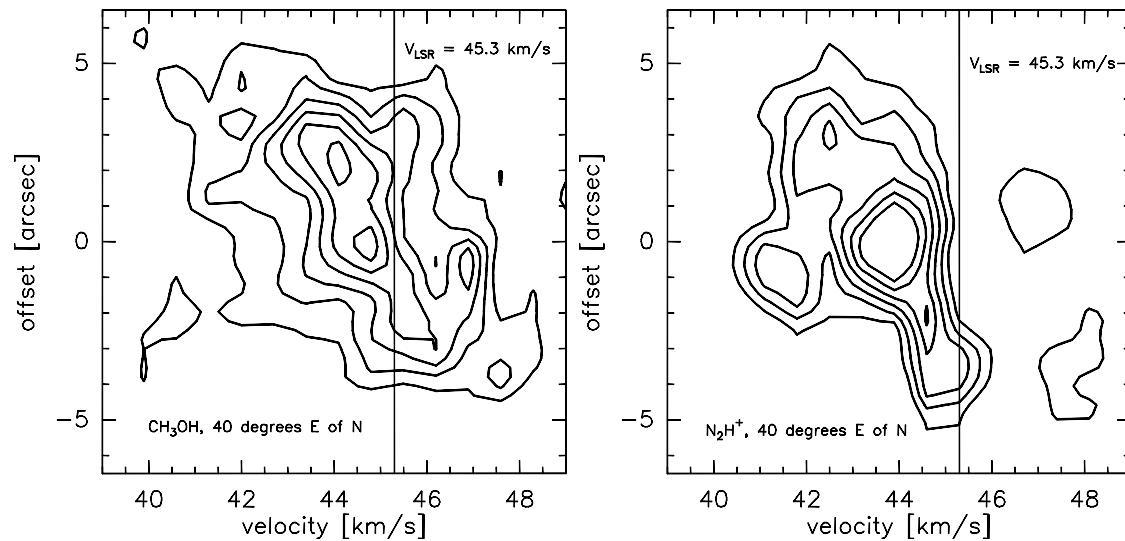


Figure 2.7: Position-velocity diagrams derived for cuts along the observed velocity gradient. The offset refers to the distance along the cut from the dust continuum peak. The rest velocity of 45.3 km s^{-1} is marked in both plots. Contours for both diagrams start at 0.16 Jy bm^{-1} and increase in 0.16 Jy bm^{-1} steps.

we suffer from missing flux especially around the velocity of rest and at more redshifted velocities, but we still see an indication for the same trends as in the CH₃OH position-velocity diagram. Because of the larger effect of missing flux in N₂H⁺ compared to CH₃OH (see Fig. 2.7), we do not further analyze this molecule suited for probing early stages of star formation, but rather concentrate on CH₃OH.

Although the position-velocity diagrams do not exhibit Keplerian velocity signatures, they are consistent with the velocity moment maps in the sense that we see the largest velocities furthest from the center. In Keplerian motion, the equilibrium condition between gravitational and centrifugal forces means that the velocities at large distances from the source should be lower than those closer to the center. One explanation for the deviation from Keplerian motion is that we do not see all the way to the center due to optically thick emission, and hence see only rotation of the outer envelope. However, without optical depth information, we cannot assume this to be the case, so we interpret the observed velocity gradient simply as non-Keplerian rotation of a large structure perpendicular to the outflow orientation. This should not come as a surprise as the mass of the central source is likely much less than the mass of the rotating structure.

2.3.6 Theoretical Modeling

Assuming optically thin line emission, we modeled the velocity gradient seen in the CH₃OH velocity moment map. The modeling was done using the Ulrich Model (Ulrich 1976; Keto 2007) which is an angular momentum conserving mass inflow model that includes gravity and an isothermal rotating envelope. We calculated the velocity and density along the line of sight

and then multiplied these together to produce the velocity distribution. The model does not include a disk because this adds another parameter which we cannot distinguish between due to observational limitations. The input parameters we used were determined from the CH₃OH moment map. We measure an observed rotation speed of 1.5 km s⁻¹ at 14,000 AU (3.8'' at the given distance of 3.7kpc). We chose a global mass infall rate for the core of 10⁻³ M_⊙ yr⁻¹ which is consistent with the slightly lower accretion rates calculated in Section 2.3.3. The system in our current studies does not fit well into the picture of Keplerian rotation that describes low-mass accretion disks (Dutrey et al. 2007), but in order to get a rough estimate of the mass in the rotating structure we make the assumption that rotational and gravitational forces are balanced at the outer edge of the disk. We then calculate the mass that is in gravitationally bound rotational motion within a given radius, r , using the following equation:

$$M_{rot} = \frac{\delta v^2 r}{G} \quad (2.1)$$

$$M_{rot}[M_{\odot}] = 1.13 \cdot 10^{-3} \times \delta v^2[\text{km/s}] \times r[\text{AU}] \quad (2.2)$$

We take r to be 14,000 AU, and δv to be 1.5 km s⁻¹, half the extent of emission and half the velocity range seen in the CH₃OH velocity moment map. From these values, we estimate M_{rot} to be 36 M_⊙. The rather low luminosity of this source leads to the interpretation that this mass is strongly dominated by a larger rotational structure opposed to a central object. In addition to the large uncertainties (typically within a factor of 5) associated with mass estimates in general, the discrepancy between the mass estimate of 120 M_⊙ from the continuum emission (Section 2.3.2) and the mass calculated here can be explained by the fact that the system is not rotationally supported but rather infalling, as we assume for the modeling.

The resulting density distribution and velocity field along with the combination of these into the velocity distribution are shown in Fig. 2.8. In these plots the disk formation radius, R_D , is the radius in the midplane that has the highest density and corresponds to the point at which the rotational force balances the gravitational force. At the disk formation radius, the Keplerian velocity is 2.1 km s⁻¹. We do not observe Keplerian velocity signatures in the position-velocity diagrams (Fig. 2.7), so we do not expect to measure the Keplerian velocity predicted by the model. Although we do not exactly fit our quantitative parameters, this simple model of rotationally supported infall reproduces our observations well.

In order to make a more direct comparison between the theoretical model and our observations, we have convolved the model to the 1.7'' angular resolution of the data and rotated it counterclockwise by 45° such that it has the same orientation as the observed velocity gradient. Figure 2.9 presents the smoothed and rotated model and the CH₃OH velocity moment map side by side. We emphasize that this model is not meant to be a best fit of the data, but rather to show that our interpretation presented here is physically plausible.

Keplerian rotation signatures are not detected in this and other regions of massive star formation (see Cesaroni et al. 2007). One scenario that could explain this is that as the core

collapses, it fragments into smaller condensations and forms several stars, each with accretion disks not necessarily aligned with the parental core's rotational axis. If this were the case, we would expect to see a more chaotic velocity structure as well as more outflow signatures. Additionally, this may not be physically reasonable in light of the modeling by Krumholz et al. (2007, 2009). In these models, multiple stars form within the same accretion disk meaning that the rotational axis should be similar for all sub-sources. Since a driving source is required to power the outflow, we suspect that a true Keplerian accretion disk may have formed at the center on scales we cannot observationally resolve.

One interpretation of the observed lobes to the northeast and southwest in the millimeter continuum is that there are several unresolved sources in the vicinity. If these objects are all part of an inward spiraling structure, this might be mistaken for a velocity gradient across them. However, our ability to reproduce the gradient in the CH₃OH velocity moment map through successful modeling provides evidence against this interpretation and rather in favor of a scenario in which a single component is surrounded by a large rotating object. In order to discriminate between these scenarios mentioned here, even higher spatial resolution images of the system would be necessary. Further studies of spectral lines probing deeper into the core would also likely prove to be helpful.

2.4 Conclusions

The Infrared Dark Cloud 18223-3, a source at the onset of massive star formation, has been observed with multiple submillimeter observatories. Despite being at a very early stage in the evolutionary process, we detect a molecular outflow and evidence for a large rotating object perpendicular to the outflow.

This region likely represents one of the earliest stages of disk formation. IRDC 18223-3 exhibits a large rotating and flattened envelope structure which we suspect is one of the earliest detectable stages in the evolutionary sequence of accretion disks. In this framework, the structure we see and have described here will continue contracting into a true accretion disk as time passes.

The combined SMA and 30 m data reveal a well defined northwest-southeast outflow orientation. To the southeast of the 1.3 mm continuum peak, we see a cone-like blueshifted component and the northwest is dominated by a broader blueshifted component. While it is less clear what is happening in the redshifted regime, the blueshifted components indicate that we are likely looking at a system that is roughly in the plane of the sky. From this we deduce that the likely disk orientation would be approximately edge on and that the associated velocity gradient would be in the northeast-southwest direction.

Based on the observed outflow properties, we find that calculated parameters are consistent with a massive driving source. Although the central source is not very massive at this point in time, the outflow characteristics provide a strong indication that this star will evolve into the

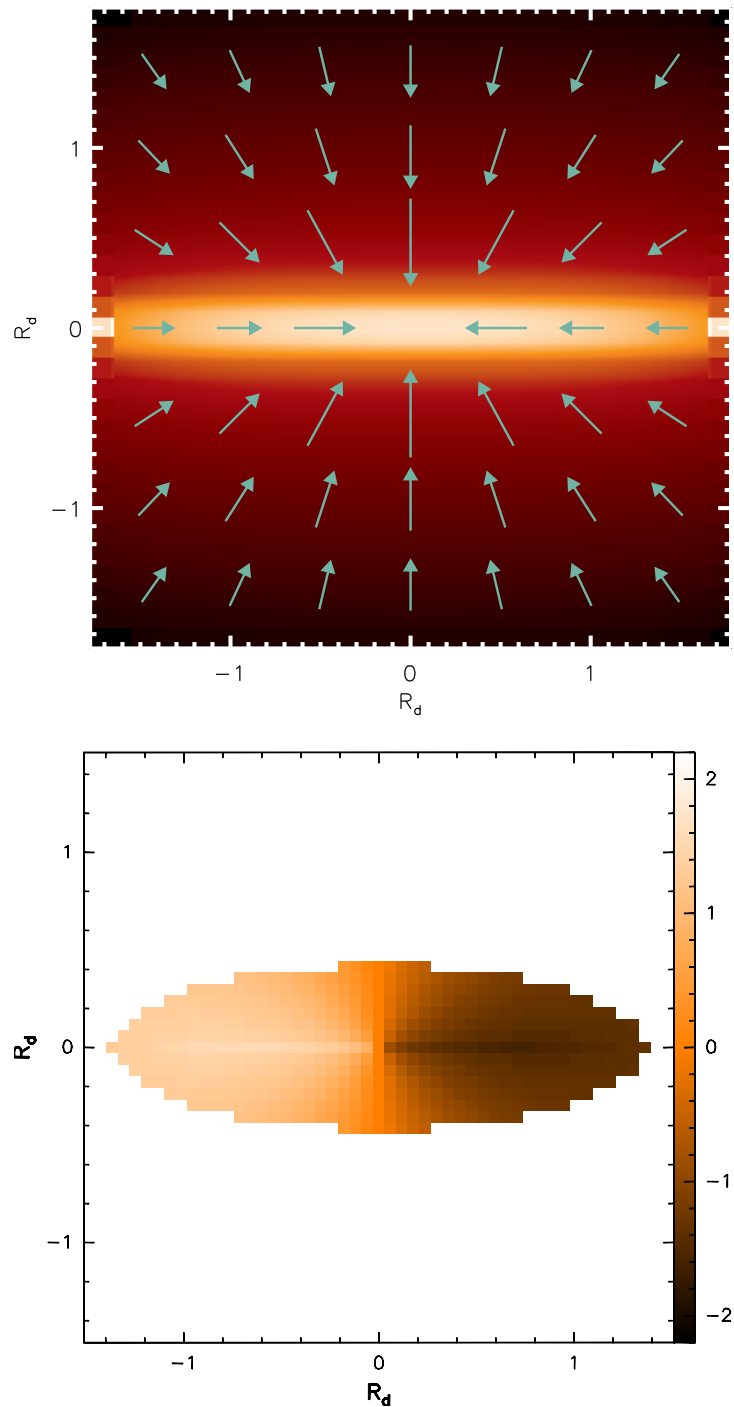


Figure 2.8: Results of modeling the velocity gradient seen in CH_3OH with the Ulrich infall model. R_d is the radius, and $1 R_d$ corresponds to 10,000 AU. *Upper:* the density distribution overlaid with the velocity field vectors. The velocity vectors vary between 0.5 and 1.0 km s^{-1} in length, and the densities vary between 9.4×10^5 and $3.9 \times 10^7 \text{ cm}^{-3}$. The logarithmic plotting of the density resembles a disk, but we have not included one in this modeling. *Lower:* the velocity and density distributions above multiplied together then averaged along the line of sight to reproduce the velocity gradient seen in the CH_3OH velocity moment map.

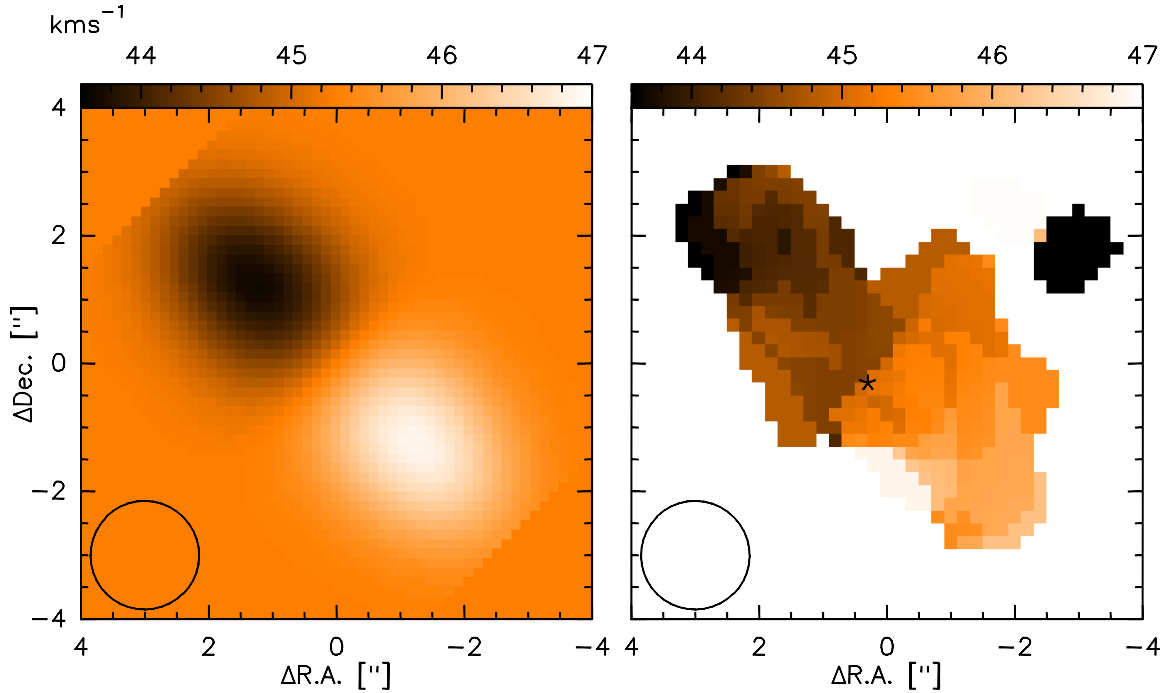


Figure 2.9: *Left*: the model shown in the lower panel of Fig. 2.8 after convolving to the $1.7''$ resolution of the data and rotating counterclockwise by 45° into alignment with the observed velocity gradient. *Right*: the CH_3OH velocity moment map as in Fig. 2.6. The velocity range has been modified to exclude the high velocity components seen in the northwest of Fig. 2.6 so that a more direct comparison to the model can be made.

massive regime.

Indeed we do see velocity gradients in CH_3OH and N_2H^+ , although they are observed over a very large spatial distance and a relatively small velocity range. On the order of 20,000 AU in size, the large rotating core we currently detect is much larger than other disk or disk-like structures around similar low luminosity intermediate to high mass star forming regions published in the literature. For instance, the disk associated with IRAS 20126+4104 is less than a third the size of the structure we observe in IRDC 18223-3 (Cesaroni et al. 2005). The reported disks around G192.16-3.82 (Shepherd et al. 2001) and IRAS 18089-1732 (Beuther et al. 2004) are smaller still. We thus suspect that CH_3OH and N_2H^+ are actually tracing the outer edges of an infalling toroid. This rotating toroid likely plays an important role in feeding an accretion disk within the unresolved central region and may decrease in size over time as the outer edges dissipate or contract leading to growth of the disk. Hence we see here potentially the earliest stages of the disk formation process. As there is not much known about CH_3OH as a tracer of massive disks, one possibility is that it may be a good tracer for disk kinematics only at very early evolutionary stages, but that other hot core molecules such as CH_3CN , for example, may be better for more evolved massive star formation regions.

Using the Ulrich Model for mass infall we have successfully reproduced the velocity gradient observed in methanol. This agreement between model and observations further enhances the argument that the rotation we see results from a single flattened rotating entity rather than

multiple sources or other complicated scenarios.

Similarly, we detect a velocity gradient in C^{18}O that is not aligned with the ^{12}CO outflow axis. However, the spatial scale is large, and the velocity range is even smaller than in CH_3OH and N_2H^+ . In this case, since C^{18}O is an isotopologue of the standard outflow tracer, ^{12}CO , it is likely that the velocity gradient we see is being influenced by infall motion or the outflow itself which would tend to shift the observed gradient toward the direction of the outflow orientation.

The results we have presented further support the idea that IRDCs are sources undergoing the early stages of high-mass star formation. Thus IRDCs provide ideal sites to study the birth of massive stars.

Chapter 3

A high mass dusty disk candidate: the case of IRAS 18151-1208

*This chapter is based on a paper submitted to the Astrophysical Journal:
Fallscheer, C., Beuther, H., Sauter, J., Wolf, S. & Zhang, Q. 2009, submitted*

Abstract

Many questions remain regarding the properties of disks around massive protostars. Here we present the observations of a high mass protostellar object including an elongated dust continuum structure perpendicular to the outflow. Submillimeter Array 230 GHz line and continuum observations of the high mass protostellar object IRAS 18151-1208 along with single dish IRAM 30 m observations afford us high spatial resolution ($0.8''$) as well as recovery of the extended emission that gets filtered out by the interferometer. The observations of ^{12}CO confirm the outflow direction to be in the southeast-northwest direction, and the 1.3 mm continuum exhibits an elongation in the direction perpendicular to the outflow. We model the physical parameters of the elongated structure by simultaneously fitting the observed spectral energy distribution (SED) and radial brightness profile using the 3D Radiative Transfer code MC3D. From these results we conclude that using the same power law parameters as were used in the low mass case for the density and flaring, and scaling up the quantitative parameters that successfully modeled the circumstellar disks of several T Tauri stars, we can also reproduce the observations of this high mass protostellar object. We also calculate that a region within the inner 40 AU of such a high mass disk is stable under the Toomre criterion. Implications on high mass star formation are discussed.

3.1 Introduction

In contrast to low mass T Tauri stars and even intermediate mass Herbig stars of which numerous examples exist where circumstellar disks have been detected (see review by Watson et al. 2007), the role of disks in the case of massive star formation is not yet well defined. In the low mass case, it is clear that molecular outflows fed by circumstellar accretion disks are an integral part of the formation process. While the occurrence of massive molecular outflows is well established in cases of massive star formation, evidence for the analogous driving structures, namely, massive accretion disks, has only tentatively been identified (see review by Cesaroni et al. 2007).

In a concerted effort to shed some light on accretion disks in high mass star formation, we observed a sample of seven candidates with the Submillimeter Array (Zhang et al. *in prep*). The high mass protostellar object IRAS 18151-1208 is one of the sources included in this study. This source was also included in the single dish survey of IRAS sources conducted by Sridharan et al. (2002); Beuther et al. (2002a), and has also been observed with single dish telescopes by Marseille et al. (2008). IRAS 18151-1208 is at a distance of 3.0 kpc and has a luminosity of approximately $10^4 L_{\odot}$ (Sridharan et al. 2002).

Previous single dish observations (Beuther et al. 2002b) suggested the presence and general morphology of outflow in the region. However, data quality was not good enough to observe specific details. Narrow-band H_2 ($\lambda = 2.122 \mu\text{m}$) observations (Davis et al. 2004) of IRAS 18151-1208 show evidence of two collimated molecular outflows originating from two separate sources. In the case of low mass star formation, it is clear that accretion disks play the role of outflow-driver. However, in the high mass regime, observations of scaled up versions of these low mass accretion disks are rare (Cesaroni et al. 2007). Our goal is to see whether a scaled-up version of a disk modeling scheme that successfully reproduces the observations of disks around T Tauri stars can be applied in the case of a massive protostellar object, namely IRAS 18151-1208.

The T Tauri star IRAS 04302+2247, nicknamed the ‘‘Butterfly Star’’ because of its butterfly-shaped morphology, is a Class I source with a well-defined circumstellar disk. Wolf et al. (2003, 2008) model the circumstellar environment of this source using a Monte Carlo 3D (MC3D) Radiative Transfer code. Similarly, the disk in the Bok globule CB 26 (Sauter et al. 2009) has also been observed and modeled. CB 26 is also a Class I young stellar object destined to become a low mass star with an edge-on circumstellar disk. Additionally, a handful of other edge-on disks around T Tauri stars have been modeled using a similar technique [e.g. HK Tau (Stapelfeldt et al. 1998), HV Tau (Stapelfeldt et al. 2003), and IM Lupi (Pinte et al. 2008)]. On the theoretical side, Whitney et al. (2003) use a similar Monte Carlo radiative transfer approach to test various envelope/disk geometries for Class I sources. While theoretical descriptions such as Whitney et al. (2003) and observational studies (Sicilia-Aguilar et al. 2006, for example) of low mass T Tauri disks are relatively well developed, such a complete picture is missing in the high mass regime.

Table 3.1: SMA observation parameters. Entries include the date of observation, the array configuration, the calibrators, the synthesized beam obtained after inverting and cleaning the data, and the 1σ continuum noise level.

Date	Freq [GHz]	Config.	Calibrators			beam [$''$]	rms_{cont} [mJy/bm]
			Bandpass	Phase/Amp.	Flux		
2007 May 17	230	very ext.	3C273	1743-038 & 1911-201	none		
2007 Jul 08	230	comp.	3C273	1743-038	none		
	230	comb.				0.8x0.7	2

Table 3.2: Observed lines

Transition	Rest Frequency [GHz]	E_{upper} [K]
$\text{C}^{18}\text{O } 2 \rightarrow 1$	219.560	16
$\text{SO } 6_5 \rightarrow 5_4$	219.949	35
$^{13}\text{CO } 2 \rightarrow 1$	220.399	16
$\text{CH}_3\text{OH } 8_{-1} \rightarrow 7_0 \text{ E}$	229.759	89
$\text{CO } 2 \rightarrow 1$	230.538	17

3.2 Observations

3.2.1 Submillimeter Array

IRAS 18151-1208 was observed at 1.3 mm with the Submillimeter Array (SMA)¹ in the compact and very extended configurations on 2007 July 8 and 2007 May 17 respectively. Observations in the compact array were made under stable and excellent weather conditions, with a $\tau(230 \text{ GHz})$ of approximately 0.07. The very extended configuration observations were made under observing conditions with a $\tau(230 \text{ GHz})$ of 0.12. The combination of these two configurations provided baseline lengths varying between 14 and 520 meters corresponding to $10 \text{ k}\lambda$ and $400 \text{ k}\lambda$ at 1.3 mm. The phase reference used was $\text{RA}(J2000) = 18^{\text{h}}17^{\text{m}}57.1^{\text{s}}$ and $\text{Dec}(J2000) = -12^{\circ}07'22''$ with the emission peak approximately $17''$ east of these coordinates. We adopted a rest velocity $v_{\text{LSR}} = 32.8 \text{ km s}^{-1}$ (Sridharan et al. 2002).

For both data sets, the quasar 3C273 was used as the bandpass calibrator, and 1743-038 was used for phase and amplitude calibration. The quasar 1911-201 was used as an additional phase and amplitude calibrator in the very extended data set. After combining the SMA data sets, the synthesized beam size of the continuum is $0.9'' \times 0.7''$. A summary of the observations is given in Table 3.1. Spectral resolution of 0.55 km s^{-1} was obtained over a 4 GHz bandwidth divided

¹The Submillimeter Array is a joint project between the Smithsonian Astrophysical Observatory and the Academia Sinica Institute of Astronomy and Astrophysics, and is funded by the Smithsonian Institution and the Academia Sinica.

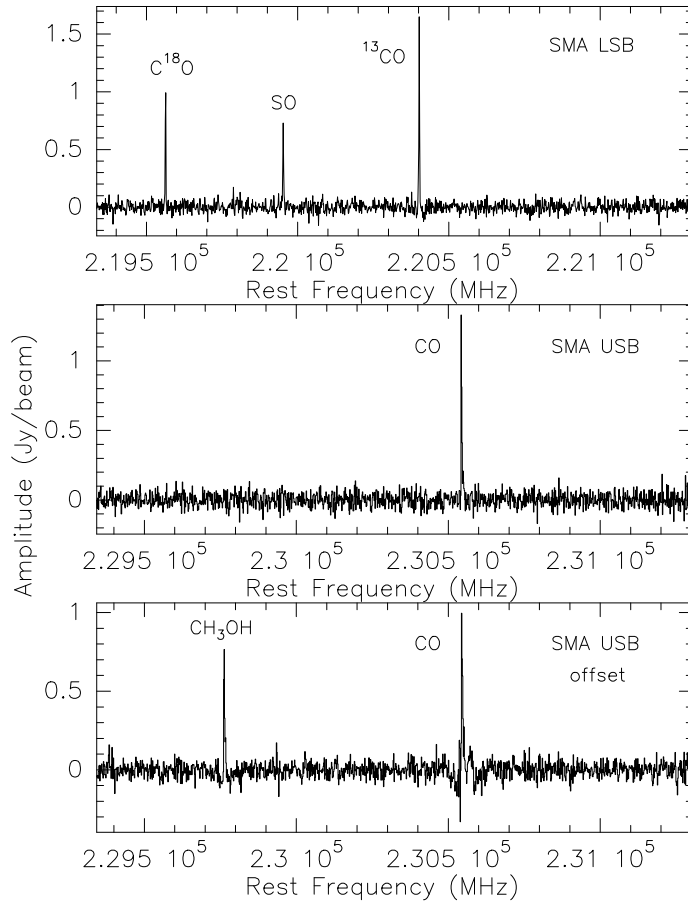


Figure 3.1: The spectra from the SMA. *Upper*: the lower side band spectrum at the center of the 1.3 mm dust continuum peak of the combined compact and very extended configuration data. *Middle*: the same as above except for the upper side band. *Lower*: the upper side band at a position approximately $7''$ northeast of the continuum peak only including the compact configuration data.

into a lower and upper sideband separated by 10 GHz (see Fig. 3.1) with central frequencies of 219.6 and 230.5 GHz respectively. The lines observed by the SMA are listed in Table 3.2.

3.2.2 Pico Veleta 30 m Telescope

The shortest baseline in our SMA datasets is 14 m which corresponds to a spatial scale of $19''$. The SMA is not sensitive to structures larger than this, so supplementary short spacing information was obtained in the on-the-fly mode with the HERA receiver on the IRAM 30 m telescope near Granada, Spain. These observations were made on 12 November 2006 under very good observing conditions with $\tau(230)$ of 0.07. The receiver was tuned to 230.5 GHz centered on the $^{12}\text{CO}(2-1)$ line. A spectral resolution of 0.4 km s^{-1} was obtained with a channel spacing of 0.3 MHz. The spectra were first processed with CLASS90 of the GILDAS package, then further analyzed with GREG. While the single dish data can in principle be combined with the interferometer data, their quality is not good enough to do so in this case, so we analyze the data sets independently.

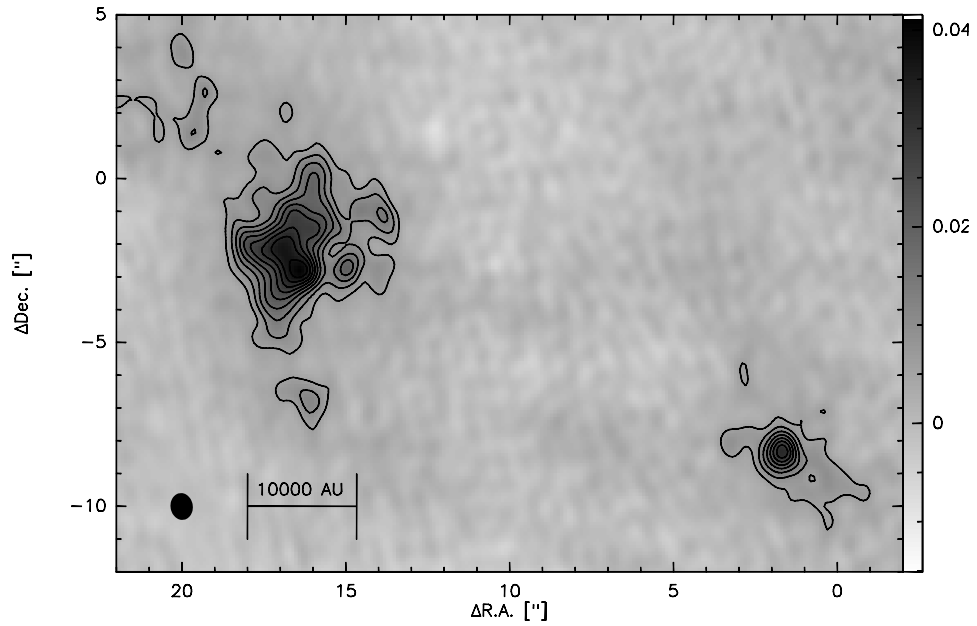


Figure 3.2: The 1.3 mm dust continuum. The size of the beam is indicated in the lower left corner. Contours start at 3σ increasing in steps of 2σ where σ is 2 mJy/beam.

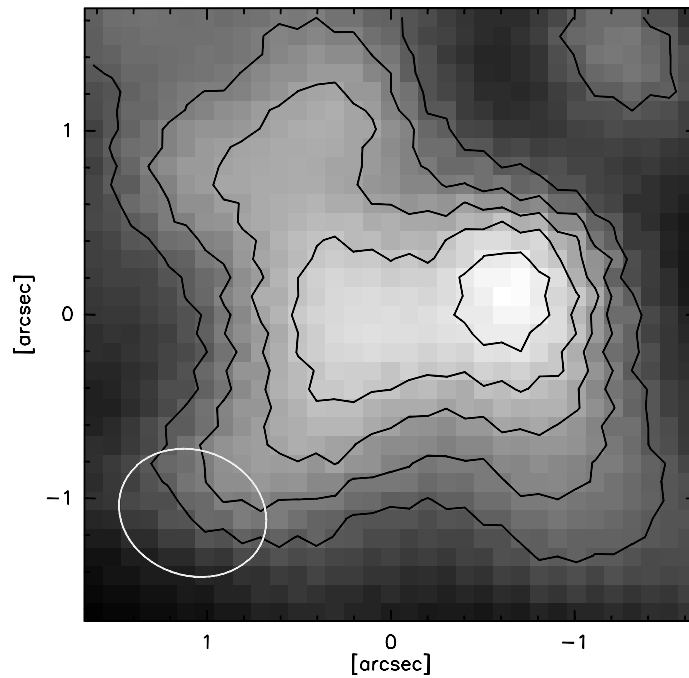


Figure 3.3: A zoomed in view of the primary peak of the 1.3 mm dust continuum. Here we have rotated the image by 61° in order to align the elongation with the horizontal axis. The size of the beam is indicated in the lower left corner. The integrated flux in this area is 0.4 Jy. $1''$ corresponds to 3000 AU.

Table 3.3: Outflow properties derived from CO observations. Total outflow mass M_t , momentum p , energy E , size, outflow dynamical age t , outflow rate \dot{M}_{out} , mechanical force F_m and mechanical luminosity L_m are given. Inputs are discussed in the text.

M_t	p	E	size	t	\dot{M}_{out}	F_m	L_m
[M_{\odot}]	[M_{\odot} km/s]	[erg]	[pc]	[yr]	[M_{\odot} /yr]	[M_{\odot} km/s/yr]	[L_{\odot}]
12	190	3.1×10^{46}	0.42	32000	3.8×10^{-4}	6.0×10^{-3}	8.0

3.3 Observational Results

3.3.1 Millimeter Continuum Emission

Combining the very extended and compact configuration interferometer data, we map the 1.3 mm dust continuum at a spatial resolution of ~ 2500 AU (Fig. 3.2). Aside from the primary peak, we detect a secondary source $16''$ to the southwest of the primary. Zooming into the primary peak (Fig. 3.3) displays the elongation of the dust continuum in greater detail. This elongation is perpendicular to the bipolar molecular outflow shown in Fig. 3.4, and may be associated with a disk component in a roughly edge-on orientation. To simplify the analysis of the modeling, we have rotated the zoomed in image by 61° such that the elongation lies along the horizontal axis. The brightness profile along this axis is asymmetric, with the difference in height of the two peaks on the order of 1σ (see Fig. 3.6).

We measure an integrated flux of 0.4 Jy in the region contained within the 10,000 AU x 10,000 AU box shown in Fig. 3.3 and a peak flux of 0.042 Jy. Following the methods of Hildebrand (1983) and Beuther et al. (2002b, 2005a) we adopt a dust opacity index β_{op} of 2.35 (Weingartner & Draine 2001) which corresponds to the dust model used in our modeling described in Section 3.4. Assuming a dust temperature of 30 K, and an optically thin system, our measured flux at 1.3 mm corresponds to a mass of $220 M_{\odot}$ and a beam averaged column density of $1.1 \times 10^{25} \text{ cm}^{-2}$. The mass and column density would of course be lower if we use different values for β_{op} , but to maintain consistency in the comparison with T Tauri stars, we use β_{op} of 2.35 for the modeling. Using the Interstellar Medium value for β_{op} of 2.0 (Hildebrand 1983), the mass and column density then would be $120 M_{\odot}$ and $6.4 \times 10^{24} \text{ cm}^{-2}$. With a value for β_{op} of 1.4 (Ossenkopf & Henning 1994), the mass and column density become $45 M_{\odot}$ and $2.4 \times 10^{24} \text{ cm}^{-2}$. These masses are, of course, affected by missing flux in the interferometer data. Comparing our interferometric 1.3 mm flux to the single dish continuum flux at this wavelength obtained by Beuther et al. (2002a), we estimate that 75% of the more extended envelope structure contributing to the single dish flux is filtered out.

3.3.2 Line Data

Toward the continuum peak, there are only four spectral lines present in the 4 GHz bandwidth of the SMA data (see Fig. 3.1). Based solely on chemical evolution, it is difficult to determine

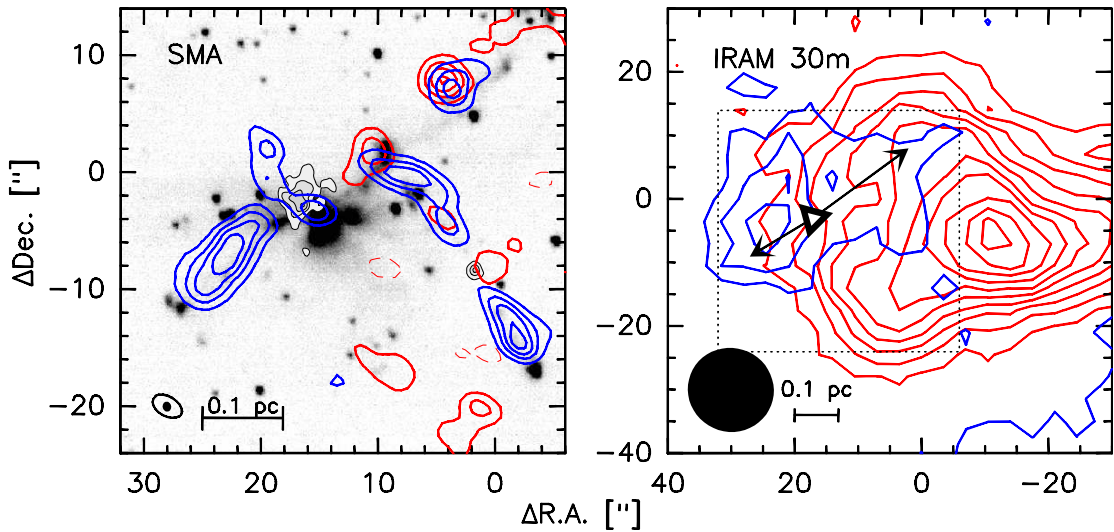


Figure 3.4: The outflow in $^{12}\text{CO}(2-1)$. Integrated maps of IRAS 18151-1208 over the entire velocity range of the line. Blueshifted emission (thick blue contours) integrated over velocities of $23-29 \text{ km s}^{-1}$ and redshifted emission (thick red contours) integrated over velocities of $40-50 \text{ km s}^{-1}$. *Left*: SMA $^{12}\text{CO}(2-1)$ and continuum (grayscale with thin solid contours) overlaid on the H_2 map of Davis et al. (2004). Contours for CO start at $\pm 3\sigma$ and increase in steps of 3σ where σ is 0.15 and $0.16 \text{ Jy bm}^{-1}\cdot\text{kms}^{-1}$ for the blue- and redshifted emission respectively. *Right*: IRAM 30 m $^{12}\text{CO}(2-1)$. The 1.3 mm dust continuum peak is indicated by the triangle, and the outflow direction and extent as determined by the SMA data are indicated by arrows. The region plotted in the SMA figure at left is indicated by the dotted lines. Contours start at 3σ and increase in steps of 3σ where σ is $11.4 \text{ Jy bm}^{-1}\cdot\text{kms}^{-1}$ for the blueshifted component and $10.4 \text{ Jy bm}^{-1}\cdot\text{kms}^{-1}$ for the redshifted component.

whether this source has not yet reached the hot core phase, or whether it has already passed through this evolutionary phase. Three of the four lines present toward the continuum peak, $^{12}\text{CO}(2-1)$, $^{13}\text{CO}(2-1)$, and $\text{SO}(6-5)$, are not high density tracers, and $\text{C}^{18}\text{O}(2-1)$ appears to be affected by outflow (see Section 3.6.3). Hence, with the data at hand we are unable to infer the kinematics of the elongated structure detected in the continuum and discussed below. Methanol, a molecule linked to rotation in Chapter 2, is present a few (~ 7) arcseconds to the northeast of the primary peak but is extremely weak directly at the location of the primary source.

Previous single dish observations by Beuther et al. (2002b) were taken during non-ideal weather conditions, so the quality of our current data set is significantly improved. Nevertheless, the $^{12}\text{CO}(2-1)$ emission is consistent with the outflow suggested by this older data set. The SMA data in Fig. 3.4 demonstrate that our observations follow the morphology of the H_2 jets seen by Davis et al. (2004). In both sets of observations, the two outflows observed are highly collimated. The two outflows we detect are roughly perpendicular to one another and appear to emanate from two separate sources detected in our 1.3 mm dust continuum. The presence of outflows is dependent on a driving source, which, in the case of low mass stars, is an accretion disk.

Several instances of anomalous behavior are apparent in Fig. 3.4. First, in the southeast-northwest outflow associated with the primary continuum source, there is a blueshifted component on the northwest side which is otherwise associated with redshifted emission (approx-

Table 3.4: Sources of SED data points.

λ (μm)	flux (Jy)	+/- (Jy)	reference
12.8	26.3	2	ESO prop. 075.C-0454, PI Fuller; H. Linz, <i>priv.comm.</i>
18.7	41.0	2	ESO prop. 075.C-0454, PI Fuller; H. Linz, <i>priv.comm.</i>
24.8	101	30	Campbell et al. (2008)
450	12.4	3.7	Marseille et al. (2008)
800	1.9	0.6	Marseille et al. (2008)
1300	0.4	0.1	these data

mately located at $\Delta\text{R.A.}=4$, $\Delta\text{Dec}=7$). This might be an indication that the outflow has a small inclination angle relative to the plane of the sky such that we observe both receding and approaching sections of the outflow. Next, it is interesting to note that both sides of the outflow associated with the secondary continuum source are dominated by blueshifted emission. This region is dominated by redshifted emission in the single dish data (Fig. 3.4) indicating that it is large scale emission and is filtered out in the interferometric data.

As discussed in Section 3.2.2, we do not combine the single dish data with the interferometric data. Instead, we use the interferometer data to accurately determine the outflow morphology as described above, but rely on the single dish data to measure fluxes. We use the single dish fluxes to calculate the outflow mass, dynamical age and outflow energetics following the approach of Cabrit & Bertout (1990). Using an average spatial extent of $30''$ for each ^{12}CO outflow lobe, and maximum blueshifted and redshifted velocities of 10 and 17 km s^{-1} respectively, we derive the properties listed in Table 3.3. Our derived values match those of Beuther et al. (2002b) reasonably well, and are likely better estimates due to poor weather conditions at the time of the earlier observations.

3.3.3 Spectral Energy Distribution

For the purpose of modeling, we gathered data for the spectral energy distribution (SED) of IRAS 18151-1208. The wavelengths and associated fluxes that we include in our SED are tabulated in Table 3.4. The 1.3 mm data point for the SED is determined by measuring the interferometric flux of IRAS 18151-1208 within the central $10,000 \text{ AU}$ by $10,000 \text{ AU}$ region. We note that the flux measured with the interferometer is a factor of four smaller than the corresponding wavelength single dish flux due to the filtering out of the cold dust in the envelope. Since we do not include this cold dust envelope component in our model, we also apply this factor of four to the $450 \mu\text{m}$ and $800 \mu\text{m}$ single dish fluxes published in Marseille et al. (2008). We justify this approach by the fact that the SED approximately follows a power law in this wavelength regime.

For the SED, the $12.8 \mu\text{m}$ and $18.7 \mu\text{m}$ data points come from VIZIER data and the $24.8 \mu\text{m}$ point comes from Campbell et al. (2008). The nominal peak positions vary by $\sim 1''$ between the

millimeter and mid-infrared data. However, in the mid-infrared, a small field of view does not allow high positional accuracy so we attribute the emission to the same source. Alternatively the offset may be due to a real difference in spatial position which would lead to a lowering of the SED at these wavelengths. We note this possibility, but proceed assuming that the detections at different wavelengths are spatially coincident.

The data of Campbell et al. (2008) exhibit a silicate absorption dip at $10 \mu\text{m}$. This dip is likely caused by absorption of the envelope. Since the millimeter interferometer data filter out the envelope, we are primarily interested in the small scale disk-like structure, so we do not try to reproduce this feature.

3.4 Modeling

After the 3D radiative transfer modeling of the circumstellar environment in the low mass regime was proven successful (Wolf et al. 2003; Sauter et al. 2009), we wanted to test whether a similar method could work in the high mass regime. We hypothesized that a scaled up version of a T Tauri disk may be able to reproduce the observations of what may possibly be a disk around a massive protostellar object.

3.4.1 The Monte Carlo 3D Radiative Transfer Code

Using the self-consistent 3D Monte Carlo Radiative Transfer code, MC3D, developed by Wolf et al. (1999); Wolf (2003), we model the elongation seen in the dust continuum of IRAS 18151-1208. In our setup, MC3D calculates the density distribution in a spherical region surrounding the central star divided into 91 equally spaced angular divisions and 50 logarithmically spaced radial divisions such that the successive grid cell is $\sim 1\%$ longer than its inner neighbor. This distribution is chosen to better resolve the density gradient in the more massive region closer to the central star. Using 100 logarithmically distributed wavelengths between 0.05 and 2000 μm , MC3D computes the thermal structure of the disk, derives SEDs, and produces images at any of the 100 wavelengths. For the purpose of this work, we use all 100 wavelengths for the temperature structure and the SED, and we compute an image at 1.3 mm.

3.4.2 The Disk

We use a density profile of a parameterized rotationally symmetric disk to produce fits to the observed SED and radial brightness profile. The density distribution we use is described by the following equation:

$$\rho_{\text{disk}}(r_{\text{cyl}}) = \rho_0 \left(\frac{R_*}{r_{\text{cyl}}} \right)^\alpha \exp \left[-\frac{1}{2} \left(\frac{z}{P_h} \right)^2 \right] \quad (3.1)$$

where z is the height above or below the midplane, R_* is the radius of the central star and r_{cyl} is the radial distance from the central rotation (z -)axis. The normalization constant, ρ_0 , is

determined by the conditions placed on the total mass and volume of the system, and

$$P_h = h_{100} \left(\frac{r_{\text{cyl}}}{100 \text{AU}} \right)^\beta \quad (3.2)$$

where h_{100} is the scale height of the disk 100 AU from the central star. The shape of the modeled disk is described by the parameters α and β , the radial density parameter and the disk flaring parameter respectively. If α and β satisfy the relation $\alpha = 3(\beta - \frac{1}{2})$, then the density distribution corresponds to that of Shakura & Sunyaev (1973). The dependence of the surface density on the disk shape parameters can then be obtained by integrating Equation 3.1 with respect to z : $\Sigma(r_{\text{cyl}}) \sim r_{\text{cyl}}^p$ where $p = \beta - \alpha$.

3.4.3 The Dust Model

Under the assumption that the gas is optically thin in the wavelength regime we are working in, it is the dust that is described by the density distribution in Equation 3.1. The dust grains are assumed to be spherical, and we adopt a power law size distribution following the MRN (Mathis et al. 1977) approach where the number of dust grains of a given radius a is given by

$$n(a) \sim a^{-3.5}. \quad (3.3)$$

Dust grain sizes a vary from 5 nm to 250 nm which are typical of the interstellar medium.

We tested two different chemical compositions. The first follows the graphite and smoothed silicate mixture of Weingartner & Draine (2001) with relative abundances of 37.5% (graphite) and 62.5% (astronomical silicate). The other contains by mass 24.2% iron and iron-poor silicates, 5.6% troilite, 25.6% refractory organics, 4.4% volatile organics, and 40.3% water (Pollack et al. 1994).

3.4.4 Observational Constraints

For the SED, the fitting is constrained in a straightforward manner by the observed fluxes. We attempt to fit our SED over the entire wavelength regime for which we have data points available.

While we use the SED to guide our efforts since the effects of modifying model parameters are more noticeable there (see Appendix) than in the image, we aim to reproduce the elongated structure seen in the 1.3 mm dust continuum perpendicular to the outflow orientation. Among other interpretations of what may be taking place in the region, possible explanations include a double source and a scaled up low mass disk. Here we focus on whether a scaled up low mass disk is consistent with these observations. Although we were able to reproduce a symmetric double peaked structure prior to smoothing with the PSF by making the inner radius larger, the convolution with the observed beam size smoothed out this effect in the image brightness profile. We then shifted our focus to fitting the shape of the elongated structure's outer edges.

This is not a significant oversight because the difference in the height of the two peaks is only on the order of 1σ . It is worth mentioning that using an extremely large inner radius flattens out the peak of the radial brightness profile (see Fig. 3.8), but because we do not know the origin of this slight asymmetry, we do not include anything in the modeling to account for the specific asymmetry nor the double peak and therefore do not give it any extra weight in our determination of the best fit model.

For the model parameters, we were able to place rough constraints on the central star, the outer radius, and the mass of the system before modeling began. Sridharan et al. (2002) place the luminosity of the IRAS 18151-1208 region at $20,000 L_{\odot}$. We therefore use this as a limiting luminosity for the central star in our modeling. We use an outer radius of 5,000 AU which is the radius at which the midplane density goes to zero and corresponds approximately to the 4σ contour of the elongation in the 1.3 mm dust continuum. Making the assumption that the region is optically thin, we can obtain a starting estimate for the mass of the system following the approach described in Section 3.3.1. Our measured flux at 1.3 mm corresponds to a mass of $220 M_{\odot}$. We take this as a starting estimate, but since there are many sources of uncertainty in this calculation such as missing flux and unknown optical depth to name a few, we did not strictly limit the mass in our tests to this value. For the test cases with a gas mass of $220 M_{\odot}$, slight differences on the order of a few percent between the observed flux and the calculated flux at 1.3 mm sometimes come about. We attribute this to the fact that despite using the same dust model, MC3D takes optical depth into consideration while the mass estimate does not.

3.4.5 The Parameter Space

A motivating question behind this study is whether a low mass disk can be scaled up to describe a high mass disk. This would manifest itself in the form of having similar parameters describing the shape of the disk and scaled up parameters for the quantities such as disk mass and extent, accompanied by a more massive central star. In the scenario that scaling-up reasonably describes the observations of the high mass protostellar object in question, we would expect the values for α and β to remain the same as in the low mass case. Although the value for h_{100} between the two cases is not directly comparable because 100 AU represents very different regions of the respective disks, we can scale h_{100} to a proportionally similar fraction of the disk's size and expect that to be proportionally larger than in the low mass case. In the ideal case, the disk mass should scale relative to the volume of the system which we can vary via the outer radius.

The parameters that we include in the modeling are:

- α , β , and h_{100} : the density distribution exponent, the disk flaring exponent, and the scale height of the disk at 100 AU respectively. These quantities describe the dust density distribution via Equations 3.1 and 3.2. We vary α between 1 and 4 and β between 0.5 and 3. The relation $\alpha = 3(\beta - \frac{1}{2})$ is shown to hold in the case of low mass disks (Wolf et al. 2003; Sauter et al. 2009), but we do not strictly follow this relation here. Under our

hypothesis that a scaled up version of a T Tauri disk may be able to describe a massive disk, we would like to see whether this relation between α and β holds. As we do not know the detailed physics of the region, we do not want to force this relation for the pure sake of the hypothesis. We test values of h_{100} between 1 and 30 AU.

- θ : the inclination of the disk with respect to the plane of the sky. The observations indicate the presence of a flattened object, and this would only be visible at inclination angles close to edge-on. However, we test inclination angles ranging from 45° to 90° (edge-on).
- R_{in} : the inner radius. We initially chose small values for R_{in} of 10, 20, and 50 AU, but also tried significantly larger values such as 400, 1000, 2500, and 4000 AU before settling on 20 AU in our best fit model.
- R_{out} : the radius at which the density goes to zero. The outer radius can roughly be constrained by the 1.3 mm continuum observations to a nominal value of 5,000 AU, so we assume this value throughout.
- M_{disk} : the dust mass. Using the dust model of Weingartner & Draine (2001) we determine a rough estimate for the mass within the 5,000 AU radius to be $220 M_\odot$ (See details in Section 3.3.1). From this, we derive a dust mass of $2.2 M_\odot$ based on a gas-to-dust ratio of 100. Taking this as our starting estimate, we subsequently determine the mass by ensuring that the SED fit goes through the 1.3 mm data point.
- Central star: due to the luminosity constraint of $20,000 L_\odot$ described above, the most massive star we consider is a B0.5 [T=26300 K, L=20000 L_\odot , R=7.0 R_\odot , M=15 M_\odot]. We also test a B1 [T=25400 K, L=16000 L_\odot , R=6.4 R_\odot , M=13 M_\odot] and a B2 [T=22500 K, L=6000 L_\odot , R=5.6 R_\odot , M=10 M_\odot] central star.

3.5 Comparing the Model with Observations

We determine the best fit model based on considering both the SED and the radial brightness profile. For each test we calculate a reduced chi-squared value as described in the last paragraph of the next section (Section 3.6.1). The parameters of the best fit model are summarized in Table 3.5 and for comparison, the best fit model of the Butterfly Star (Wolf et al. 2003, 2008) and CB 26 (Sauter et al. 2009) are also included in this table. The corresponding SED and brightness profile of the best fit model are shown in Figs. 3.5 and 3.6.

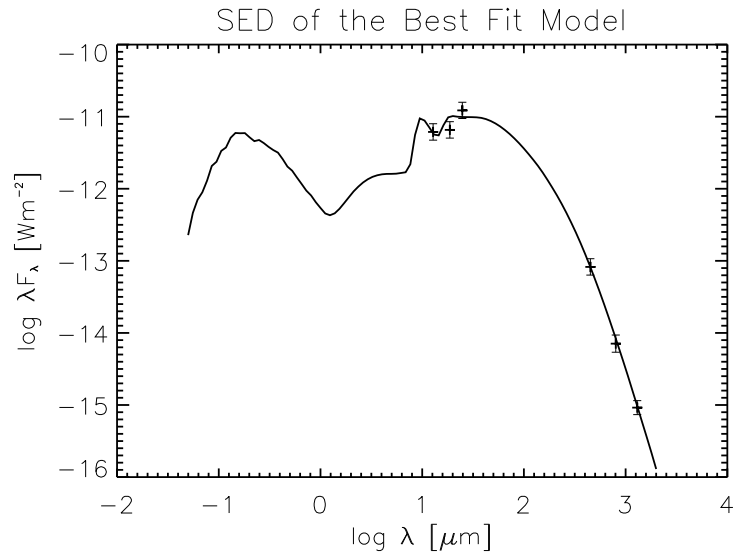


Figure 3.5: The SED of the best fit model. In this figure we include shorter wavelengths than in the modeling to show the contribution from the central star.

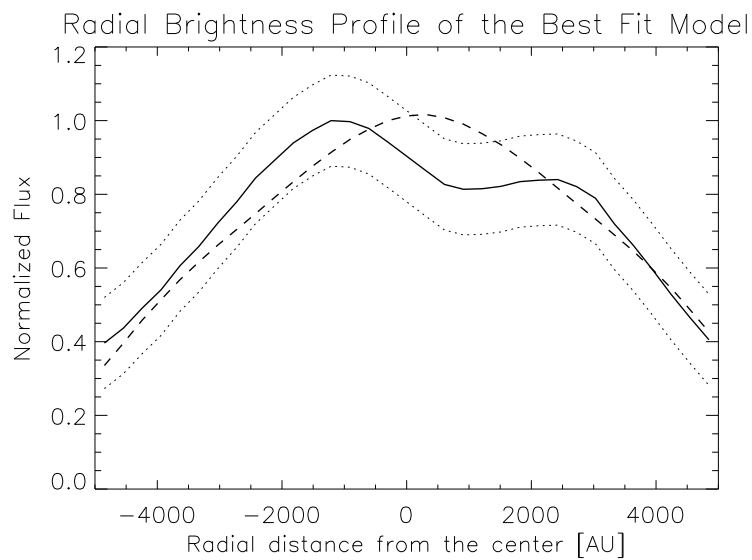


Figure 3.6: The radial density profile of the best fit model. The solid line is the cut through the midplane of the observed elongated structure. The dotted lines are $\pm 1\sigma$, and the dashed line is the model.

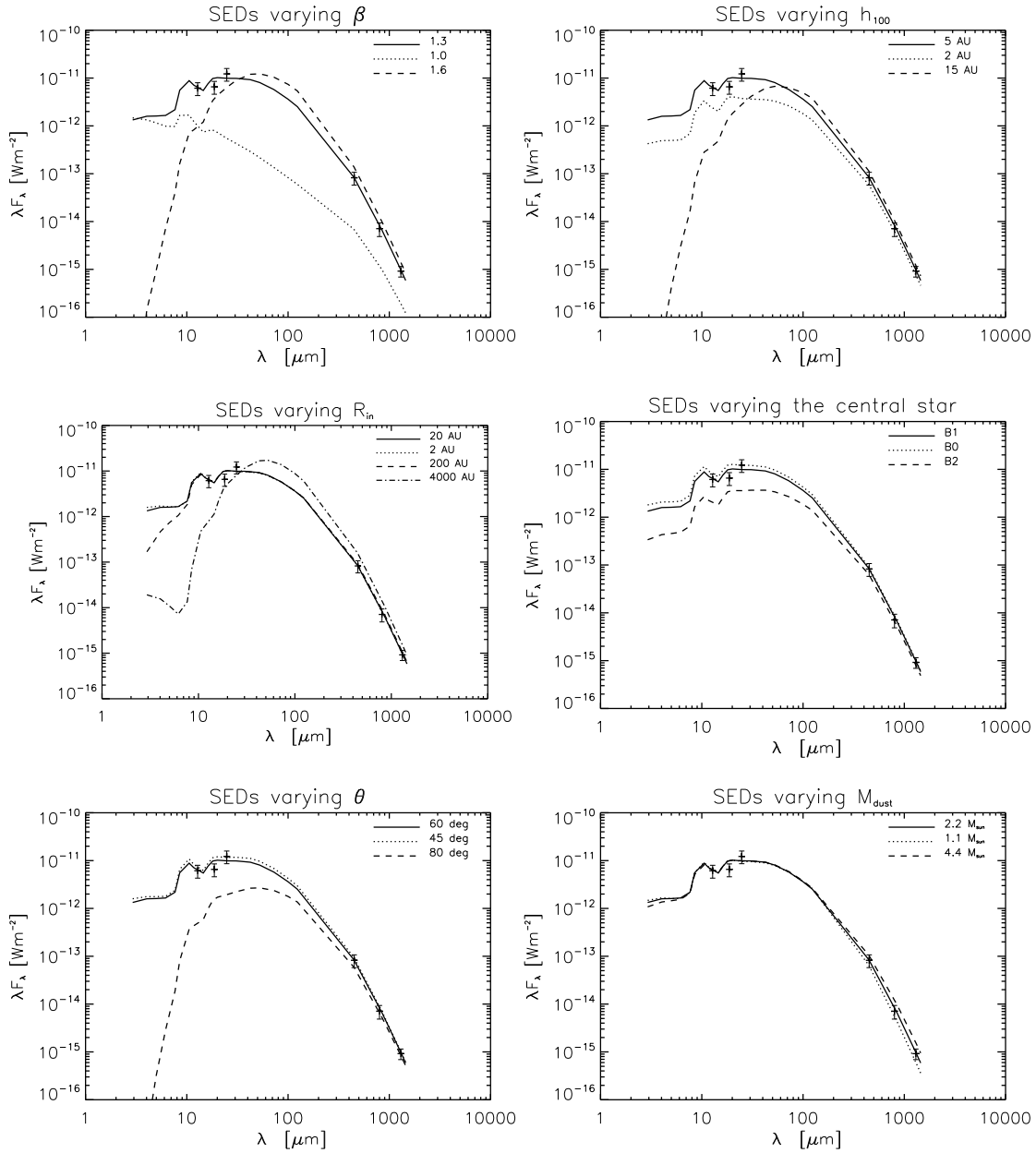


Figure 3.7: The effect on the SED of varying individual parameters. Although numerous combinations of parameters were tested (see Section 3.4.5 for a description of the parameter space), these demonstrate how individual parameters affect the SED. The solid line is always the best fit model (see Fig. 3.5). SEDs varying (from left to right, top to bottom) the flaring exponent (β), the scale height at 100 AU (h_{100}), the inner radius (R_{in}), the central star's spectral type, the inclination angle (θ), and the dust mass (M_{disk}).

Table 3.5: The parameters used in the best fit model.

Object	α	β	h_0 (AU)	M_{disk} (M_{\odot})	θ ($^{\circ}$)	R_{in} (AU)	R_{out} (AU)	R_* (R_{\odot})	T_* (T_{\odot})	L_* (L_{\odot})
IRAS 18151	2.4	1.3	200	2.2	60	20	5000	6.4	25400	16000
IRAS 04302	2.37	1.29	15	0.0007	90	0.07	300	2	4000	0.92
CB 26	2.2	1.4	6	0.003	85	45	200	2	4000	0.92

Parameters include the radial density distribution parameter α , flaring parameter β , scale height of the disk at $\frac{1}{3}R_{\text{out}}$ h_0 , dust mass M_{disk} , inclination angle θ ($\theta=90^{\circ}$ corresponds to an edge-on disk), the inner and outer radii of the density distribution R_{in} and R_{out} and the radius, temperature, and luminosity of the central star.

3.6 Discussion

3.6.1 Testing the Parameter Space

As described in Section 3.4.5, a wide range of model parameters were tested before settling on the ones used in the best fit model. Figures 3.7 and 3.8 contain overlaid SEDs and radial brightness profiles that demonstrate the effects of varying the model parameters. The effects on the SEDs are conspicuous, but the differences in the brightness profiles are more subtle. We therefore quantify each fit by determining a reduced chi-squared value for all tests performed.

Varying the dust composition as described in Section 3.4.3 did not significantly affect our results, so we present here only the results of the Weingartner & Draine (2001) composition to maintain a more direct comparison with the Butterfly Star and CB 26.

- The disk shape parameters β (flaring parameter), and h_{100} (scale height at 100 AU) primarily affect the shorter wavelengths in the SED. As demonstrated in Fig. 3.7, both lower and higher values of β and of h_{100} than used in the best fit model significantly decrease the flux in the shorter wavelength (micron) regime of the SED.
- The density distribution exponent α cannot be constrained by the data themselves. Higher resolution data would be necessary to provide stronger constraints on α . After constraining β , we use the direct relation for Shakura & Sunyaev (1973) disks between α and β [$\alpha = 3(\beta - \frac{1}{2})$] to determine a value of 2.4 for α . This approach satisfactorily reproduces our observations.
- Inclination angle: the difference in the SEDs is small for inclination angles between 45° and 60° , but we use 60° in our best fit model based on the observational data that indicate a more edge-on orientation. The SED deviates further from the observations at inclination angles larger than 60° .
- Disk mass: in the mass regime we tested, the only parameter that significantly affects the millimeter wavelength side of the SED without affecting the micron side is the dust mass. Figure 3.7 makes it apparent that using the dust model of Weingartner & Draine (2001),

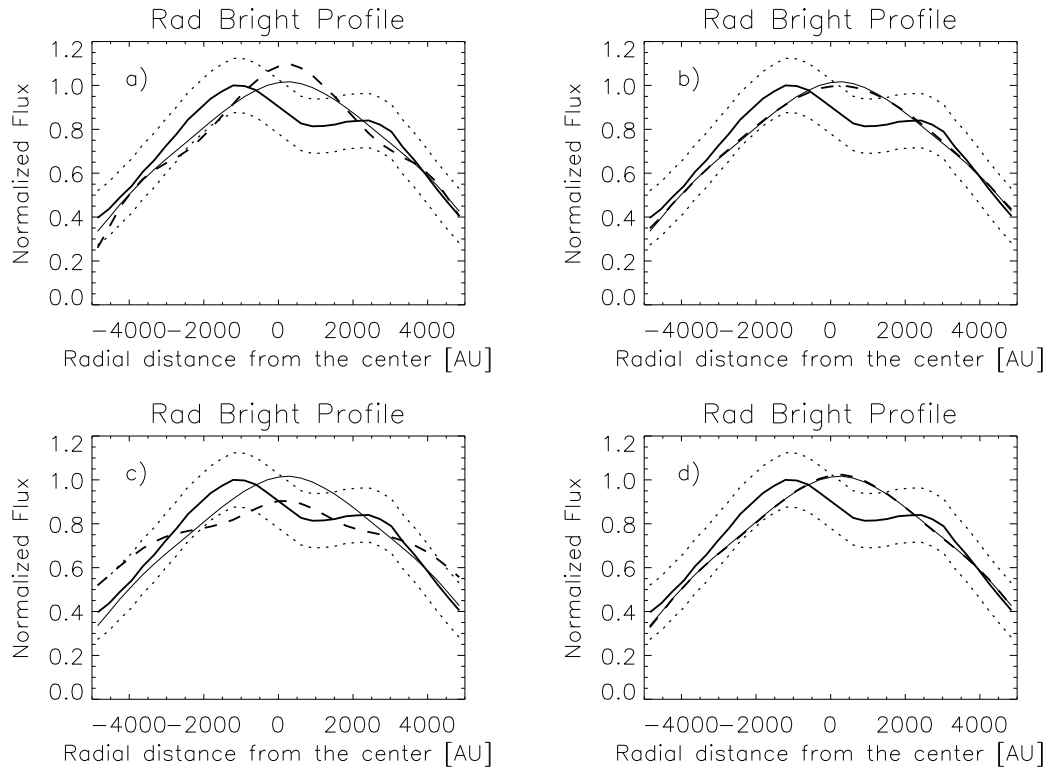


Figure 3.8: The effect on the radial brightness profiles of varying individual parameters. In each panel, the thick solid line is the cut through the midplane of the observed elongated structure, the dotted lines are $\pm 1\sigma$, the dashed line is the model and the thin solid line is an overlay of the best fit model (see Fig. 3.6). Here we have included only a select sample of the most deviant cases. The brightness profile was not affected as heavily as the SED and many of the cases show very minor deviations from the best fit model, so we do not include them here. In choosing the best fit model, we took both the SED and the brightness profile into account. See Section 3.5 for details. The parameters are similar to those of the best fit model except in panel (a): the disk flaring parameter $\beta=1.0$ instead of 1.3. (b): the inclination angle $\theta=80^\circ$ instead of 60° (c): the outer radius $R_{\text{out}}=2500$ AU instead of 20 AU and the dust mass $M_{\text{dust}}=1.2$ instead of 2.2. (d): the dust mass $M_{\text{dust}}=1.2$ instead of 2.2.

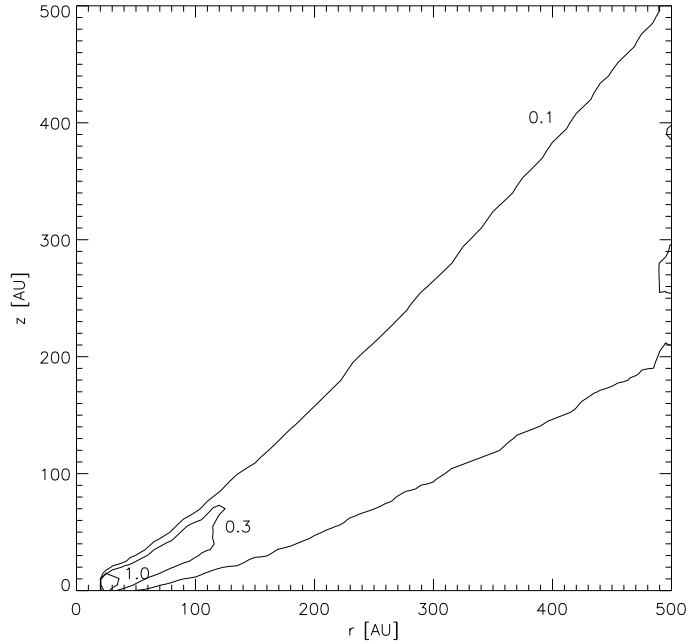


Figure 3.9: Contour plot of the Toomre Q stability parameter. The value of Q is labeled next to the respective contour. Values of Q greater than 1.0 indicate stability under the Toomre criterion.

a dust mass of $2.2 M_{\odot}$ is necessary to fit the observed 1.3 mm flux. With a gas-to-dust ratio of

$$\frac{M_{\text{Gas}}}{M_{\text{Dust}}} \sim 100, \quad (3.4)$$

this corresponds to a total disk mass of $220 M_{\odot}$. This is much larger than the main sequence mass of a B1 central star ($13 M_{\odot}$) indicating that this system cannot be Keplerian and should be quite unstable. To quantify this statement, we calculate the stability in the system under the assumption that it is a disk. Following Toomre (1964), the condition for stability is

$$Q(r, z) = \frac{c_s(r, z)\kappa(r)}{\pi G \Sigma(r)} > 1 \quad (3.5)$$

where c_s is the local sound speed, κ the angular frequency of the disk derived from Kepler's Law, G the gravitational constant and Σ the surface density. Figure 3.9 indicates that regions only within the central-most 40 AU of the system are stable under the Toomre criterion. These results are consistent with what Kratter & Matzner (2006); Vaidya et al. (2009) find in their modeling. As expected for a star-disk system that has a significant fraction of the mass in the disk, the modeled disk in this situation is unstable and is likely fragmenting and possibly forming a multiple system as described by Krumholz et al. (2009).

- Central star: since we do not have observational data for the wavelength regime dominated by the central star, we do not include these wavelengths in our SED modeling since

the main contribution to the flux at the wavelengths for which we have data is from the warm dust in the disk. Nevertheless, increasing the temperature and luminosity of the central star raises the SED in the dust dominated wavelength regime and shifts the peak to shorter wavelengths as one would expect for warmer objects.

- Inner radius: we do not expect our symmetric model to reproduce the asymmetric peak structure of the observed radial brightness profile but even having a large inner hole (large R_{in}) does not produce a double peak structure as one might expect. At extreme values of R_{in} such as 2500 or 4000 AU, the brightness profile does appear double peaked, but after convolution with the observed beam, the double peak that comes out of the modeling is smoothed out. Increasing the inner radius to these extreme values flattens out the brightness profile toward the center (see Fig. 3.8) but also makes the brightness profile wider which significantly worsens the fit at the edges.

To quantify the quality of the fit for each set of parameters tested, we do a weighted linear least squares fit to the six data points in the SED as well as six points distributed along the sides of the radial brightness profile. We avoid the central section of the brightness profile because our symmetric model cannot account for the asymmetric structure observed. We choose six points in the brightness profile to give equal weight to the SED and image fitting. While this test helps significantly in narrowing down the best values for most parameters, it does not do a good job discriminating between values of α . We have not done a complete parameter space study for the parameters listed above, so this least squares fit represents the best fit of the chosen parameter combinations. However, we have attempted to do this in a manner such that the progression of model parameters tested becomes more and more constraining. Namely, starting with a coarse grid within the parameter space described in Section 3.4.5, groups of parameter sets were tested. Depending on the SED and radial brightness profile fits, the next set of tests were designed to narrow down the parameter space and use a finer grid.

3.6.2 Comparison with T Tauri Stars

Comparing IRAS 18151-1208 with CB 26 (Sauter et al. 2009) and the Butterfly Star (IRAS 04302+2247, Wolf et al. 2003, 2008), we notice that similar parameters describing the distribution of the dust adequately reproduce the observed elongation in IRAS 18151-1208. We did not choose these values right from the beginning, but only through quantifying the fits by means of calculating a weighted least squares value did we determine these parameters to be nearly identical. In the case of the density distribution exponent α , the best fit value is not tightly constrained by the least squares fitting. We therefore calculate a value of 2.4 for α using the value of the more constrained parameter β in the Shakura & Sunyaev (1973) relation between α and β .

On absolute scales, the values of the disk scale height at 100 AU do not coincide (5 AU for IRAS 18151-1208 versus 10 AU for CB 26 and 15 AU for the Butterfly Star). However, this

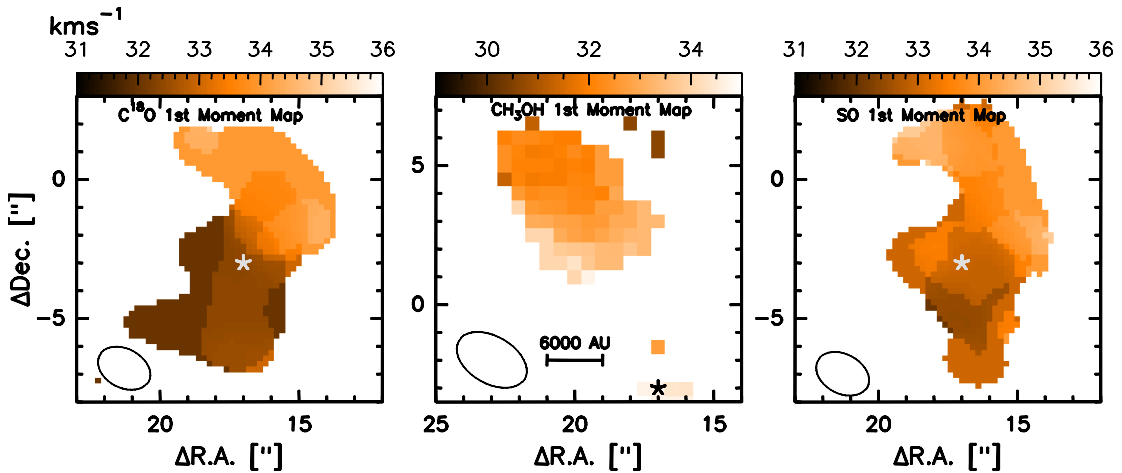


Figure 3.10: C^{18}O , CH_3OH , and SO velocity moment maps clipped at the 8σ , 4σ , and 6σ levels respectively of the corresponding line's intensity map. For C^{18}O , $\sigma=0.075$ Jy, for CH_3OH , $\sigma=0.054$, and for SO , $\sigma=0.062$. In each panel, the star symbol indicates the position of the dust continuum peak, and the circle at bottom left represents the size of the SMA beam. Although the size of each map is identical, note that the spatial position is offset in the middle panel compared to the other panels.

discrepancy can be explained by the fact that in the T Tauri stars, 100 AU is proportionately much further out in the disk (e.g. $\frac{1}{3}R_{\text{out}}$ for the Butterfly Star) compared to the high mass protostellar object in which 100 AU corresponds to only one fiftieth of the outer radius ($\frac{1}{50}R_{\text{out}}$). As defined, these values cannot directly be compared. As a better comparison, we calculate the height of the massive disk at $\frac{1}{3}R_{\text{out}}$. This turns out to be 200 AU, or 4% of the outer radius. In the CB 26 and Butterfly Star cases, the height of the disk one third of the way out is 3% and 5% of the outer radius respectively. Within the uncertainties, these numbers are quite comparable and support our assumption that a geometrically thin disk is an appropriate model in the high mass regime.

The parameters describing the dust mass and the central star differ significantly for the two types of young stars as expected. The mass of the modeled IRAS 18151-1208 system is on the order of 1000 times greater than in the T Tauri cases. Another large difference is in the outer radius. In the scenario that massive star formation proceeds as a scaled up version of low mass star formation, it is expected that disks around massive stars should be significantly larger than the disks of their low mass counterparts. The observations in this case study are consistent with this picture, but definitive observational evidence of large disks around massive stars is lacking (See the review by Cesaroni et al. 2007). The elongated structure that we observe in IRAS 18151-1208 is more than ten times larger than the several hundred AU extent of disks around T Tauri stars and is consistent with a scaling factor of ~ 15 compared to the Butterfly Star for the overall system.

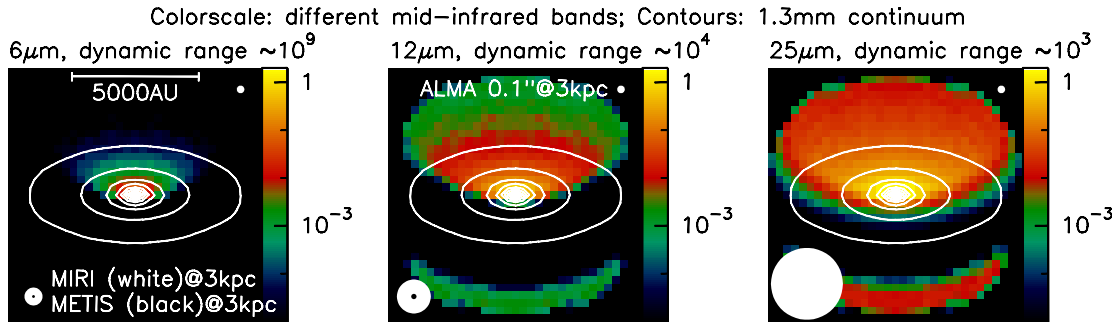


Figure 3.11: Predictions at mid-infrared and millimeter wavelengths of what may be observable with future observatories. For the sake of example, resolution elements for several planned instruments (MIRI on JWST, METIS on the E-ELT, and ALMA) are shown in the panels that correspond to wavelengths observable with those instruments. The flux scale is identical in all three panels.

3.6.3 Rotation and Infall

The scarcity of molecular lines in the observed spectrum has made it a difficult task to assess the region for indications of rotation or infall. A velocity gradient in C^{18}O is mildly present (see Fig. 3.10), but is neither aligned with the elongation in the expected disk orientation nor with the outflow direction. This gradient has a velocity range of $\sim 4 \text{ km s}^{-1}$ and extends across a region approximately 25,000 AU long. The SO emission follows a similar trend as C^{18}O , but the trend is even weaker. These molecules are likely affected by both the outflow and the disk component.

There is no significant methanol detection at the position of the dust continuum peak, and the emission detected to the northeast does not exhibit any indication of rotation. As there are no further lines in our 4 GHz bandwidth spectrum from the SMA, we are limited on this front. Perhaps further observations at other wavelengths would yield a tracer of the kinematics in the region.

3.6.4 Predictions for Future Observatories

The MC3D code is capable of computing images at a wide range of wavelengths which can be used to speculate what a disk might look like with future observatories. In Fig. 3.11 we include predictions at 6, 12, and 25 micron as well as contour overlays of the 1.3 mm model. In this figure, we also include the beam sizes of observatories on the horizon, namely the Atacama Large Millimeter Array (ALMA), and the MIRI and METIS instruments planned for the James Webb Space Telescope (JWST) and the European Extremely Large Telescope (E-ELT). The flux is plotted on the same scale in each panel for the purpose of comparison. It should be noted that despite increases in sensitivity over today's instruments, the dynamic range of these future observatories will still be insufficient for the dynamic range of the 6 μm image.

3.7 Conclusions

Observations of the high mass protostellar object IRAS 18151-1208 reveal an elongation in the 1.3 mm dust continuum. These observations also confirm a well-defined orientation for a collimated outflow emanating from that dust continuum peak. This elongated structure is perpendicular to the outflow orientation, and has an approximate diameter of 10,000 AU. While kinematic evidence of rotation is not available, the spatial signature of the dust continuum is indicative of a circumstellar disk.

Under the hypothesis that massive star formation is a scaled up version of low mass star formation, we adapted the 3D radiative transfer Monte Carlo code MC3D to reproduce the observations. This was achieved by fitting the SED as well as the radial brightness profile of the 1.3 mm dust continuum image. The best fit model is of a flared disk containing $220 M_{\odot}$ of gas and dust with an inclination of 60° . While this is not the only possible scenario to explain the observations, we conclude that this scaled up approach is viable.

Compared to disks around T Tauri stars for which MC3D has successfully been applied, our best fit model has similar parameters describing the shape of the disk (density distribution and flaring amount) while larger values are necessary for the absolute parameters of the system such as mass, extent, and the central star. The disk produced by the modeling is unstable aside from a small region close to the central star. This is an expected outcome since the mass of the disk is dominant in the disk-star system.

A further outcome of the modeling is that we can produce images at multiple wavelengths which can be helpful for visualizing what future observatories such as ALMA, JWST, and the ELTs will be capable of observing. Future work possible before these observatories become available includes looking for other tracers of the kinematics in the region. Pending the discovery of a molecule that traces rotation in the region, this source will be unique in that both the spatial density and flaring structure as well as the kinematic properties of the region will be known.

Chapter 4

The Hot Core Source: IRAS 18507+0121

4.1 Introduction

The initial stages of massive star formation take place in a dense region within a molecular cloud, namely, in an Infrared Dark Cloud (IRDC). The dense, cold cores within these IRDCs then evolve from a cold dense starless core into the Hot Molecular Core (HMC) phase. These HMCs are dense, massive and are characterized by chemical richness (Kurtz et al. 2000).

One example of an HMC source is IRAS 18507+0121. IRAS 18507+0121 is located within the infrared dark cloud seen in Fig. 4.1 and its position is marked in this figure as MM1. For this source, we will adopt a distance of 3.9 kpc and a rest velocity of 57.1 km s^{-1} . These values are consistent with what other authors have used (e.g. Molinari et al. 1996; Zhang et al. 2005; Shepherd et al. 2007), although mild variations to these quantities can be found in the literature.

Based on SED fitting, Rathborne et al. (2005) estimate a bolometric luminosity for this source of $32,000 L_{\odot}$. Because massive protostars evolve at relatively constant luminosity (Iben 1965; Palla & Stahler 1990), this can give a rough estimate for a high mass protostars' main sequence luminosity and hence its mass. The luminosity determined for IRAS 18507+0121 corresponds to an O9.5 main sequence star.

In a study by Shepherd et al. (2007) including observations of $^{12}\text{CO}(1-0)$, the outflow orientation in the region was determined. A dominant redshifted lobe is observed to the southwest of the millimeter continuum peak and a weak blueshifted counterpart is detected to the northeast. Some evidence for a weak outflow orthogonal to the primary outflow is also presented.

The discovery of an accretion disk perpendicular to the outflow orientation around a massive protostar would provide strong support for an accretion based formation scenario for massive stars. By modeling single dish spectra of several high density tracers, Ramesh et al. (1997) infer the presence of infall in the region. More recently, Rathborne et al. (2008) observe a velocity shift with the Submillimeter Array in the higher excited $J=3-2$ transition of ^{13}CO that

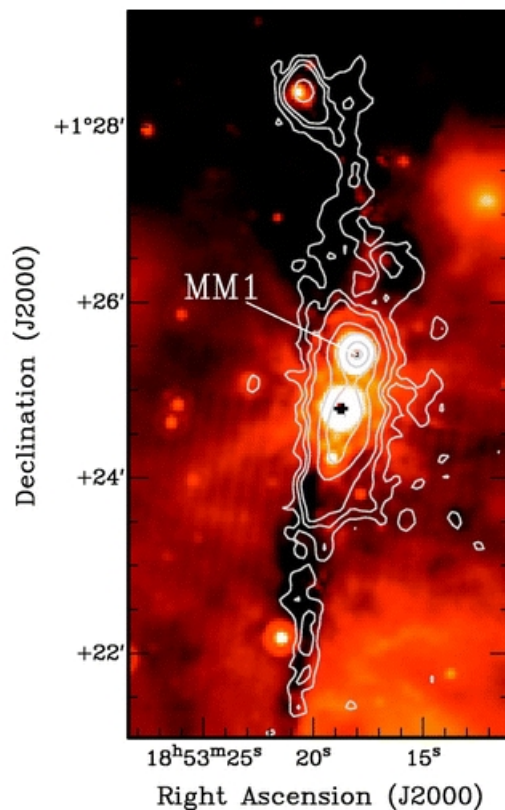


Figure 4.1: Spitzer 24 μm image with IRAM 30m 1.2 mm continuum contours. MM1 corresponds to the source in our current studies. Figure credit: Fig. 5 in Rathborne et al. (2006).

is perpendicular to the outflow, although they cannot differentiate between the possibilities that this may be the result of either an outflow or a rotating envelope.

This source was included in a sample of massive star formation regions deemed to be good candidates for harboring accretion disks (PI Q. Zhang). As a member of this sample, IRAS 18507+0121 was observed with the Submillimeter Array and the IRAM 30 m telescope. These observations made possible the study of the outflow component as well as the search for indications of accretion activity in the region. Additionally, the more evolved hot core chemistry of this source is well suited for a comparative study with the chemistry of the two sources discussed previously in this thesis.

4.2 Observations

IRAS 18507+0121 was observed with the Submillimeter Array (SMA) and IRAM 30 m telescope. Submillimeter Array observations include the 1.3 mm dust continuum as well as a multitude of molecular lines. Maps of $^{12}\text{CO}(2-1)$ and $^{13}\text{CO}(2-1)$ were made with the IRAM 30 m single dish telescope.

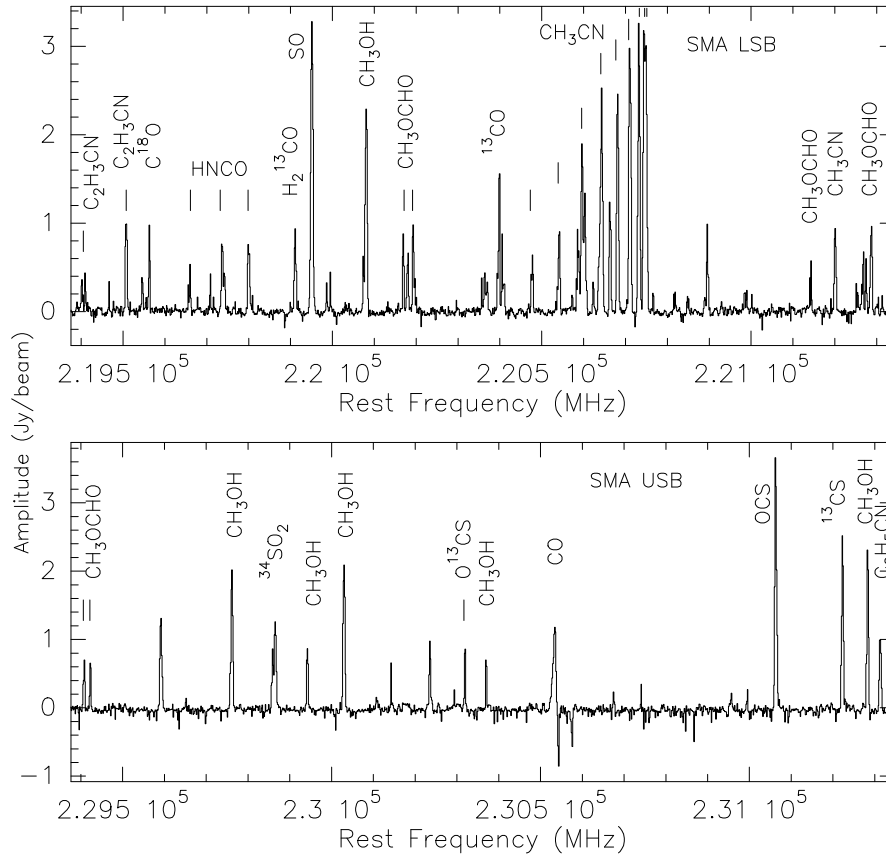


Figure 4.2: The spectra from the SMA. All identified lines are labeled. *Upper*: the lower side band spectrum at the center of the 1.3 mm dust continuum peak of the compact configuration data. *Lower*: the same as above except for the upper side band.

4.2.1 Submillimeter Array

Observations of IRAS 18507+0121 were made with the SMA in the compact configuration on 2007 August 1 and in the very extended configuration on 2008 August 3. The two spectral sidebands were tuned to the commonly used 220 and 230 GHz setup which includes the ^{12}CO , ^{13}CO , and C^{18}O $J=2-1$ transitions as well as a CH_3CN ladder and other hot core tracing molecules. Each sideband has a bandwidth of 2 GHz. The spectra from the lower and upper sidebands are shown in Fig. 4.2, and the identified lines are listed in Table 4.1.

The datasets were calibrated in a similar fashion as the SMA datasets of the previous two sources in this thesis. The compact configuration observations were made with 5 of the SMA's 8 antennas. The quasar 3c454.3 was used as the bandpass calibrator, and the quasar 1751+096 which was observed regularly during the source loop was used for phase and amplitude calibration.

Table 4.1: Observed lines

Transition	Rest Frequency [GHz]	E_{up}/k [K]	Transition	Rest Frequency [GHz]	E_{up}/k [K]
$\text{C}_2\text{H}_3\text{CN}(23_{3,20}-22_{3,19})$	219.401	146	$\text{CH}_3\text{CN}(12_{3-11_3})$	220.709	133
$\text{C}_2\text{H}_5\text{CN}(22_{2,21}-21_{1,20})$	219.464	113	$^*\text{CH}_3\text{CN}(12_{2-11_2})$	220.730	97
$^*\text{C}_2\text{H}_5\text{CN}(24_{2,22}-23_{2,21})$	219.506	136	$\text{CH}_3\text{CN}(12_{1-11_1})$	220.743	76
$^*\text{C}^{18}\text{O}(2-1)$	219.560	16	$\text{CH}_3\text{CN}(12_{0-11_0})$	220.747	69
$\text{HNCO}(10_{3,8}-9_{3,7})$	219.657	433	$\text{CH}_3\text{OCHO}(18_{13,*}-17_{13,*}) \text{ A}$	221.141	213
$\text{HNCO}(10_{3,7}-9_{3,6})$	219.657	433	$\text{CH}_3\text{CN}(12_{1-11_1}), \nu_8=1$	221.199	?
$\text{HNCO}(10_{2,9}-9_{2,8})$	219.734	228	$\text{CH}_3\text{OCHO}(18_{12,7}-17_{12,6}) \text{ E}$	221.281	196
$\text{HNCO}(10_{2,8}-9_{2,7})$	219.737	228	$\text{CH}_3\text{OCHO}(18_{3,15}-17_{3,14}) \text{ E}$	229.405	110
$^*\text{HNCO}(10_{0,10}-9_{0,9})$	219.798	58	$\text{CH}_3\text{OCHO}(18_{3,15}-17_{3,14}) \text{ A}$	229.420	110
$^*\text{H}_2^{13}\text{CO}(3_{1,2}-2_{1,1})$	219.909	33	$\text{CH}_3\text{OH}(8_{-1,8}-7_{0,7}) \text{ E}$	229.759	89
$^*\text{SO}(5_6-4_5)$	219.949	35	$^{*34}\text{SO}_2(4_{2,2}-3_{1,3})$	229.858	19
$^*\text{CH}_3\text{OH}(8_{0,8}-7_{1,6}) \text{ E}$	220.078	97	$\text{CH}_3\text{OH}(19_{5,15}-20_{4,16}) \text{ A}$	229.864	579
$^*\text{CH}_3\text{OCHO}(17_{4,13}-16_{4,12}) \text{ E}$	220.167	103	$\text{CH}_3\text{OH}(19_{5,14}-20_{4,17}) \text{ A}$	229.939	579
$\text{H}_2\text{CCO}(11_{1,11}-10_{1,10})$	220.178	76	$\text{CH}_3\text{OH}(3_{-2,2}-4_{-1,4}) \text{ E}$	230.027	40
$\text{CH}_2(\text{OH})\text{CHO}(7_{6,2}-6_{5,1})$	220.197	37	$\text{CH}_3\text{OCHO}(22_{9,13}-22_{8,14}) \text{ A}$	230.294	203
$\text{CH}_2(\text{OH})\text{CHO}(7_{6,1}-6_{5,2})$	220.197	37	$\text{O}^{13}\text{CS}(19-18)$	230.318	111
$^{13}\text{CO}(2-1)$	220.399	16	$\text{CH}_3\text{OH}(22_{4,18}-21_{5,17}) \text{ E}$	230.368	683
$\text{CH}_3\text{CN}(12_8-11_8)$	220.475	526	$\text{CO}(2-1)$	230.538	17
$^*\text{CH}_3\text{CN}(12_7-11_7)$	220.539	419	$^*\text{OCS}(19-18)$	231.061	111
$\text{HNCO}(10_{1,9}-9_{1,8})$	220.585	102	$^{*13}\text{CS}(5_0-4_0)$	231.221	33
$\text{CH}_3\text{CN}(12_6-11_6)$	220.594	326	$\text{CH}_3\text{OH}(10_{2,9}-9_{3,6}) \text{ A}$	231.281	165
$\text{CH}_3\text{CN}(12_5-11_5)$	220.641	247	$\text{C}_2\text{H}_5\text{CN}(26_{1,25}-25_{1,24})$	231.310	153
$\text{C}_2\text{H}_5\text{CN}(25_{2,24}-24_{2,23})$	220.661	143	$\text{C}_2\text{H}_5\text{CN}(27_{0,27}-26_{1,26})$	231.312	158
$\text{CH}_3\text{CN}(12_4-11_4)$	220.679	183	$\text{C}_2\text{H}_5\text{CN}(24_{2,23}-23_{1,22})$	231.313	132

The * symbol before the name of the line indicates that the velocity moment map of that line is presented in Fig. 4.5.

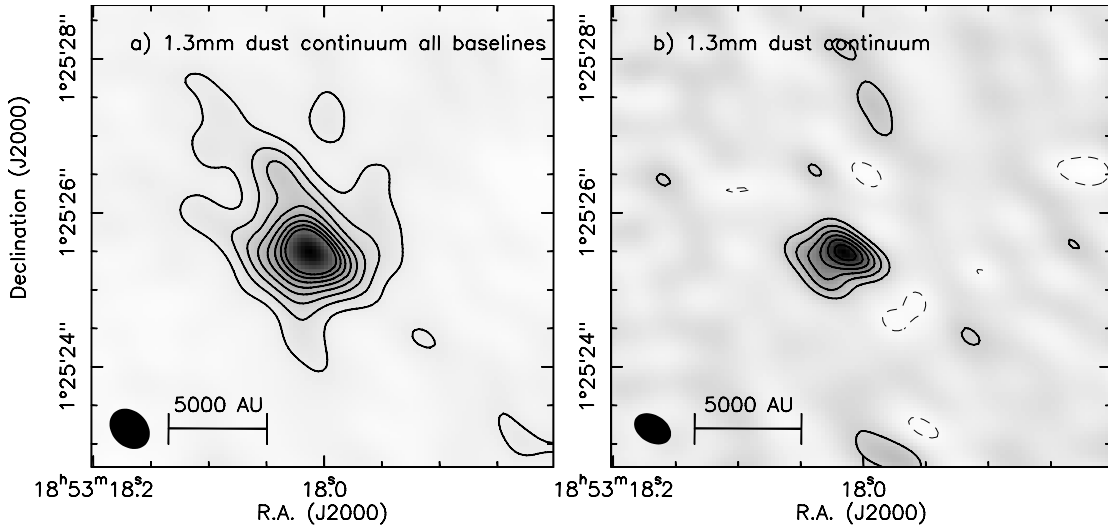


Figure 4.3: The SMA 1.3 mm dust continuum. *a*: including all baselines using a robust parameter of 2 (natural weighting). Contours start at $\pm 4\sigma$ in steps of 4σ where $\sigma=5.7 \text{ mJy bm}^{-1}$. *b*: excluding short (less than 100 k λ) baselines and using a robust parameter of -2 (uniform weighting) to emphasize the long baselines. Contours start at $\pm 3\sigma$ in steps of 3σ where $\sigma=7.5 \text{ mJy bm}^{-1}$.

For the very extended configuration data set, all 8 antennas were operational. Zenith opacity, $\tau(225 \text{ GHz})$, was ~ 0.1 . As in the compact configuration data, quasar 3c454.3 was used as the bandpass calibrator. The quasars 1751+096 and 1830+063 were used as phase and amplitude calibrators. Observations of MWC349 and Callisto were used for flux calibration. Combined with the compact configuration, visibilities range from 14 to nearly 400 k λ .

4.2.2 Pico Veleta 30 m Telescope

We have obtained ^{12}CO (2–1) and ^{13}CO (2–1) observations with the IRAM 30 m telescope near Granada, Spain. These observations were made in pooled mode in 2007. A map of each molecular line's emission was created with the nine-pixel HERA receiver. These maps are approximately $140'' \times 140''$ in extent and have a beam size of $11''$. Scans were made with $2''$ spacing in both Right Ascension and Declination. The single dish spectra were initially reduced with CLASS in the GILDAS software package, and then Right Ascension and Declination scans were combined with the plait algorithm in GREG. The ^{12}CO single dish data were converted to visibilities and combined with the SMA ^{12}CO data using UVMODEL in MIRIAD.

4.3 Results and Discussion

4.3.1 Millimeter Continuum Emission

In Fig. 4.3 we present the 1.3 mm dust continuum. Including all of the data from the compact and very extended configurations (Fig. 4.3a), we see that on relatively large scales, the outflow cavity is already apparent. The ^{12}CO data presented in the next section indicate that the outflow

is oriented northeast-southwest. This is already hinted at by the extensions detected along the edges of the outflow cavity emanating in both directions from the central source. Taking into account the direction of beam elongation, we also detect with some reservation an elongation in the continuum perpendicular to the outflow orientation.

When the short baseline data between 0 and 100 k λ (corresponding to baselines shorter than 130 m) are excluded and uniform weighting is applied (Fig. 4.3b), the beam size is reduced slightly and the large-scale emission is filtered out. After making these adjustments, the elongation of the continuum becomes more pronounced. By excluding the short baselines, the elongation along the outflow axis is due to the shape of the beam. However, in the orthogonal direction, an extension becomes prominent especially toward the southeast and may be the signature of a disk. Because this observation appears to be resolution limited, higher angular resolution data would be necessary to confirm the true nature and extent of this potential disk object.

This extension is small in physical extent. Approximately 1'' across, this corresponds to a projected length of slightly less than 4000 AU. Although we cannot confirm that this elongated structure is rotating, one possible explanation for the extension would be the presence of an accretion disk. As this is significantly smaller than the flattened elongation seen in IRAS 18151-1208 (Chapter 3), the elongation observed in this source may be an indication that the disk component becomes more compact over time. This possibility will be discussed further in Chapter 5.

Following the same procedure as described in Sections 2.3.2 and 3.3.1 for IRDC 18223-3 and IRAS 18151-1208, the gas mass and beam averaged H₂ column density can be obtained. Using the continuum image with all baselines of the combined compact and very extended configuration datasets, we measure a peak flux of 0.29 Jy bm⁻¹ and a total flux of 1.26 Jy. Assuming a temperature of 34 K and an opacity index of 1.8 as determined by Rathborne et al. (2005), the calculated gas mass is 400 M_⊙ and the beam averaged column density is 6.0×10²⁵ cm⁻². Considering that some of the flux is filtered out in these interferometric observations, this mass estimate is consistent with the single dish estimate of 800 M_⊙ derived by Rathborne et al. (2005).

4.3.2 Line Data and Outflow Properties

As seen in Fig. 4.4, observations of ¹²CO (2–1) indicate the presence of an outflow in a northeast-southwest orientation. Here, the redshifted lobe of the molecular outflow is dominant and well defined. The outflow morphology seen here matches the ¹²CO (1–0) observations presented by Shepherd et al. (2007) well. Namely, we also trace an expanding redshifted outflow lobe and only very weak blueshifted emission. However, a secondary outflow proposed by Shepherd et al. (2007) (labeled outflow ‘B’ by these authors) is not detected in our data.

As we have done in previous chapters, we can calculate characteristics of the region based on the outflow properties. Refer to Section 2.3.3 for a description of the method and assumptions

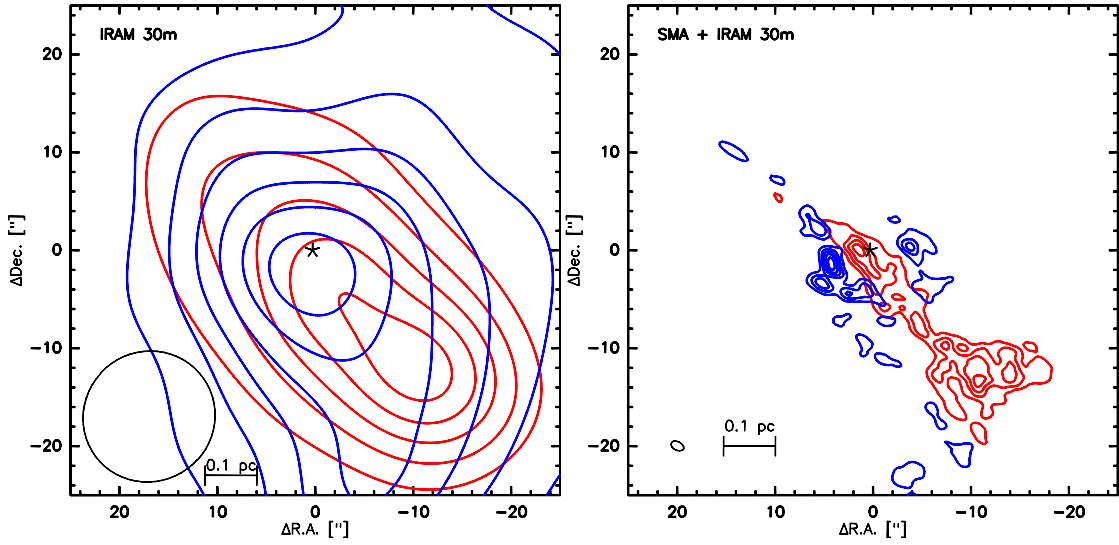


Figure 4.4: Blue- and redshifted ^{12}CO emission. Blueshifted emission (blue contours) ranges from 41-54 km s^{-1} and redshifted emission (red contours) ranges from 61-84 km s^{-1} . The SMA 1.3 mm dust continuum peak is indicated by the star symbol. Beam sizes are shown in the bottom left corner. Contours go from 15% to 90% of the integrated wing's peak flux in steps of 15%. *Left*: the IRAM 30 m data. The blue- and redshifted peak fluxes are 14.1 and 44.4 $\text{mJy bm}^{-1} \text{ km s}^{-1}$ respectively. *Right*: the SMA compact and very extended configuration data combined with the single dish data. Peak fluxes are 0.9 and 1.6 $\text{mJy bm}^{-1} \text{ km s}^{-1}$ for red and blueshifted emission respectively.

Table 4.2: Outflow parameters without inclination angle correction and corrected for an inclination of 45° with respect to the plane of the sky.

i [$^\circ$]	M_t [M_\odot]	p [$M_\odot \text{ km/s}$]	E [erg]	size [pc]	t [yr]	\dot{M}_{out} [M_\odot/yr]	F_m [$M_\odot \text{ km/s/yr}$]	L_m [L_\odot]
	43	1100	2.8×10^{47}	0.52	23000	1.8×10^{-3}	4.7×10^{-2}	100
45	43	1500	5.6×10^{47}	0.74	23000	1.8×10^{-3}	6.6×10^{-2}	200

Entries include inclination i , total outflow mass M_t , momentum p , energy E , size, outflow dynamical age t , outflow rate \dot{M}_{out} , mechanical force F_m and mechanical luminosity L_m . Inputs are discussed in the text.

made for these calculations. Using only the single dish data, we measure an average outflow extent of $27''$ from the position of the source, a maximum blueshifted velocity of 16 km s^{-1} and a maximum velocity of 27 km s^{-1} for the redshifted lobe. With these values, we calculate the outflow properties listed in Table 4.2. In order to compare our results with Shepherd et al. (2007), we correct these calculated values for an inclination angle of 45° as they have done. After doing so, we obtain a slightly higher total mass, but roughly an order of magnitude higher values for the energetic quantities such as momentum, kinetic energy, accretion rate, force, and luminosity. The timescale is correspondingly slightly shorter than the outflow dynamical age they calculate. The discrepancy between the two sets of calculations arises in the fact that the outflow traced by $^{12}\text{CO} (2-1)$ is not as extended as traced by $^{12}\text{CO} (1-0)$ and that our redshifted lobe extends to much higher velocities than the redshifted $^{12}\text{CO} (1-0)$.

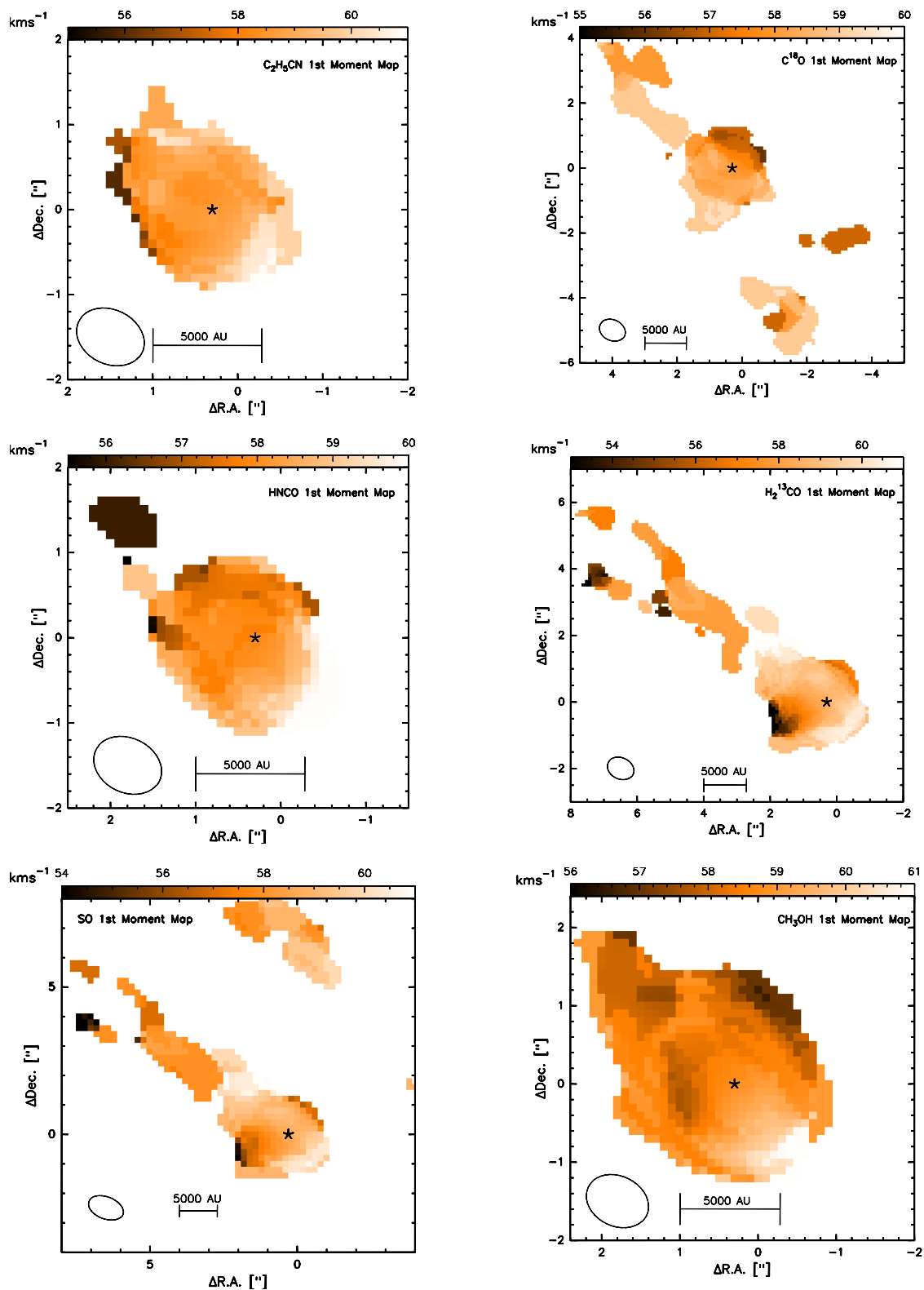


Figure 4.5: Velocity moment maps of a selection of the lines in the SMA data. For chemical species with multiple transitions within the data set, we present the moment map of the strongest transition, with the exception of the CH₃CN k=7 line which we include in addition to the k=2 line as a representative of the more highly excited lines in the CH₃CN k-ladder. The beam size is included in the lower left corner and the peak position of the 1.3 mm dust continuum is indicated by the star symbol in each panel.

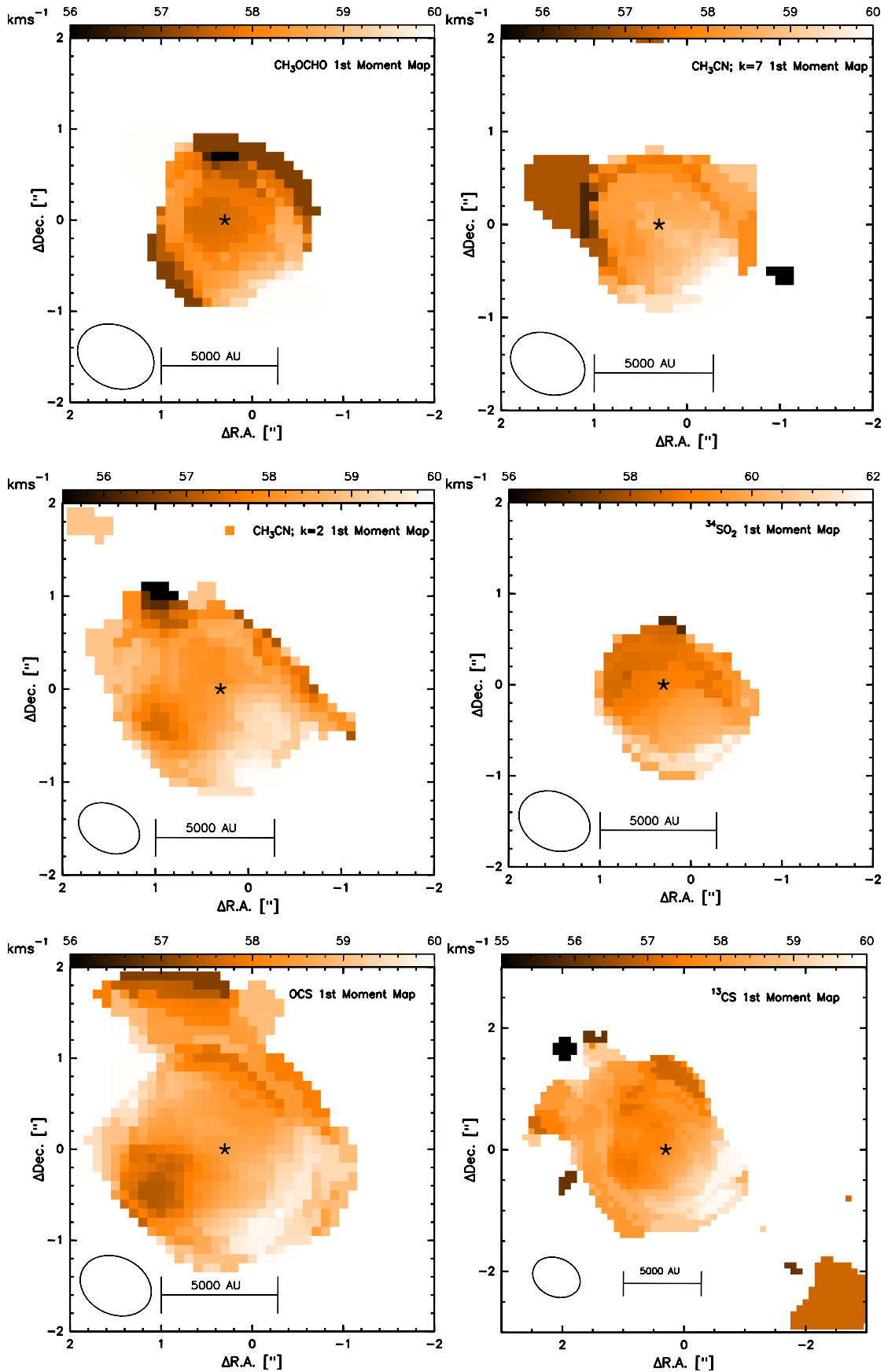


Figure 4.5: continued

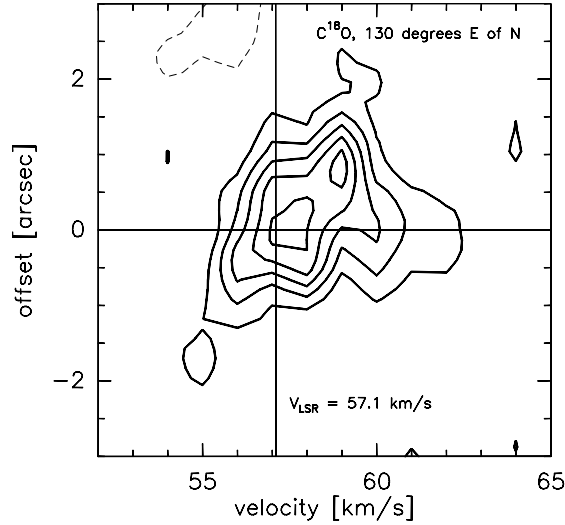


Figure 4.6: The position-velocity diagram of $C^{18}O$ along a cut perpendicular to the outflow axis. The offset on the y-axis is the distance from the dust continuum peak. Contours start at $\pm 1\sigma$ and continue in steps of 1σ where σ is $0.094 \text{ Jy } \text{bm}^{-1}$.

4.3.3 Velocity Structure

In Fig. 4.5, we present velocity moment maps of a selection of the molecular lines present in the SMA data set. The transitions presented in the moment maps are marked by a * symbol in Table 4.1. As we have seen in the previous two case studies, $C^{18}O$ exhibits behavior indicating that it is affected by the outflow. In IRAS 18507+0121, a velocity gradient is present in the central region of the $C^{18}O$ velocity moment map, although an extension to the northeast and southwest tracing the outflow is also present.

As we have discussed in the previous two chapters, velocity gradients in $C^{18}O$ may trace a rotating disk component, but it is heavily influenced by the outflow as well. In IRDC 18223-3 and IRAS 18151-1208, this was made apparent by the observation that the velocity gradients in $C^{18}O$ were neither aligned with nor perpendicular to the outflow. In the case of IRAS 18507+0121 the gradient is also not perpendicular to the outflow, and the effect of the outflow is made evident by an extension along the outflow.

We use a position-velocity diagram to further study the kinematics of the observed $C^{18}O$ velocity gradient. The position-velocity diagram through the dust continuum peak and perpendicular to the outflow orientation is shown in Fig. 4.6. In this diagram, it is evident that for redshifted velocities, the highest velocity emission is located closest to the center. This distribution is consistent with a Keplerian structure, but cannot be confirmed.

The outflow component is also traced by $H_2^{13}CO$ and SO . In the velocity moment maps of these molecules, the outflow is only detected to the northeast of the continuum peak. Although the ^{12}CO data indicate that the redshifted outflow component primarily extends to the southwest, the velocities tracing the outflow extension to the northeast in the moment maps are also redshifted. This is not inconsistent, because although a majority of the redshifted emission is to

the southwest, Fig. 4.4 shows that some redshifted emission extends past the continuum peak to the northeast. Since the redshifted emission is much stronger than the blueshifted emission in the region, it is preferentially weighted in the moment maps. All of the other moment maps exhibit relatively compact emission and do not exhibit any indication of rotation.

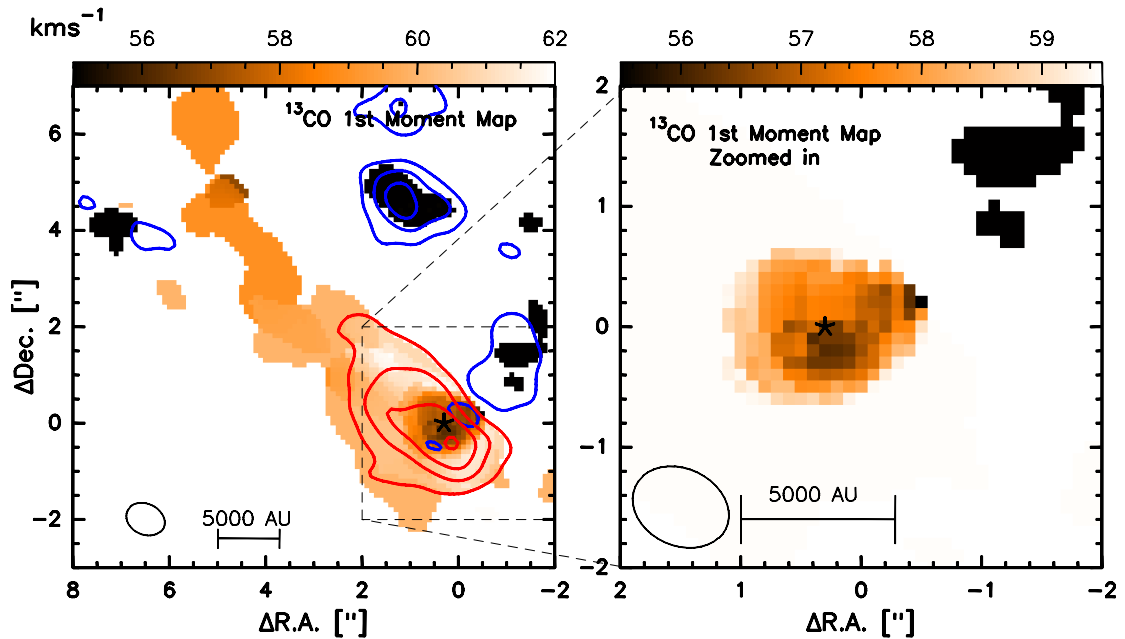


Figure 4.7: The velocity moment map of ^{13}CO . The red and blue contours in the left panel are the red- and blueshifted emission for 1 km s^{-1} channels centered on 55 km^{-1} and 61 km^{-1} respectively. Contours start at 2σ and increase in 2σ steps where σ_{red} is 0.110 Jy bm^{-1} and σ_{blue} is 0.072 Jy bm^{-1} . The panel on the right is a zoomed-in view of the central region. The velocity range has been modified in the panel at right to show detail of the central-most region better. The beam size and position of the dust continuum peak (star symbol) are indicated in each panel.

Rathborne et al. (2008) report extended emission in $^{13}\text{CO}(3-2)$ perpendicular to the outflow. The authors detect a velocity shift across the extension and propose that it may be a result of either a rotating envelope or an outflow. Figure 4.7 shows the velocity moment map of $^{13}\text{CO}(2-1)$. In this figure, contours of the same velocity ranges as used for red- and blueshifted emission in Rathborne et al. (2008) Fig. 6 are overlaid. Although the $^{13}\text{CO}(2-1)$ data presented here are a different transition than studied by Rathborne et al. (2008), the general trends are reproducible to some degree. Namely, the different transitions of ^{13}CO both exhibit extended redshifted emission more centrally located and weaker blueshifted emission offset to the northwest of the continuum peak. However, we do not interpret the observations as an extended rotating object perpendicular to the outflow.

4.4 Conclusions

In this chapter, SMA and IRAM 30 m data of the hot core IRAS 18507+0121 were analyzed. The SMA 220/230 GHz spectrum of IRAS 18507+0121 is rich with molecular lines. This is a

typical spectral signature of a source in the hot core phase of massive star formation.

Mapping the $^{12}\text{CO}(2-1)$ emission, we detect the molecular outflow in the northeast-southwest direction associated with this source. This orientation is in agreement with the $^{12}\text{CO}(1-0)$ outflow orientation determined by Shepherd et al. (2007). The redshifted outflow component is far stronger than the blueshifted component and traces the expanding outflow cavity.

Velocity moment maps of a representative sample of spectral lines were inspected for evidence of rotation. Most of the chemical species did not contain any indication of velocity gradients with the exception of C^{18}O . However, the gradient in C^{18}O is not perpendicular to the outflow, and the detection of emission along the outflow axis makes it evident that the C^{18}O gradient is influenced by the outflow. The velocity moment maps of H_2^{13}CO and SO also trace the outflow and do not provide any evidence for rotation in the central region.

An elongation in the 1.3 mm dust continuum perpendicular to the outflow provides potential indication for the presence of a disk component. Although not very convincingly seen when all of the data from both the compact and very extended configurations is included, the elongation comes out stronger when the data from the shortest baselines ($<100\text{ k}\lambda$) are not included. This leads us to believe that with higher angular resolution data, the elongation may become even more pronounced. If this elongation is the result of a disk component, its compact size may be the limiting factor to detecting rotation in the velocity moment maps. If this is the case, higher angular resolution in the line data may also lead to the discovery of rotation in some of the molecular lines present.

Chapter 5

Comparison of the Case Studies

The three sources introduced and analyzed in the previous three chapters represent different evolutionary stages in the massive star formation process. This is evident through several lines of reasoning, most notably in their individual chemical blueprints and in their physical appearances. IRDC 18223-3 is, as the naming scheme indicates, dark at infrared wavelengths up to $8\ \mu\text{m}$. This is an initial indication that this source is at one of the earliest observable stages of massive star formation. While it is clear that the other two sources are at more advanced stages of evolution, it is more difficult to determine whether IRAS 18151-1208 is more evolved than IRAS 18507+0121 or not. We suspect that IRAS 18151-1208 has not yet reached the hot core stage yet and hence is younger than IRAS 18507+0121. Our justification for this will be discussed below.

In Table 5.1, several properties of the three regions are listed which roughly can be used to glean clues about the ages of the sources. None of the indicators can be used independently to determine a definitive evolutionary sequence, much less a precise age for the individual sources. However, from the combination of several methods, we can get a feeling for evolutionary trends. Caveats and limitations of each method will be discussed separately in detail in the sections of this chapter.

Table 5.1: Comparison of observed/derived quantities of the three sources.

Object	C ¹⁸ O Line Width [km s ⁻¹]	Disk(?) Radius [AU]	8 μm detection	chem. richness [num of lines]
IRDC 18223	1.7	14000	no	5
IRAS 18151	2.9	5000	yes	4
IRAS 18507	2.8	<4000	yes	48

Disk radius refers to the radius of the flattened rotating or elongated structure observed. Chemical richness refers to the number of lines present in the SMA 220/230 GHz spectrum at the center of the dust continuum peak. In the case of IRAS 18507+0121, the number reported here includes only identified lines. Several additional lines exist which could not be identified.

5.1 The Spectral Approach

5.1.1 Infrared Observations

As a massive star evolves, it becomes visible at progressively shorter wavelengths. The spectrum of a blackbody at the initial 20 K of the surrounding molecular cloud peaks around $150\ \mu\text{m}$ so the beginning stages of massive star formation are only observable at radio and far infrared frequencies. As a massive star forms, it will become ‘visible’ at mid infrared wavelengths and then eventually at shorter wavelengths. The Infrared Dark Cloud IRDC 18223-3 remains undetected in all four mid-infrared wavelengths (3.6, 4.5, 5.8, and $8.0\ \mu\text{m}$) of the Spitzer GLIMPSE survey (Benjamin et al. 2003). The shortest wavelength IRDC 18223-3 has been detected at $24\ \mu\text{m}$ (Beuther & Steinacker 2007) whereas both IRAS 18151-1208 and IRAS 18507+0121 are detected in the mid-infrared at $8\ \mu\text{m}$. This provides a strong indication that IRDC 18223-3 is less evolved than the other two sources in this study.

5.1.2 SMA Spectra

While the SMA spectra shown in Figure 5.1 of IRDC 18223-3 and IRAS 18151-1208 do not exhibit significant differences in their chemical signatures, the hot core source 18507+0121 stands out as a source with a rich chemical diversity, clearly indicative of the hot core phase of massive star formation. Earlier stages in the star formation process have not had sufficient time to form the diversity of chemical species, nor are they warm enough to allow the higher energy transitions. For example, in IRAS 18507+0121, the CH_3CN (12–11) ladder at around 220.7 GHz includes the transitions up to $k=8$. These higher energy transitions have excitation temperatures in excess of a few hundred Kelvin are only produced once the temperature and density of a region become high enough.

The abundance of a particular molecule as well as the temperature and density of the region affect the strength of a molecular line. As these properties increase with time, the strengths of spectral lines also increase. However, it is impossible to directly compare the strengths of lines from one region to another on an absolute scale due to intrinsic brightness and spatial filtering variations which come about because of the different distances to the regions involved. So instead of comparing abundances, the types of molecules present in each region are compared. In star formation, it takes time before complex molecules are produced (Nomura & Millar 2004). The IRAS 18507+0121 spectrum exhibits far more complex molecules than the other sources. For example, the presence of the CH_3CN ladder up to the $k=8$ line as well as several sulfur bearing molecules indicate that IRAS 18507+0121 is more evolved than the other two sources.

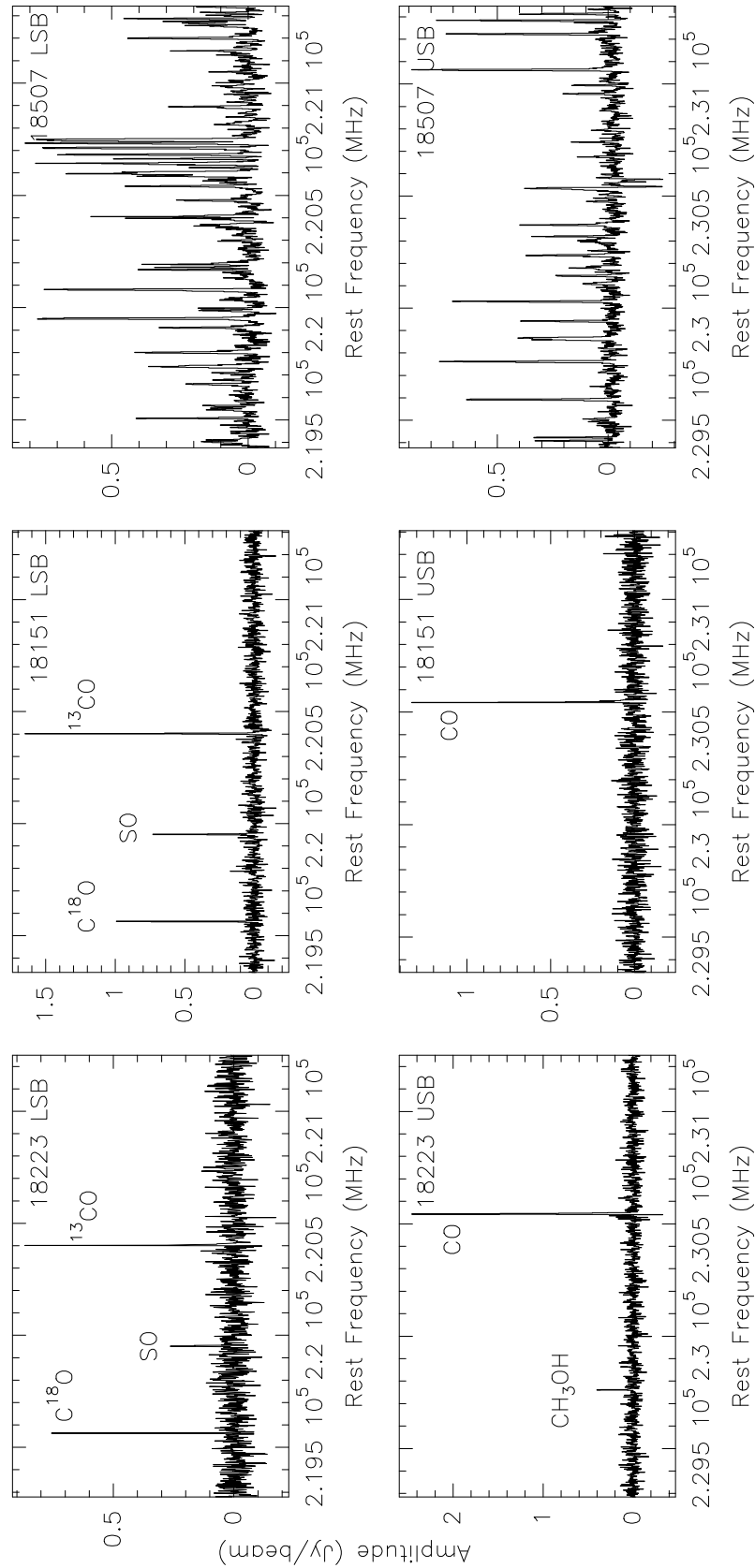


Figure 5.1: 220/230 GHz spectra from the SMA of IRDC 18223-3, IRAS 18151-1208, and IRAS 18507+0121 extracted at the central positions of the respective source's dust continuum peak. Each spectrum includes both compact configuration data and either extended or very extended configuration data. To prevent overcrowding in the IRAS 18507+0121 panels, the names of the lines have been omitted here. A similar figure with the lines labeled can be seen in Fig. 4.2.

5.1.3 CH₃OH

As shown in Chapter 2, methanol (CH₃OH) is present at the young Infrared Dark Cloud stage. We also determine it to be a good tracer of rotation in the region. In the more evolved high mass protostellar object IRAS 18151-1208, the CH₃OH is no longer detectable in the central region. As IRAS 18151-1208 is even closer than IRDC 18223-3, this is probably not attributed to a sensitivity effect. Interestingly, in IRAS 18151-1208 CH₃OH is detected in a region removed by seven arcseconds from the central continuum peak (see lower panel of Fig. 3.1). While an evolutionary effect is suggested here, the possibility that the presence of CH₃OH is an environmental effect such as a product of shocks cannot be ruled out.

In the hot core source IRAS 18507+0121, multiple methanol lines are detected. However, unlike IRDC 18223-3 in which CH₃OH traces a large rotating object, the CH₃OH detected in IRAS 18507+0121 is very compact and does not resolve rotational signatures (see Fig. 4.5). While the mechanism explaining the difference in observed characteristics of methanol at the various evolutionary stages is not clear, it appears that CH₃OH may be useful for disk studies only at the very earliest stages of massive star formation.

5.1.4 C¹⁸O Line Width

As a source evolves, the temperature and density in the region increase. As the temperature increases, noticeable effects in the spectrum include the appearance of higher energy transitions and broader line widths. This thermal broadening is a result of the velocity distribution of atoms in a gas becoming wider as the average kinetic energies of the atoms increase at higher temperatures. In a star formation region, the temperature increases over time, so it is therefore expected that the widths of spectral lines should increase with time. Of the sources in our study, IRDC 18223-3 has a noticeably smaller line width (see Table 5.1) than the others and is consistent with IRDC 18223-3 being the youngest source in our sample. The C¹⁸O line widths of the two more evolved sources are not significantly different from one another and cannot be used to distinguish places for these two sources in an evolutionary sequence.

5.2 The Physical Approach

Based on the infrared non-detection and the narrower line widths as described in the previous section, we are fairly confident that IRDC 18223-3 is the youngest source in our sample. Although the indicators of evolutionary differences are not as strong for the remaining two sources, we suggest that IRAS 18151-1208 is at an earlier evolutionary stage than the hot core IRAS 18507+0121 based mainly on the chemical diversity observed in IRAS 18507+0121. Although further constraints cannot be placed on the true age sequence with the characteristics of the dust and gas discussed in this section, trends supporting the adopted sequence which best explains the observations as described above in Section 5.1 are found.

5.2.1 Outflow Extent and Outflow Dynamical Age

A rough estimate for the ages of these regions can be made by measuring the properties of the outflow such as extent and maximum velocity. The age is then calculated simply by dividing the extent of the outflow by the velocity at which it is traveling. Descriptions of the measurements used to derive the dynamical ages can be found in Sections 2.3.3, 3.3.2, and 4.3.2. The dynamical ages of the three sources without a correction for inclination are 37,000 years, 32,000 years, and 23,000 years for IRDC 18223-3, IRAS 18151-1208 and IRAS 18507+0121 respectively. Although at first glance the numbers indicate an evolutionary trend opposite to what has been determined above, these values are not distinguishable from one another given the sources of error involved in the computation. One of the sources of uncertainty in this method is the orientation of the outflow. Although we postulate in Chapters 2 and 3 that the outflow may be roughly in the plane of the sky, this assertion cannot be made for IRAS 18507+0121, so an inclination angle of 45° is assumed following the approach of Shepherd et al. (2007). A correction factor of the tangent of the inclination angle would be necessary to determine dynamical ages more accurately. At low inclination angles such as we suspect may be the case in IRDC 18223-3 and IRAS 18151-1208, the dynamical ages of these sources become significantly smaller. Another source of error in this method is that the jets which entrain the molecular outflow have much higher velocities than the outflows themselves. Thus, with higher sensitivity data, the measured velocities in the line wings would be higher and estimated dynamical ages would be correspondingly younger. Given the errors associated with this method of age determination, the values for the outflow dynamical ages obtained in this manner cannot discriminate between the ages of these sources.

5.2.2 Spatial Extent of the Disk-like Object

In IRDC 18223-3, the flattened rotating object surrounding the central source has an approximate diameter of 28,000 AU (see Fig. 2.9). While indication of rotation perpendicular to the outflow orientation is not identified in the other two sources, elongation in the 1.3 millimeter dust continuum of these sources is detected. The elongation seen in IRAS 18507+0121 is not as prominent as that seen in IRAS 18151-1208, nevertheless, its presence is visible. In IRAS 18151-1208, the elongation in the dust continuum has a diameter of approximately 10,000 AU whereas the elongation in IRAS 18507+0121, if real, is not larger than about 4,000 AU.

The case studies presented in this thesis thus suggest that disks in massive star formation may undergo a progression over time from a large rotating toroid stage through a stage with a flattened, rotating object, then on to a compact accretion disk. However, this remains speculative due to low number statistics. Because other explanations for the observations such as multiplicity at the given resolution of our data cannot be ruled out, this sequence is merely suggested as a possibility. Future observations with higher spatial resolution and/or different molecular tracers may confirm or refute this interpretation. Resolving the elongations into multiple sources or

detecting velocity gradients along the elongated structures seen in IRAS 18151-1208 and IRAS 18507+0121 would provide strong evidence one way or the other for the different possibilities. Until then, an evolutionary trend from a large rotating toroid toward a more compact accretion disk provides a logical explanation for the observations at hand.

Chapter 6

Conclusions

6.1 Summary

Circumstellar disks are crucial elements in the formation of low mass stars, but our understanding of their role in massive star formation is still limited. The motivation for this thesis has been to improve the observational status for the as of yet only tentative indication for the existence of disk components around massive protostars.

The approach in this thesis has been to take an in-depth look at three examples of massive star formation and deduce information from observations about the possibility of a disk component. The observations come primarily from the Submillimeter Array (SMA) and IRAM 30 m single dish facilities. As the regions in this study are between 3000 and 4000 pc away, the $\sim 1''$ spatial resolution achievable with current submillimeter interferometers affords us resolution at spatial scales on the order of a few thousand AU.

These sources are at different evolutionary stages which sets an ideal stage for an observational study of how disks evolve in massive star formation. In all three sources, indications for a disk-like structure were identified. These observations have been discussed in the context of an accretion-based method of massive star formation and were found to be consistent.

6.1.1 Outflow

In all of the case studies, determining or confirming the outflow orientation was the first step. Although the existence of the disk component was the primary interest, clues to guide the search were obtained by studying the outflows. If disks are present, they should be perpendicular to the molecular outflow. Molecular outflows are easily resolved due to their large spatial extent. Also, molecular tracers of outflows are well-established, especially ^{12}CO , and are readily observed in star formation regions with standard observing set-ups.

For the youngest source in the study, IRDC 18223-3, no previous observations had detected the outflow component. The outflow is oriented in the northwest-southeast direction based on a blueshifted cone-shaped outflow component extending toward the southeast. The single

dish ^{12}CO data are consistent with this orientation, except that the majority of the blueshifted emission is seen on the northwest side of the continuum peak (opposite the blueshifted cone). This indicates that the outflow is roughly in the plane of the sky since part of both the northwest and the southeast component are seen approaching.

Previous low data quality single dish ^{12}CO observations of a more evolved source, IRAS 18151-1208, tentatively identified an outflow component in the region (Beuther et al. 2002b), and molecular Hydrogen observations at $2.12\ \mu\text{m}$ tracing a collimated jet were consistent with that morphology (Davis et al. 2004). In this thesis, high angular resolution ^{12}CO data were used to determine that the outflow is indeed in the orientation predicted by these previous studies. With the spectroscopic information at high angular resolution afforded by the SMA observations, we were able to determine the outflow kinematics. As in IRDC 18223-3, blueshifted emission was also detected on both sides of the IRAS 18151-1208 dust continuum peak and again this was interpreted to mean that the outflow lies close to the plane of the sky.

The morphology of the outflow traced by the $^{12}\text{CO}(2-1)$ data in the most evolved hot core source, IRAS 18507+0121, matches the $^{12}\text{CO}(1-0)$ morphology outlined by Shepherd et al. (2007) remarkably well. In this source, the outflow is oriented southwest-northeast with the dominant redshifted component in the southwest direction. Although Shepherd et al. (2007) suggest the presence of a weak secondary outflow associated with IRAS 18507+0121, its presence was not detected here. For this source, no clues were present to help establish the outflow's inclination with respect to the plane of the sky.

6.1.2 Disk Indications

Once the outflow orientation of each source had been determined using ^{12}CO , a search for indications of a circumstellar accretion disk perpendicular to the outflow was made. Different molecules trace different components within a star forming region, so a data set requires both outflow and high density tracers to make a successful search for signatures of disk rotation. Among others, high density tracing candidates include C^{17}O , NH_3 , C^{34}S , CH_3CN , and HCOOCH_3 . If a velocity gradient is detected perpendicular to the outflow by a high-density tracing molecule, this may be caused by a circumstellar accretion disk. Once a velocity gradient is established, position-velocity diagrams are used to determine the kinematics of the rotation.

In IRDC 18223-3, velocity gradients that are not aligned with the outflow orientation were detected in C^{18}O , N_2H^+ , and CH_3OH , although the gradient in CH_3OH is the most convincing and is perpendicular to the outflow. We suspect that C^{18}O is being affected by the outflow which would explain why the velocity gradient traced by that molecule is not orthogonal to the outflow. The position-velocity diagrams for this source (see Fig. 2.7) do not show a Keplerian rotational signature, but this is not surprising as accretion disks in massive star formation are not necessarily expected to be Keplerian. Opposed to low-mass stars in which the mass of the disk component is negligible, the mass of a disk would be significant compared to its central massive star. Such disks will probably fragment and form substructure within the disk. The

velocity gradient in IRDC 18223-3 spans a distance of 28,000 AU which is very large, and may have a smaller Keplerian component within. The large size of the observed velocity gradient may be a result of this source's early evolutionary phase.

Although minimal evidence for C¹⁸O and SO velocity gradients not aligned with the outflow were detected in IRAS 18151-1208, a lack of other potential disk-tracing molecules in the SMA data limited our chances to detect rotation perpendicular to the outflow. However, in this source, the 1.3 mm dust continuum emission is flattened and elongated in the direction orthogonal to the molecular outflow. A circumstellar disk would be consistent with this observation, so this interpretation was developed further. This modeling work is described further in the next subsection (Section 6.1.3).

In IRAS 18507+0121, despite the abundance of many possible disk tracing candidates, evidence for rotation was only tentatively seen in one chemical species. A velocity gradient was detected in C¹⁸O, although not perpendicular to the outflow. As C¹⁸O also traces emission from the outflow, its detection of rotation may be questionable. Although not as pronounced as in IRAS 18151-1208, an elongation was detected in the 1.3 mm dust continuum perpendicular to the outflow. This elongation is less than 4000 AU in diameter and became more prominent when the angular resolution was increased by including only the data from long baselines. This suggests that data with higher spatial resolution would provide further insight into the nature of the circumstellar region of IRAS 18507+0121.

The arguments presented in Chapter 5 suggest an evolutionary sequence with IRDC 18223-3 being the youngest and IRAS 18507+0121 the most evolved. Under this assumption, it was noticed that the sizes of the observed disk-like objects decrease as age increases. In the youngest source (IRDC 18223-3), the rotating object has a diameter of 28,000 AU, while in the more evolved high mass protostellar object (IRAS 18151-1208), the elongation in the continuum is approximately 10,000 AU and in the most evolved hot core (IRAS 18507+0121), the elongation in the continuum is no more than 4,000 AU. The decrease in size from a large rotating flattened structure to a compact elongated structure perpendicular to the outflow suggest that the size scales of the disk component may decrease as they evolve around forming massive stars.

6.1.3 Theoretical Modeling

For the sources IRDC 18223-3 and IRAS 18151-1208 models were created which reproduced the observations. For IRDC 18223-3, the Ulrich mass inflow model was used (Ulrich 1976; Keto 2007). This model conserves angular momentum and includes gravity and a rotating envelope. Although a disk was not included in the modeling, it was established that a single rotating entity is capable of reproducing the observed CH₃OH velocity gradient. In some cases, multiple unresolved sources may be mistaken for signatures of an accretion disk, but the results of the modeling are consistent with rotation being a more likely explanation for the observed gradient.

For IRAS 18151-1208, we tested whether a scaled-up low-mass disk model could reproduce

the elongated dust continuum observations. Using the Monte Carlo 3D Radiative Transfer code of Wolf et al. (2003), we concluded that the scaled-up model was capable of replicating the observed elongation. In the scaled-up model, the values for the shape parameters such as the disk's relative scale height at one third of the outer radius, the density distribution and flaring exponents remained identical. The parameters for the outer radius, disk mass, central star mass and luminosity all required larger values than in the T Tauri cases to which IRAS 18151-1208 was compared. Analysis of the system's Toomre stability led to the conclusion that regions only within the central-most 40 AU were stable which is consistent with theoretical work on the subject. Taking this modeling project one step further, modeled images were produced at 6, 12, and 25 μm and discussed what future observations may be possible with up-and-coming observatories such as ALMA, JWST, and the E-ELT.

In both cases, the modeling results are not unique solutions to the question of whether accretion disks in these massive star formation regions are being observed, but rather are one possible explanation for those observations. Although other explanations for the observations such as multiplicity cannot be ruled out, the success of the modeling is consistent with the hypothesis that massive stars form via accretion from a circumstellar disk.

6.2 Direction for the Future

With the eventual goal of understanding the complete process of massive star formation, understanding the mechanism by which a star gains its mass is a necessary piece in the puzzle. Much progress has been made in recent years in the field of massive disk studies, but there are still many unresolved questions pertaining to their nature and prevalence. Although the current submillimeter arrays such as SMA, PdBI and CARMA will continue to be an integral part of massive star formation research, the advent of the Atacama Large Millimeter/submillimeter Array (ALMA) for early science within the next few years will provide an amazing boost to the current state of massive disk research.

The main ALMA array will consist of 50 antennas 12 meters in diameter at a 5000 m elevation site in the Atacama Desert of northern Chile and a compact array will contain another four 12-meter antennas and twelve 7-meter antennas. The array will have baselines ranging from as short as 15 m to as long as 16 km. Ten receiver bands with frequencies ranging from 30 GHz ($\lambda \sim 1$ cm) up to 950 GHz ($\lambda \sim 0.3$ mm) are planned. An artist's view of the ALMA site with the array in an extended configuration can be seen in Fig. 6.1. One of the antenna transporters is also shown in this figure.

One limitation of this thesis is the small number statistics from which the conclusions are based. Looking for indications of rotating flattened structures perpendicular to outflows in additional massive star formation regions would help to determine whether the decreasing with age trend seen in the sizes of disks is representative of a general tendency. This would require observations of additional sources which exhibit indications for a disk as well as characteristics



Figure 6.1: A computer generated image of the ALMA site with the array in an extended configuration. Figure credit: ALMA (ESO/NAOJ/NRAO).

that allow us to place them roughly on an evolutionary timeline. In this direction, we can begin expanding our sample by reducing and analyzing a CARMA dataset on hand of the high mass protostellar region IRAS 18566+0408. Observations at 7 mm hint at the presence of a disk around this source, although the CARMA data have much higher angular resolution, and will allow investigation of the disk's kinematics if present.

Further research is necessary for all three of the sources discussed in this thesis. Observations at higher angular resolution may reveal the true nature of Keplerian disks in these systems. For instance, with an angular resolution of $0.1''$, ALMA will probe size scales on the order of 300-400 AU at the distances of these objects. With this order of magnitude increase in resolution compared to current submillimeter interferometers, ALMA will surely prove to be an extremely valuable resource for massive disk studies. Additionally, kinematic confirmation that the elongated structures in IRAS 18151-1208 and IRAS 18507+0121 are rotating is necessary to aid in a more complete interpretation of those observations.

The case study of IRAS 18507+0121 brings to light several possibilities for future investigation. Namely, as disks evolve, it is not clear whether the chemical tracers of disks also change meaning simply that the correct tracer is missing in our spectral setup, or whether such a rotating structure's shrinkage over time has rendered it irresolvable at the spatial resolution available with current observations. Tests to distinguish between these possible explanations include using current interferometers to look at different spectral ranges that include other chemical species or using ALMA in the future to probe spatial scales not achievable with current observatories.

One natural question that arises from the modeling work with IRAS 18151-1208 is whether

the results can be extrapolated to other wavelengths. Predictions of what the region will look like at other wavelengths can be made, but it will take future observatories such as ALMA, JWST, and the E-ELT to confirm, refute, or place constraints on these conjectures. Coming in the near future, observations of massive star formation regions with ALMA in the submillimeter/millimeter regime will trace the cold gas and dust and with JWST in the mid-infrared will trace the warm dust. As ALMA and JWST will trace different physical processes in massive star formation, the complementarity of these future observatories will make an understanding of massive star formation across a broad wavelength regime possible.

With the arrival of ALMA on the horizon, this thesis research has been an excellent way to prepare for the advancements that will be possible once observing begins. Massive star formation studies are ideally suited for science with ALMA. With spatial resolution of the completed array eventually reaching the order of $0.01''$ as well as increased sensitivity, spectral resolution, and imaging capabilities, ALMA will certainly revolutionize the field of disk studies in massive star formation in the coming decade.

Acknowledgements

I am foremost thankful for the amazing scientific opportunities available at MPIA which have allowed me to develop as a scientist, but also as an individual during the three and a half years here as a PhD student. I am thankful for the scientific experiences that have broadened my horizons, and allowed me to see the world through international travel. I am also thankful for the opportunity to immerse myself in another culture, feeding and appeasing my appetite for experiencing a different way of life.

This journey would not have been as enjoyable (or even possible) without the following people. I thank:

- Henrik Beuther for limitless support in matters both scientific and non-scientific. For bringing the CfA experience alive. For allowing to correct his English.
- Qizhou Zhang for his supervision during my six month research exchange at the CfA.
- Robert ‘Kim’ Kimberk, Steve Leiker, Cosmo Papa, Ed Tong, and Pat Riddle for their guidance in the SMA Receiver Lab during the six months at the CfA and for teaching me the nuts and bolts (and chips and grids) about instrumentation.
- Henrik Beuther, Thomas Henning, Ralf Klessen, Robi Banerjee & Matthias Bartelmann for evaluating this thesis, guiding my thesis work along the way, and/or agreeing to be on my defense committee.
- Christian Fendt for making the IMPRS program run as smoothly as possible.
- My family whose continuous love and encouragement as well as occasional physical presence made it all the way to Germany from nearly half way around the world.
- Thomas Baumann for the Möbius band, for his deep-rooted friendship and for riding life’s roller coaster with me.
- Marcello Cacciato and Surhud More for all of the distractions. For the tech support and at times, emotional support. For contributing to the lively spirit of our office.
- Ros Skelton and Rory Holmes for the endless joy of hearing their versions of our native language. For the misunderstandings and just plain not-understandings. Ros for her

use of South African abbrevs like “avo” and “howzit?” and for asking “What’s for pudding?”. Rory for saying things like “dungarees”, “Gordon Bennett”, “cleaning rota” and “courgette” and for pronouncing “zebra” and “soldering” the way he does.

- Felix Friedl for laughing with me. For making parties, taking me ski driving and climbing and for all the other fun direct translation mix-ups.
- Jürgen Sauter for being a connoisseur of geek humor and for teaching me that nature is just an approximation to theory.
- Abby Hedden & Michael Stenner for their friendship and long walks which got us through the Boston winter.
- André, Boris, Christine, Eva, Hendrik, Jan, Joachim, Juliet, Markus, Martin, Mica, Monika, Natalie, Roman, Rory, Tessel, and all of the other coffee hour folks for providing a social outlet for frustrations and humor, and for nurturing friendships.
- The Collegium Musicum musicians for the combined music and German immersion atmosphere.

Thank you to all. I also thank these inanimate objects:

- The Königstuhl for keeping my sense of wonder for the natural world alive through the hikes to MPIA. For testing and pushing my body’s physical limitations through the bike rides to MPIA.
- The RNV for providing such miserable bus service and consequently the impetus for me to bike and hike to MPIA, something I truly came to enjoy.
- Leo for being my best inanimate friend and clearing up much German language related confusion.

Bibliography

- Arce, H. G., Shepherd, D., Gueth, F., et al. 2007, *Protostars and Planets V*, 245
- Bally, J. & Zinnecker, H. 2005, *AJ*, 129, 2281
- Banerjee, R. & Pudritz, R. E. 2007, *ApJ*, 660, 479
- Beltrán, M. T., Cesaroni, R., Neri, R., et al. 2004, *ApJ*, 601, L187
- Beltrán, M. T., Cesaroni, R., Neri, R., et al. 2005, *A&A*, 435, 901
- Benjamin, R. A., Churchwell, E., Babler, B. L., et al. 2003, *PASP*, 115, 953
- Bernard, J. P., Dobashi, K., & Momose, M. 1999, *A&A*, 350, 197
- Beuther, H., Churchwell, E. B., McKee, C. F., & Tan, J. C. 2007, in *Protostars and Planets V*, ed. B. Reipurth, D. Jewitt, & K. Keil, 165–180
- Beuther, H., Hunter, T. R., Zhang, Q., et al. 2004, *ApJ*, 616, L23
- Beuther, H., Schilke, P., Menten, K. M., et al. 2002a, *ApJ*, 566, 945
- Beuther, H., Schilke, P., Menten, K. M., et al. 2005a, *ApJ*, 633, 535
- Beuther, H., Schilke, P., Sridharan, T. K., et al. 2002b, *A&A*, 383, 892
- Beuther, H., Sridharan, T. K., & Saito, M. 2005b, *ApJ*, 634, L185
- Beuther, H. & Steinacker, J. 2007, *ApJ*, 656, L85
- Beuther, H. & Walsh, A. J. 2008, *ApJ*, 673, L55
- Beuther, H., Zhang, Q., Greenhill, L. J., et al. 2005c, *ApJ*, 632, 355
- Beuther, H., Zhang, Q., Sridharan, T. K., & Chen, Y. 2005d, *ApJ*, 628, 800
- Bonnell, I. A. & Bate, M. R. 2006, *MNRAS*, 370, 488
- Bonnell, I. A., Bate, M. R., Clarke, C. J., & Pringle, J. E. 1997, *MNRAS*, 285, 201
- Bonnell, I. A., Bate, M. R., Clarke, C. J., & Pringle, J. E. 2001, *MNRAS*, 323, 785

- Bonnell, I. A., Bate, M. R., & Zinnecker, H. 1998, *MNRAS*, 298, 93
- Bonnell, I. A., Vine, S. G., & Bate, M. R. 2004, *MNRAS*, 349, 735
- Bontemps, S., Andre, P., Terebey, S., & Cabrit, S. 1996, *A&A*, 311, 858
- Bronfman, L., Nyman, L.-A., & May, J. 1996, *A&AS*, 115, 81
- Cabrit, S. & Bertout, C. 1990, *ApJ*, 348, 530
- Cabrit, S. & Bertout, C. 1992, *A&A*, 261, 274
- Campbell, M. F., Sridharan, T. K., Beuther, H., et al. 2008, *ApJ*, 673, 954
- Carey, S. J., Noriega-Crespo, A., Price, S. D., et al. 2005, in *Bulletin of the American Astronomical Society*, Vol. 37, *Bulletin of the American Astronomical Society*, 1252
- Cesaroni, R. 2005, *Ap&SS*, 295, 5
- Cesaroni, R., Felli, M., Testi, L., Walmsley, C. M., & Olmi, L. 1997, *A&A*, 325, 725
- Cesaroni, R., Galli, D., Lodato, G., Walmsley, C. M., & Zhang, Q. 2007, in *Protostars and Planets V*, ed. B. Reipurth, D. Jewitt, & K. Keil, 197–212
- Cesaroni, R., Galli, D., Lodato, G., Walmsley, M., & Zhang, Q. 2006, *Nature*, 444, 703
- Cesaroni, R., Neri, R., Olmi, L., et al. 2005, *A&A*, 434, 1039
- Chini, R., Hoffmeister, V., Kimeswenger, S., et al. 2004, *Nature*, 429, 155
- Choi, M., Evans, II, N. J., & Jaffe, D. T. 1993, *ApJ*, 417, 624
- Churchwell, E. 2002, *ARA&A*, 40, 27
- Churchwell, E., Wolfire, M. G., & Wood, D. O. S. 1990, *ApJ*, 354, 247
- Clark, P. C., Glover, S. C. O., Bonnell, I. A., & Klessen, R. S. 2009, *ArXiv e-prints*
- Cortes, P. C., Crutcher, R. M., Shepherd, D. S., & Bronfman, L. 2008, *ApJ*, 676, 464
- Cyganowski, C. J., Whitney, B. A., Holden, E., et al. 2008, *AJ*, 136, 2391
- Davis, C. J., Varricatt, W. P., Todd, S. P., & Ramsay Howat, S. K. 2004, *A&A*, 425, 981
- Dutrey, A., Guilloteau, S., & Ho, P. 2007, in *Protostars and Planets V*, ed. B. Reipurth, D. Jewitt, & K. Keil, 495–506
- Frerking, M. A., Langer, W. D., & Wilson, R. W. 1982, *ApJ*, 262, 590
- Goldsmith, P. F., Langer, W. D., & Velusamy, T. 1999, *ApJ*, 519, L173

- Goto, M., Usuda, T., Dullemond, C. P., et al. 2006, *ApJ*, 652, 758
- Hatchell, J., Thompson, M. A., Millar, T. J., & MacDonald, G. H. 1998, *A&AS*, 133, 29
- Hildebrand, R. H. 1983, *QJRAS*, 24, 267
- Hofner, P., Cesaroni, R., Olmi, L., et al. 2007, *A&A*, 465, 197
- Hofner, P., Wyrowski, F., Walmsley, C. M., & Churchwell, E. 2000, *ApJ*, 536, 393
- Iben, I. J. 1965, *ApJ*, 141, 993
- Jackson, N. 2008, in *Lecture Notes in Physics*, Berlin Springer Verlag, Vol. 742, *Lecture Notes in Physics*, Berlin Springer Verlag, ed. F. Bacciotti, L. Testi, & E. Whelan, 193–218
- Jijina, J. & Adams, F. C. 1996, *ApJ*, 462, 874
- Jørgensen, J. K., Hogerheijde, M. R., Blake, G. A., et al. 2004, *A&A*, 415, 1021
- Kahn, F. D. 1974, *A&A*, 37, 149
- Kastner, J. H., Zuckerman, B., Weintraub, D. A., & Forveille, T. 1997, *Science*, 277, 67
- Keto, E. 2003, *ApJ*, 599, 1196
- Keto, E. 2007, *ApJ*, 666, 976
- Keto, E. & Wood, K. 2006, *ApJ*, 637, 850
- Keto, E. R., Ho, P. T. P., & Haschick, A. D. 1988, *ApJ*, 324, 920
- Kratter, K. M. & Matzner, C. D. 2006, *MNRAS*, 373, 1563
- Kroupa, P., Tout, C. A., & Gilmore, G. 1993, *MNRAS*, 262, 545
- Krumholz, M. R., Klein, R. I., & McKee, C. F. 2007, *ApJ*, 656, 959
- Krumholz, M. R., Klein, R. I., McKee, C. F., Offner, S. S. R., & Cunningham, A. J. 2009, *Science*, 323, 754
- Kurtz, S. 2002, in *Astronomical Society of the Pacific Conference Series*, Vol. 267, *Hot Star Workshop III: The Earliest Phases of Massive Star Birth*, ed. P. Crowther, 81–94
- Kurtz, S., Cesaroni, R., Churchwell, E., Hofner, P., & Walmsley, C. M. 2000, *Protostars and Planets IV*, 299
- Larson, R. B. & Starrfield, S. 1971, *A&A*, 13, 190
- López-Sepulcre, A., Codella, C., Cesaroni, R., Marcelino, N., & Walmsley, C. M. 2009, *A&A*, 499, 811

- Marseille, M., Bontemps, S., Herpin, F., van der Tak, F. F. S., & Purcell, C. R. 2008, *A&A*, 488, 579
- Massey, P. & Hunter, D. A. 1998, *ApJ*, 493, 180
- Mathis, J. S., Rumpl, W., & Nordsieck, K. H. 1977, *ApJ*, 217, 425
- McKee, C. F. & Tan, J. C. 2003, *ApJ*, 585, 850
- Molinari, S., Brand, J., Cesaroni, R., & Palla, F. 1996, *A&A*, 308, 573
- Moscadelli, L., Cesaroni, R., & Rioja, M. J. 2005, *A&A*, 438, 889
- Nomura, H. & Millar, T. J. 2004, *A&A*, 414, 409
- Ossenkopf, V. & Henning, T. 1994, *A&A*, 291, 943
- Palla, F. & Stahler, S. W. 1990, *ApJ*, 360, L47
- Pinte, C., Padgett, D. L., Ménard, F., et al. 2008, *A&A*, 489, 633
- Pollack, J. B., Hollenbach, D., Beckwith, S., et al. 1994, *ApJ*, 421, 615
- Qi, C., Ho, P. T. P., Wilner, D. J., et al. 2004, *ApJ*, 616, L11
- Ramesh, B., Bronfman, L., & Deguchi, S. 1997, *PASJ*, 49, 307
- Rathborne, J. M., Jackson, J. M., Chambers, E. T., et al. 2005, *ApJ*, 630, L181
- Rathborne, J. M., Jackson, J. M., & Simon, R. 2006, *ApJ*, 641, 389
- Rathborne, J. M., Jackson, J. M., Zhang, Q., & Simon, R. 2008, *ApJ*, 689, 1141
- Salpeter, E. E. 1955, *ApJ*, 121, 161
- Sandell, G., Wright, M., & Forster, J. R. 2003, *ApJ*, 590, L45
- Sauter, J., Wolf, S., Launhardt, R., et al. 2009, *A&A*, 505, 1167
- Scalo, J. M. 1986, *Fundamentals of Cosmic Physics*, 11, 1
- Schilke, P., Walmsley, C. M., Pineau des Forets, G., & Flower, D. R. 1997, *A&A*, 321, 293
- Schreyer, K., Henning, T., van der Tak, F. F. S., Boonman, A. M. S., & van Dishoeck, E. F. 2002, *A&A*, 394, 561
- Schreyer, K., Semenov, D., Henning, T., & Forbrich, J. 2006, *ApJ*, 637, L129
- Shakura, N. I. & Sunyaev, R. A. 1973, *A&A*, 24, 337
- Shepherd, D. S. & Churchwell, E. 1996, *ApJ*, 457, 267

- Shepherd, D. S., Claussen, M. J., & Kurtz, S. E. 2001, *Science*, 292, 1513
- Shepherd, D. S. & Kurtz, S. E. 1999, *ApJ*, 523, 690
- Shepherd, D. S., Nürnberger, D. E. A., & Bronfman, L. 2004, *ApJ*, 602, 850
- Shepherd, D. S., Povich, M. S., Whitney, B. A., et al. 2007, *ApJ*, 669, 464
- Sicilia-Aguilar, A., Hartmann, L., Calvet, N., et al. 2006, *ApJ*, 638, 897
- Simon, M., Dutrey, A., & Guilloteau, S. 2000, *ApJ*, 545, 1034
- Sobolev, A. M., Cragg, D. M., Ellingsen, S. P., et al. 2007, in *IAU Symposium*, Vol. 242, IAU Symposium, ed. J. M. Chapman & W. A. Baan, 81–88
- Sollins, P. K., Zhang, Q., Keto, E., & Ho, P. T. P. 2005, *ApJ*, 631, 399
- Sridharan, T. K., Beuther, H., Saito, M., Wyrowski, F., & Schilke, P. 2005a, *ApJ*, 634, L57
- Sridharan, T. K., Beuther, H., Schilke, P., Menten, K. M., & Wyrowski, F. 2002, *ApJ*, 566, 931
- Sridharan, T. K., Williams, S. J., & Fuller, G. A. 2005b, *ApJ*, 631, L73
- Stapelfeldt, K. R., Krist, J. E., Ménard, F., et al. 1998, *ApJ*, 502, L65+
- Stapelfeldt, K. R., Ménard, F., Watson, A. M., et al. 2003, *ApJ*, 589, 410
- Thompson, A. R., Moran, J. M., & Swenson, Jr., G. W. 2001, *Interferometry and Synthesis in Radio Astronomy*, 2nd Edition, ed. M. J. M. S. G. W. J. Thompson, A. R.
- Toomre, A. 1964, *ApJ*, 139, 1217
- Ulrich, R. K. 1976, *ApJ*, 210, 377
- Vaidya, B., Fendt, C., & Beuther, H. 2009, *ApJ*, 702, 567
- Watson, A. M., Stapelfeldt, K. R., Wood, K., & Ménard, F. 2007, in *Protostars and Planets V*, ed. B. Reipurth, D. Jewitt, & K. Keil, 523–538
- Weingartner, J. C. & Draine, B. T. 2001, *ApJ*, 548, 296
- Whitney, B. A., Wood, K., Bjorkman, J. E., & Wolff, M. J. 2003, *ApJ*, 591, 1049
- Williams, S. J., Fuller, G. A., & Sridharan, T. K. 2004, *A&A*, 417, 115
- Wolf, S. 2003, *Computer Physics Communications*, 150, 99
- Wolf, S., Henning, T., & Stecklum, B. 1999, *A&A*, 349, 839
- Wolf, S., Padgett, D. L., & Stapelfeldt, K. R. 2003, *ApJ*, 588, 373

Wolf, S., Schegerer, A., Beuther, H., Padgett, D. L., & Stapelfeldt, K. R. 2008, *ApJ*, 674, L101

Wolfire, M. G. & Cassinelli, J. P. 1987, *ApJ*, 319, 850

Wuchterl, G. & Klessen, R. S. 2001, *ApJ*, 560, L185

Yorke, H. W. & Sonnhalter, C. 2002, *ApJ*, 569, 846

Zhang, Q., Ho, P. T. P., & Ohashi, N. 1998, *ApJ*, 494, 636

Zhang, Q., Hunter, T. R., Brand, J., et al. 2005, *ApJ*, 625, 864

Zhang, Q., Hunter, T. R., Brand, J., et al. 2001, *ApJ*, 552, L167

Zinnecker, H. & Yorke, H. W. 2007, *ARA&A*, 45, 481